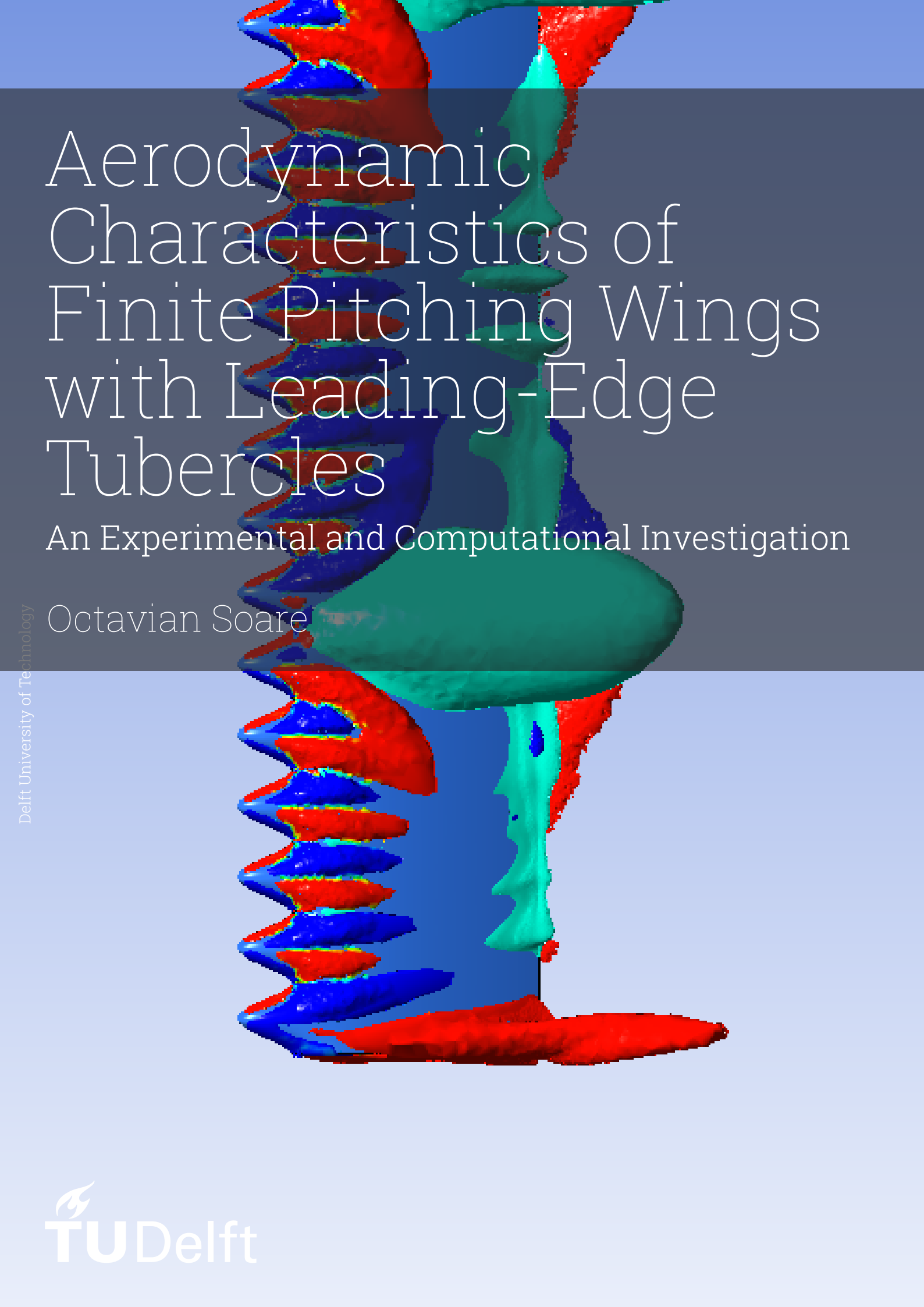

Aerodynamic Characteristics of Finite Pitching Wings with Leading-Edge Tubercles

An Experimental and Computational Investigation

Octavian Soare

Delft University of Technology

TU Delft

Aerodynamic Characteristics of Finite Pitching Wings with Leading-Edge Tubercles

An Experimental and Computational Investigation

by

Octavian Soare

To obtain the degree of Master of Science,
at the Delft University of Technology,
to be defended publicly on Friday July 5, 2024 at 9:30 AM.

Student number:	4832701
Thesis supervisors:	Dr. M. Li
	Dr. Ir. F. Scarano
Scientific advisors:	Dr. Ir. S. Hickel
Project Duration:	09, 2023 - 06, 2024
Faculty:	Faculty of Aerospace Engineering, Delft

An electronic version of this thesis is available at `https://repository.tudelft.nl/`.

TU Delft

Preface

This report represents the condensed work of the past 9 months, but it is just the keystone that closes an arch started 6 years ago, when I first stepped in Delft to start my journey into becoming an aerospace engineer.

First and foremost I want to acknowledge and thank for their contribution my supervisors Morgan and Fulvio for their guidance and advice over all these months. At the end of the thesis, I feel that I have really learned from you. There have been many thesis meetings that I approached very worried about my progress or my results and that I left, after the discussions with you, uplifted and with fresh ideas and avenues to pursue. For all of this and for bearing with my lack of planning, the most sincere thank you! Furthermore, also from the Aerodynamics department, I want to thank Stefan Hickel for taking part in many of our meetings and for the very valuable advice provided not just on CFD, but on all the aspects of the project. I want to also thank and acknowledge the invaluable help from Stefan Bernardy, Frits Donker Duyvis and Peter Duyndam with everything wind tunnel, manufacturing and setup related issues that Pere and I would have been in big trouble without. And last but not least, thank you to my colleague Pere for all the inspiration and motivation throughout the thesis and for the 2 very intense wind tunnel weeks we have shared and I cannot wait to see you and your work on track.

None of what I achieved would have ever been finished were it not for the amazing support and occasional productive "bullying" from the great friends I made in Delft. To my Romanian friends, Nico, Crina, Andrada, Elena, Vlad, Tudor, Alex and Adi, thank you for always being there through thick and thin! Also, to my very international family, Praj, Gopal, Manos and Manos, Irmak, Aytek, Alex, Mohamed and Kevin, you guys are amazing and I cannot wait to replicate our Stieltjesweg dinners in the future, wherever that will lead us.

Finally, to my family who made this all possible and supported me unconditionally: Vă mulțumesc, sunt astăzi un inginer doar mulțumită vouă!

Octavian Soare
Delft, June 2024

Abstract

Blades in rotor systems such as helicopters and wind turbines experience highly dynamic inflow conditions such as rapid pitching that can lead to dynamic stall. This in turn causes large force fluctuations which translate into fatigue for the blade structure and controllability issues for the vehicles. Biomimetics brings a potential solution in the shape of leading-edge tubercles inspired by the flippers of humpback whales, which possess impressive manoeuvrability for their body size. While the ability of this bio-inspired leading-edge shape to soften and delay stall in steady conditions is well-documented, there are very few studies investigating its effect in unsteady conditions. Further, most existing works focused on full-span wings, finite span effect is more the rule than exception in real-world applications. Therefore, the scope of this study is to analyse the effect of leading-edge tubercles on the flow structure evolution throughout sinusoidal oscillations of finite wings and on their tip vortex strength. The pitching oscillations were picked to be representative of typical helicopter blade conditions: the main oscillation used being described by $\alpha(t) = 15^\circ + 15^\circ \times sin(2\pi ft - \frac{\pi}{2})$ with a reduced frequency $k = 0.1$ that place the flow phenomena squarely in the unsteady aerodynamics regime.

To analyse the two main aspects mentioned above, this thesis combined two methodologies: one experimental and the other computational. Wind tunnel experiments were conducted on three finite wings, one with a straight leading-edge and two with different leading-edge tubercles, all subjected to sinusoidal pitching oscillations. The flow was seeded with Helium-filled soap bubbles, and 3D Particle Tracking Velocimetry technique with the state-of-the-art Shake-The-Box algorithm were employed to obtain the complex instantaneous flow field around the wings throughout the oscillation cycles. After obtaining the particle tracks, phase-averaging was used to improve the quality of experimental results by making use of the multiple oscillation cycles recorded. The computational study replicates the wind tunnel conditions. U-RANS simulations were performed using the Ansys CFX solver and a deforming mesh to model the pitching motion of the aerofoil. Both experiments and simulations were conducted at a chord Reynolds number of $Re = 3.3 \times 10^4$ due to limitations regarding the achievable oscillating frequency of the actuator and the wind tunnel size and capabilities.

Both experimental and computational results correlate well in terms of the flow structure, allowing for a detailed comparison between the two methods. Similar to observations under steady conditions, wings with leading-edge tubercles under dynamic pitching also show a more benign stall behaviour and quicker reattachment on the downstroke of the oscillations compared to their straight leading-edge counterpart. This is attributed to the compartmentalisation effect of the streamwise vortices shed by the tubercles. However, the experiments show that, surprisingly, the angle of attack at which the maximum lift coefficient is produced is not increased or delayed compared to the straight-leading-edge wings. Furthermore, the tubercle wings exhibit reduced tip vortex strength throughout the oscillation cycle, thanks in part to the destructive effect of the streamwise vortices near the wing tip on the tip vortex. Finally, in close correlation with the tip vortex circulation, the tubercle wings have a lower induced drag coefficient compared to straight-leading-edge wings, with a better span efficiency also as a result of the compartmentalisation effect of tubercles on the spanwise flow.

Contents

List of Figures

List of Tables

Nomenclature

Abbreviations

Abbreviation	Definition
CAD	Computer Aided design
CFD	Computational Fluid Dynamics
DES	Detached Eddy Simulation
DSV	Dynamic Stall Vortex
HFSB	Helium-Filled Soap Bubbles
LES	Large Eddy Simulation
OTF	Optical transfer Function
PIV	Particle Image Velocimetry
PTV	Particle Tracking Velocimetry
RANS	Reynolds-averaged Navier-Stokes
U-RANS	Unsteady Reynolds-averaged Navier-Stokes
VSC	Volume Self-Calibration

Symbols

Symbol	Definition	Unit
A_{osc}	Amplitude of oscillation	[deg]
A_{tub}	Amplitude of tubercles	[mm]
AR	Aspect Ratio	[-]
b	Span	[mm]
c	Chord	[mm]
C	Courant number	[-]
C_L	Lift Coefficient	[-]
C_D	Drag Coefficient	[-]
f	Frequency	[Hz]
k	Reduced frequency	[-]
M	Mach number	[-]
Re	Reynolds number	[-]
t	Time	[s]
U_∞	Freestream velocity	[m/s]
U	Velocity X component	[m/s]
V	Velocity Y component	[m/s]
W	Velocity Z component	[m/s]
α	Angle of attack	[deg]
Γ	Circulation	[m^2/s]
ω	Circular frequency	[deg/s]
ω_x	Vorticity X component	[1/s]
ω_y	Vorticity Y component	[1/s]
ω_z	Vorticity Z component	[1/s]
ρ	Density	[kg/m^3]

1

Introduction

1.1. Problem statement

1.1.1. Helicopter rotor aerodynamics

Rotocraft are extremely important air transportation vehicles thanks to their ability to land in confined spaces and to hover. Leishman [1] explains that advances in rotorcraft performance are currently limited by the aerodynamic characteristic of the rotor blade. Colpitts and Perez [2] further detail that, in hover, the rotor thrust is restricted by the achievable blade pitch angle before blade stall and by rotor tip speed. Given the current technology for engine and drive systems, improvements of rotor performance could be accomplished through increased aerodynamic performance of the rotor blade.

The widely ranging inflow conditions and Mach number that a rotor blade experiences are detailed by Seddon and Newman [3] and are usually illustrated through what is known as a "figure-of-eight" diagram such as the ones shown in Figure 1.1. These plots track a particular spanwise location on the blade, near the tip, as it completes one full rotation. They highlight the oscillatory nature of the inflow conditions, as well the passing of the retreating blade through a stall region and the passing of the advancing blade through a drag rise region.

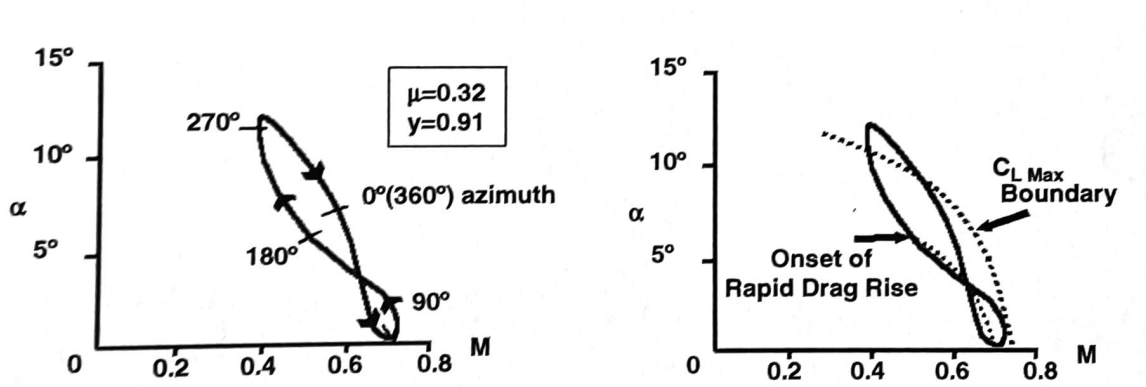

Figure 1.1: Figure-of-eight diagrams for a typical helicopter blade with a NACA0012 airfoil [3]

The main aspect that is evident from the figure-of-eight plots is the dynamic nature of the inflow conditions and hence of the aerodynamic phenomena that involve the wing. As early as 1960, Carta [4] showed the hysteretic behaviour of an oscillating symmetric airfoil helicopter blade. However, the complexity does not stop here: If the frequency and amplitude of the oscillation of the angle of attack are high enough, dynamic stall occurs.

1.1.2. Dynamic stall

Dynamic stall is a phenomenon characterized by the sudden, unsteady separation of airflow over the airfoil, leading to significant changes in lift, drag, and pitching moment, often with pronounced and sometimes undesirable aerodynamic effects. The sequence of events that characterise dynamic stall is shown in Figure 1.2. According to Kramer [5], the rapid rotation of the airfoil does not come, at first, with a change of the pressure distribution on the suction side of the airfoil that would be expected at the new increased angle of attack, a lag time existing between the airfoil motion and the pressure response. This lag time increases and the hysteretic character of the lift vs. angle of attack curve becomes more evident as the frequency of oscillation gets larger [6]. This lag also means that the airfoil separation is slightly delayed because the boundary layer is not experiencing the increased pitch angle until a later moment. When the angle of attack has increased enough, a vortex is formed and shed at the leading-edge of the airfoil, shown in Figure 1.2 (e). This is commonly known in literature as the 'dynamic stall vortex' or 'DSV'. The DSV convects downstream above the suction side of the airfoil, providing vortex lift that increases the lift slope of the airfoil significantly and produces additional lift in the range of 50-100% of the maximum lift value in static conditions, visible in the Figure 1.2 (g) events sequence. The downstream convection of the DSV also leads to a rear shift of the centre of pressure of the airfoil, which translates into a nose-down pitching moment. This is followed by a full and sudden loss of lift, corresponding to Figure 1.2 (h). When the oscillating airfoil returns to an angle of attack lower than the static critical angle, the flow reattaches (Figure 1.2 (k) , completing the hysteretic lift vs. angle of attack loop.

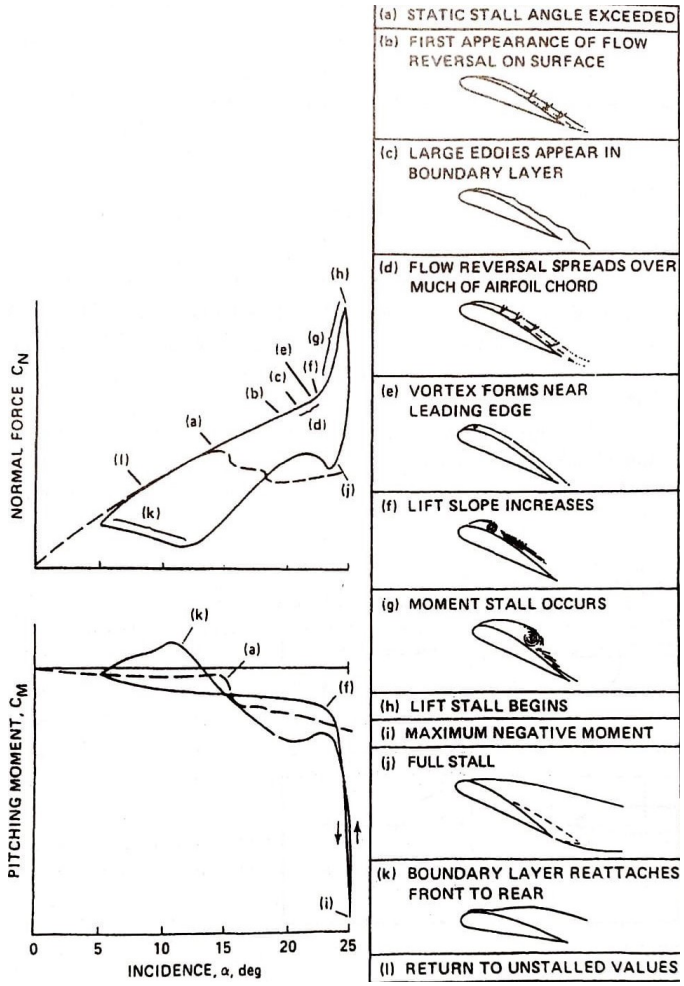

Figure 1.2: Dynamic stall events on a NACA 0012 airfoil [7]

It is appropriate to introduce at this point the notion of reduced frequency k, a dimensionless parameter

commonly used in literature as a measure of the unsteadiness of the problem [1]. Reduced frequency is defined as the ratio shown in Equation 1.1, where ω is the circular frequency, b is the semi-chord of the wing or airfoil and U_∞ is the freestream velocity.

$$k = \frac{\omega \cdot b}{U_\infty} \tag{1.1}$$

Therefore, the reduced frequency is to be understood as the picthing frequency normalised by the freestream velocity of the flow. The fathers of aeroelasticity and unsteady aerodynamics, Sears and Wagner, characterise the flow conditions as being in the:

- Steady aerodynamic regime for $k = 0$
- Quasi-steady aerodynamic regime for $0 < k < 0.05$
- Unsteady aerodynamic regime for $k > 0.05$

Values of $k > 0.2$ are considered highly unsteady flows. To anchor these values in real-life applications for a better understading, helicopter blades operate around the value of $k = 0.1$ [8]. Dynamic stall, which occurs in this unsteady aerodynamic regime, is a problem because it leads to rapid variations in the lift and drag forces experienced by a wing, these large and frequent fluctuations proving to be an issue for the structure and control of the aircraft, rotor, or wind turbine. In the case of helicopters, rotor blades experience varying angles of attack as they rotate, especially during different phases of flight, maneuvers, or changes in airspeed. When rotor blades encounter rapid changes in angle of attack, they can be susceptible to dynamic stall, which can have several implications for helicopter performance and safety: dynamic stall can result in vibrations and reduced lift during maneuvers. In wind turbines, it can lead to increased fatigue loads and reduced energy capture efficiency.

1.1.3. The tip vortex

The pressure difference between the suction side and the pressure side of any wing creates a spanwise pressure gradient, causing air to flow around the wingtip and form vortices at the tips [9]. The strength of the tip vortex is of particular importance to rotors like those of helicopters and wind turbines because of a number of reasons:

- Stronger tip vortices lead to higher power losses. The rotor induced power is proportional to the kinetic energy of the trailed tip vortices. As the vortex strength increases, more energy is lost to the wake, decreasing overall rotor efficiency. [10]

- Blade-vortex interactions: Stronger tip vortices result in more intense blade-vortex interactions (BVI), which can lead to increased noise, vibration, and structural loads on the rotor blades. A visualisation of the way the tip vortices of helicopter blades propagate and impact the next blades is shown in Figure 1.3 from a CFD simulation performed by the German Aerospace Center (DLR). The effects of vortices impacting the blades not only reduce the aerodynamic efficiency but also impact the overall performance and operational capabilities of the rotorcraft. [1]

- Hover performance: In hover conditions, stronger tip vortices can lead to increased power requirements and reduced hover efficiency. This is particularly important for helicopters, where hover performance is a critical design consideration. [11]

- Forward flight performance: During forward flight, the interaction between the advancing and retreating blade tip vortices becomes more complex. Stronger vortices can lead to asymmetric loading and increased drag, potentially reducing the rotor's efficiency in forward flight. [1]

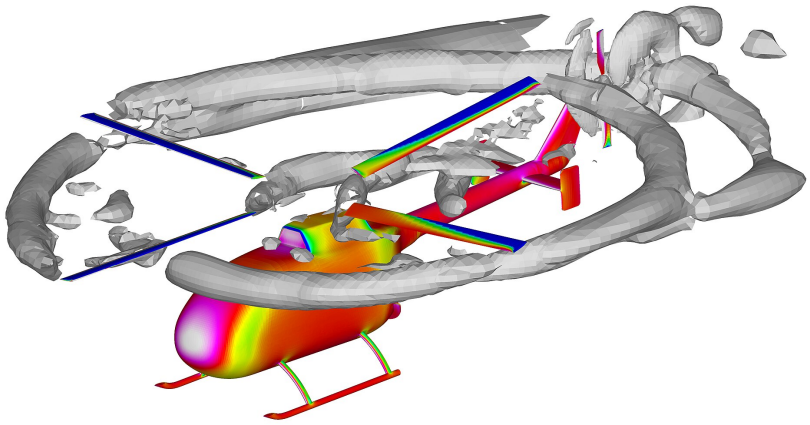

Figure 1.3: Iso-surface of vorticity visualisation of helicopter blade tip vortices [1]

1.2. Research scope

Biomimetics brings a potential solution to reducing the negative effects of dynamic stall as well as reducing the tip vortex strength [2] in the shape of leading-edge tubercles inspired by the flippers of humpback whales, which possess impressive manoeuvrability for their body size. These are formalised as sinusoidal protuberances applied on the leading-edge of wings. While the ability of these leading-edge tubercles to soften and delay stall in steady conditions is already well-documented, there are very few studies investigating its effect in unsteady conditions. Further, most existing works focused on full-span wings, finite span effect is more the rule than exception in real-world applications. Therefore, the scope of this study is twofold:

- First, it is to analyse the effects of leading-edge tubercles on the flow structure evolution throughout sinusoidal oscillations of finite wings. This type of oscillations is considered most representative of real-life applications such as helicopter rotor blades. The first scope of this study is to find whether the previously documented physical mechanisms of the tubercles still work as expected in these unsteady conditions and whether the angle of attack envelope of the wings can be extended, in the context of this oscillatory regime.

- The other main target of this thesis project is to investigate the effects of leading-edge tubercles on the tip vortex strength. This includes researching the effect of the tip shape, also referred to as the "tip end condition", on the tip vortex strength and behaviour, as well as investigating whether the tubercles decrease the induced drag of the wings throughout their oscillation cycles. Furthermore, the tip vorticity (and, when integrated, the circulation) is a value of interest because it is proportional to the lift force produced by the wing and can offer an insight into the evolution of the lift force for the experimental case where force balance measurements were not possible.

1.3. Methodology

The essence of this study revolves around the comparative analysis between conventional smooth leading-edge wings and those modified with leading-edge tubercles under various conditions of pitch oscillation. To analyse the two main aspects mentioned above, this thesis combined two methodologies: one experimental and the other computational.

[1] `https://www.dlr.de/en/media/images`

Wind tunnel experiments were conducted on three finite wings, one with a straight leading-edge and two with different leading-edge tubercles, all subjected to sinusoidal pitching oscillations. The flow was seeded with Helium-filled soap bubbles, and the novel 3D Particle Tracking Velocimetry technique with the state-of-the-art Shake-The-Box algorithm were employed to obtain the complex instantaneous flow field around the wings throughout the oscillation cycles. After obtaining the particle tracks, phase-averaging was used to improve the quality of experimental results by making use of the multiple oscillation cycles recorded.

Motivated by the lack of force measurements from the wind tunnel, the computational study aims to complement the experimental one and therefore replicates the wind tunnel conditions. U-RANS simulations were performed using the Ansys CFX solver and a deforming mesh to model the pitching motion of the aerofoil. Both experiments and simulations were conducted at a chord Reynolds number of $Re = 3.3 \times 10^4$ due to limitations regarding the achievable oscillating frequency of the actuator and the wind tunnel size and capabilities. The use of both experimental and numerical allows for a thorough and robust understanding of the flow structures and provides the study with both qualitative and quantitative results.

1.4. Report outline

This report commences with Chapter 2, offering a comprehensive review of the literature regarding the biomimetic approach of the leading-edge tubercles. The main flow mechanisms involved with the tubercles are identified and explained in more depth. A research gap is then identified leading to the presentation of three main research questions. This is followed by an overview of previously used experimental and numerical methods in the context of leading-edge tubercle studies.

Following the literature review, Chapter 3 offers insight into the methodology, experiment design and procedures involved in the experimental study and the computational study, respectively. This chapter will also touch upon the limitations of each set-up and how these affect the results.

Chapter 4 aims to prove the validity of both the experimental and numerical methods and delves into the marriage of the two methods and the comparison between their results.

The results of the comparative study between the different leading-edge and tip shapes on the wings, in the attempt to answer the research questions, are presented in Chapter 5. This is followed by drawing the conclusion and offering future work recommendations in Chapter 6.

Finally, a quote from 1975 belonging to William J. McCroskey, a renowned American aeronautical engineer, sets the tone well for the present study: "*Fortunately, engineers and technologists do not wait until everything is completely understood before building and trying new devices. Even so, an improved understanding of fundamental unsteady fluid flow processes can serve to stimulate new innovations, as well as improvements in the performance, reliability and costs of many existing machines. Therefore, research in unsteady fluid dynamics seems assured a lively future in modern industrial societies.*"

2

Background Information

2.1. Biomimetics

Fish [12] explains that biomimetism is an interdisciplinary field that seeks to imitate and apply the structures, mechanisms, and principles found in biological organisms to the development and enhancement of human-made technologies. Through the study and emulation of nature's time-tested patterns and strategies, this approach aims to solve complex human problems and improve the efficiency, sustainability, and functionality of engineered systems. In the context of the dynamic stall problem, a possible solution has been found by studying the humpback whales, their swimming behaviour and particular morphology.

Humpback whales, shown in Figure 2.1, are distinguished by their impressive size and distinctive body characteristics, as well as their remarkable feeding strategies and unique flipper morphology. These marine mammals, known for their agility in water, utilize highly maneuverable and elongated flippers, the longest relative to body size among cetaceans [13], to execute tight-radius turns essential for their prey capture techniques. Their specialized feeding behaviors, such as the "bubble netting" method, showcase their ability to herd and trap small fish or plankton by creating bubble barriers, followed by a swift, upward lunge through the concentrated prey. It is believed that the tubercle-shaped structures on the leading-edges of their flippers enable their flippers to maintain lift at high angles of attack, and ultimately their tight turning radius and high maneuverability.

Fish and Battle [13] dig deeper into the hydrodynamic implications of the leading-edge tubercles's presence on the flippers of humpback whales. Two morphological aspects of the flippers point to their hydrodinamic capabilities. First, the cross-section of the flippers very well resembles an airfoil-like shape, identified to be closest to the $NACA63_4 - 021$ low-drag airfoil, shown below in Figure 2.2.

Furthermore, Fish and Battle [13] present an even more interesting finding regarding the tubercles: barnacles, a form of parasitic crustaceans that attach themselves to surfaces, were only found on the whale flippers's leading-edges at the peak locations of the tubercles and not in-between the tubercles. Barnacles can only attach themselves to wetted areas with lower flow velocity, which suggests there is a variation in the spanwise velocity profile of the flipper with lower velocities around the leading-edge at the peaks and higher velocities at the troughs. This further led to the theory that the leading-edge tubercles act like large vortex generators whose vortices help delay stall.

After the previously described theory, Miklosovic et. al [15] subsequently investigates the effects of leading tubercles through wind tunnel testing, confirming that the wing with tubercles delayed the stall angle by 40% and increased the maximum lift coefficient by 6% compared to the straight leading-edge, when finite wing models resembling flippers were set to increasing angles of attack in a steady state scenario. This shows the performance potential of the tubercles and suggests it might be a solution

[1] `https://www.thoughtco.com/humpback-whale-facts-4154353`

Figure 2.1: The Humpback Whale (*"Megaptera novaeanglie"*) [1]

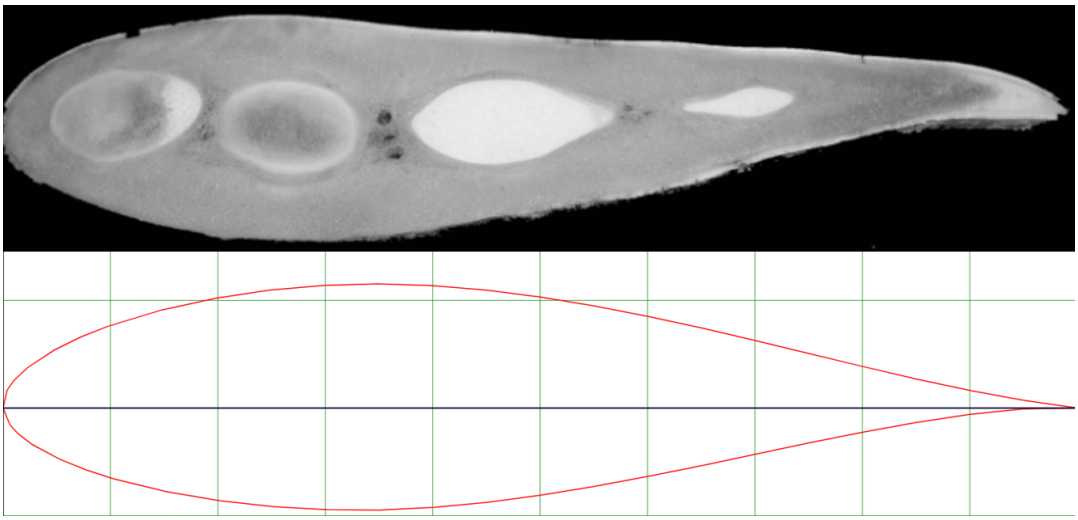

Figure 2.2: Humpback whale flipper cross-section compared to $NACA63_4 - 021$ airfoil contour [14]

for the dynamic stall problem described in Subsection 1.1.2. The mechanisms involved will be further detailed in Section 2.3.

2.2. Idealised tubercle shape

Most previous studies simplify and idealise the tubercle shape by a sinusoide shape in planform view. Essentially, the tubercle planform shape is defined by two parameters: the amplitude and the wavelength of the sinusoide, as illustrated by Figure 2.3. The same type of parametrisation, with somewhat different notations is used all throughout literature, from earlier works on leading-edge tubercles such as Miklosovic et al. in 2004 [15] to more recent studies such as that of Fernandes et al. in 2013 [16] or that of Borg in 2012 [17].

In cross-section, they are usually simplified as an elongated airfoil leading-edge, blending back to the original airfoil shape by the chordwise location of the highest thickness point of the airfoil, as chosen

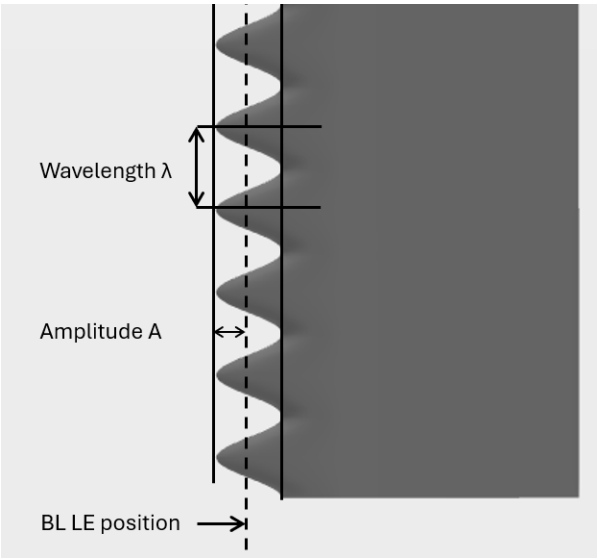

Figure 2.3: Typical geometric description of the tubercle planform shape - own drawing

and illustrated by Custodio et al. [18] in Figure 2.4. It is apparent that by doing this, the peak airfoil ends up having a sharper leading-edge curvature and the trough airfoil a blunter leading-edge radius. However, it is important to note that Johari et al. [14] have performed experiments comparing

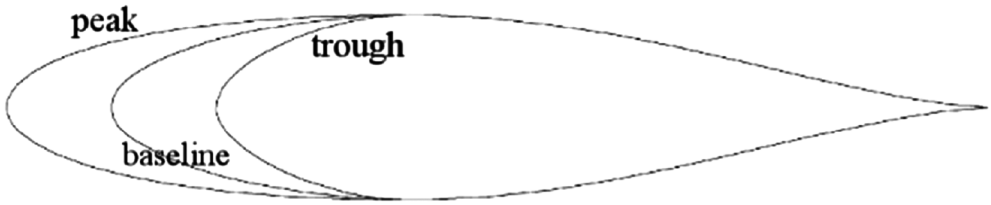

Figure 2.4: Cross-section view of airfoil geometry at different locations of the tubercle [18]

2.3. Flow mechanisms of tubercles

Rostamzadeh et al. [19] offers perhaps the best overview on the flow mechanisms involved with tubercle leading-edges, but in the following section only the most important and generally agreed-upon mechanisms will be discussed in more depth.

2.3.1. Vortex generators

The first and probably the most important and widely accepted mechanism is that at non-zero angles of attack the leading-edge tubercles act as vortex generators. Each of the two edges of a tubercle sheds a streamwise vortex. These have the known effect, similar to vortices produced by conventional strakes, of transferring kinetic energy from the freestream flow into the boundary layer, thus making it more resilient to adverse pressure gradients and delaying stall. As mentioned earlier, this theory was proposed by Fish and Battle [13], but validated and reinforced by Miklosovic et al. [15]. Hansen et al. [20] also draws the conclusion that leading-edge tubercles behave in a similar fashion vortex generators and that the ratio between the tubercle amplitude and wavelength is a relevant parameter for the strength of the shed streamwise vortices.

2.3.2. Rounded delta wings

Another potential physical mechanism generated by the tubercles is that of so called vortex lift or "reflective lift". If the amplitude and period of the planform sinusoide are big enough, the planform shape of a tubercle ends up resembling a delta wing that is rounded at the tip. One known effect of delta wings is that the two counter-rotating vortices shed by the long, angled leading-edges. The low static pressure associated with the vortex cores leads to additional top surface suction, namely the vortex lift. The leading egde vortex shedding of a delta wing is shown in Figure 2.5. Similarly, each tubercle sheds two such counter-rotating vortices and one theory is that these boost lift at higher angles of attack by the aforementioned vortex lift mechanism.

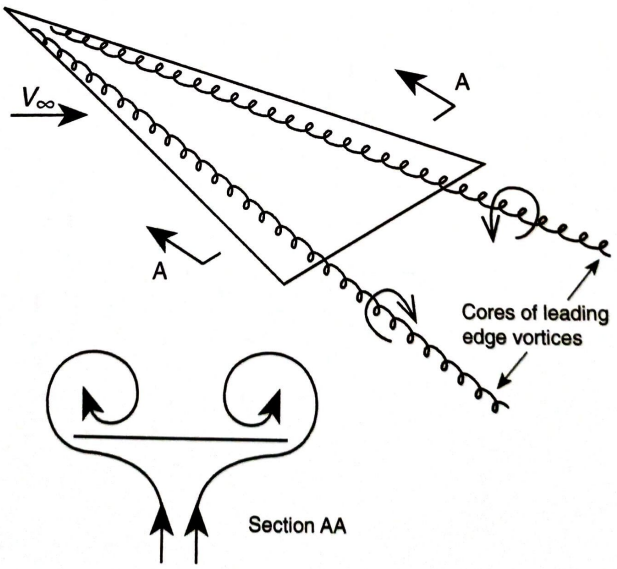

Figure 2.5: leading-edge vortices on a delta wing [21]

This theory was proposed by Custodio [18], but was contested by Bolzon et al. [22] based on two relevant differences between the delta wings and the tubercles: first, in the case of delta wings, the vortices induce downwash on the surface of the wing, but the upwash occurs further away from the surface, whereas in the case of the tubercles, both the induced downwash and induced upwash regions occur immediately in the proximity of the wing. Secondly, the shear scale difference between a typical delta wing and a tubercle, coupled with the rounded shape, produce much weaker vortices and therefore the effect is negligible.

2.3.3. Variation of the effective AoA

One effect that goes hand-in-hand with both previously described ones, but is more widely accepted is that the counter-rotating streamwise vortices produced by the tubercles alter the effective local angle of attack that the airfoil sees. The airfoil at a peak spanwise location sees a lower effective angle of attack than the airfoil at a trough location because the tubercle vortices induce downwash at the peaks and upwash at the troughs. The induced vertical velocities are visible in Figure 2.6. This is even more accentuated by the difference in local chord length, that means the airfoil at the peak experiences a shallower adverse pressure gradient because of its longer chord.

This effect ties in with the difference in velocity profile over the whale's flippers that lead to the barnacles attaching themselves only at tubercle peak locations, as explained in the Section 2.1 on biomimetism. The difference in velocities, particularly around the suction peak near the leading-edge, with the trough experiencing much higher velocities, is visible in the pressure coefficient distribution over the airfoil at peak and trough sections Figure 2.7. All of this translates to a wing with leading-edge tubercles exhibiting delayed stall at the peak locations and earlier signs of stall at trough locations compared to

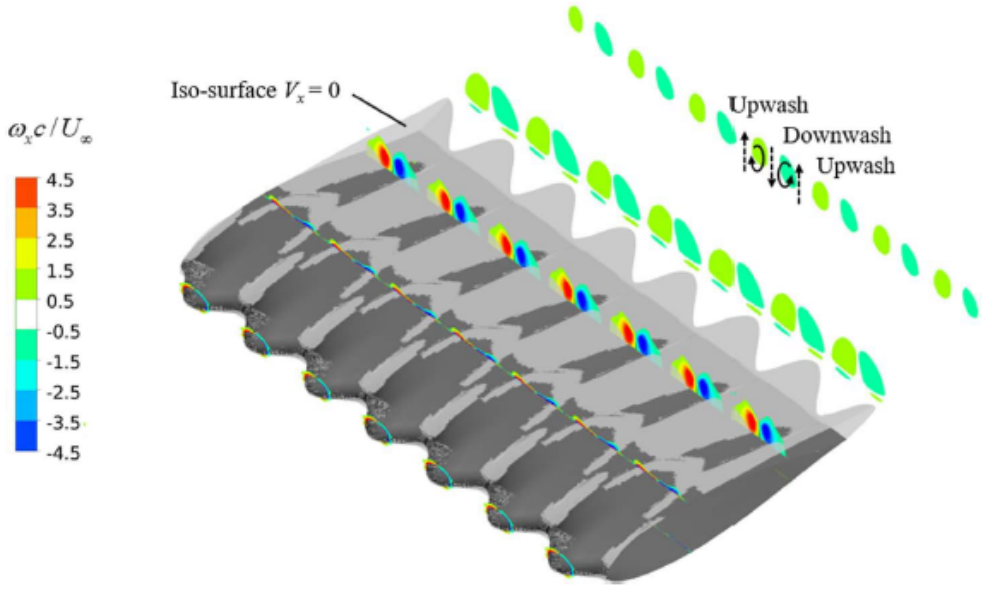

Figure 2.6: Visualisation of the vortex-induced upwash and downwash along the span, from Cai et al. [23]

a straight leading-edge wing.

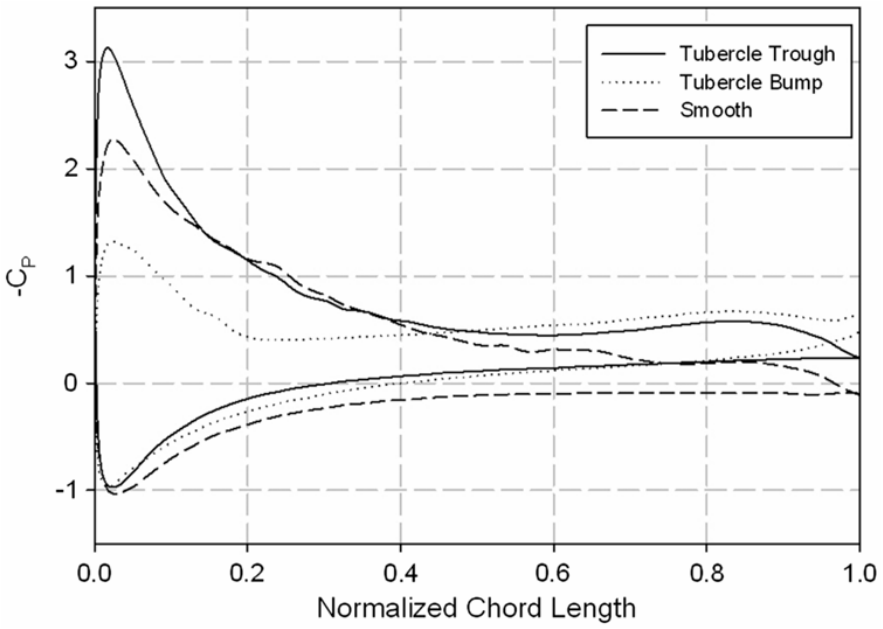

Figure 2.7: Chordwise pressure coefficient distribution at tubercle peak (bump) and trough (valley) obtained by Weber et al. [24]

2.3.4. Spanwise compartmentalisation

Multiple researchers starting from Fish and Battle [13], Hansen et al.[20], Pedro and Kobayashi [25] and up to more recent studies by Moscato [26] propose another flow mechanism that is a result of the streamwise vortices produced by the tubercles, namely that these vortices act similar to wing fences

and essentially become a barrier in the spanwise propagation of stall.

To illustrate this effect, the visualisation of a snapshot of the suction side of a wing with tubercles obtained by an own U-RANS simulation at the fixed angle of attack $\alpha = 15°$ is useful, shown in Figure 2.8. The red and blue surfaces shown are iso-surfaces of vorticity around the X-axis (streamwise component) of equal value, but opposite sign. This is also useful to visualise the way the tubercles each roll-up these two counterrotating vortices, as mentioned above. Furthermore, in the results, the grey iso-surface (also indicated by the arrow) shows flow of velocity smaller than zero, indicating an area of reversed flow, indicative of stall. This stall cell appears bound by the tubercle streamwise vortices that are deformed around it. This supports the theory that these act as a barrier against the propagation of the stall region.

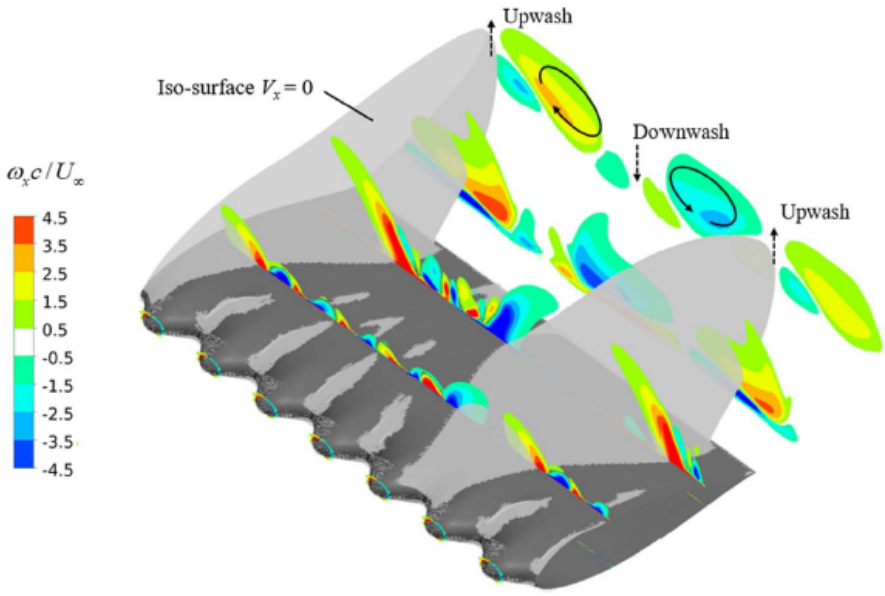

Figure 2.8: Compartmentalisation of stall cells by the streamwise vortices, from Cai et al. [23]; the separated flow region is indicated by the iso-surface of velocity $V_x = 0[m/s]$

2.4. Overview of previous studies and results

2.4.1. Finite span wings - tubercles, steady aerodynamic conditions

Research on the effects of LE tubercles on 3D finite wings in steady conditions dates mostly from the past 5 years, in chronological order Reid et al. in 2019 [27], Moscato et al. in 2022 [26] and Colpitts and Perez in 2023 [2]. Their studies have revealed interactions between the streamwise vortices shed by the tubercles and the wing tip vortex. Reid et al. [27] found that the tip vortex has a lower vorticity in teh tubercle case, decreasing in turn the induced drag. This is confirmed by Colpitts and Perez [2] who studied this effect on non-oscillating rotor blades.

Reid et al. [27] performed a wind tunnel study on rectangular finite wings at Reynolds numbers between $Re = 8 \times 10^4$ and $Re = 2 \times 10^5$, using wings with aspect ratios of $AR = 3$, $AR = 5$ and $AR = 7$ that are based on a NACA0012 airfoil and with different tip end conditions. The conclusions were that the wings with tubercles showed $C_{L_{max}}$ values approximately 2% lower than for the straight leading-edges, but with the stall angle is delayed by $3 - 5°$. The lift curve is straightened, not exhibiting the characteristic sharp decrease of the baseline wings, aligning with previous 2D (infinite span wings) results. Furthermore, they suggest the distribution of velocities close to the tip as influenced by the tip end condition (i.e. whether the wing ends with a peak or with a valley, as shown in Figure 2.9) has in turn an effect on the spanwise propagation of stall and on the induced drag [27], with the valley tip end

conditions showing the highest improvement in post stall lift. As explained in Subsection 2.3.4, Reid et al. suggest the streamwise vortices shed by the tubercles also delay the onset and spanwise, as well as chordwise, propagation of stall as a result of compartmentalisation.

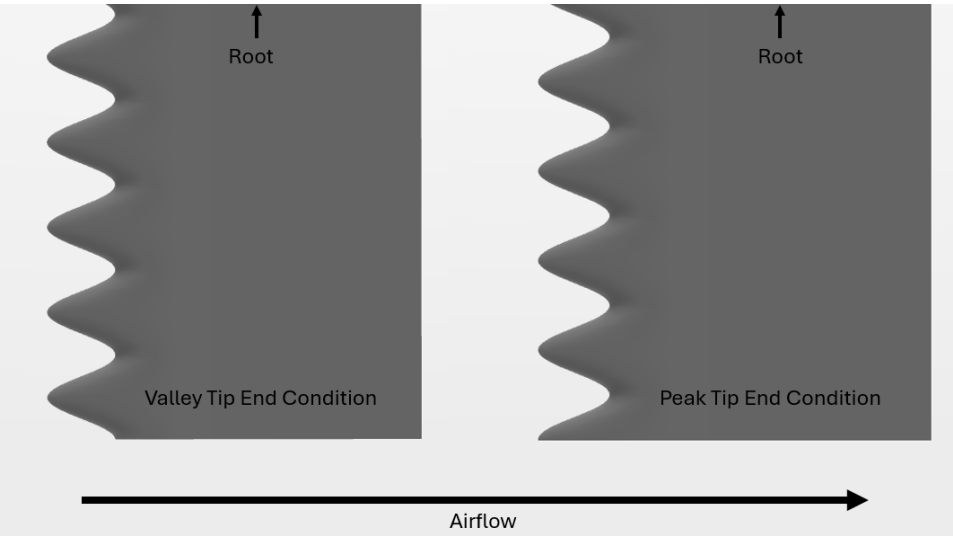

Figure 2.9: Geometrical illustration of difference in tip end condition - own drawing

Moscato et al. [26] have also performed a wind tunnel experiment, but this time also aided by planar PIV, besides the force balance measurements. The main difference to the previous study is the focus on wing models that more closely resemble simplified versions of the humpback whale flippers that sparked the studies on tubercles, mentioned in Section 2.1. The force coefficient results again align with previous 2D studies and the ones obtained by Reid et al., exhibiting a lower $C_{L_{max}}$, but a straighted lift curve, as shown in Figure 2.10 that represents existing results from literature, assembled by Moscato et al. Furthermore, the PIV planes obtained reinforce the known flow mechanisms stated in Section 2.3.

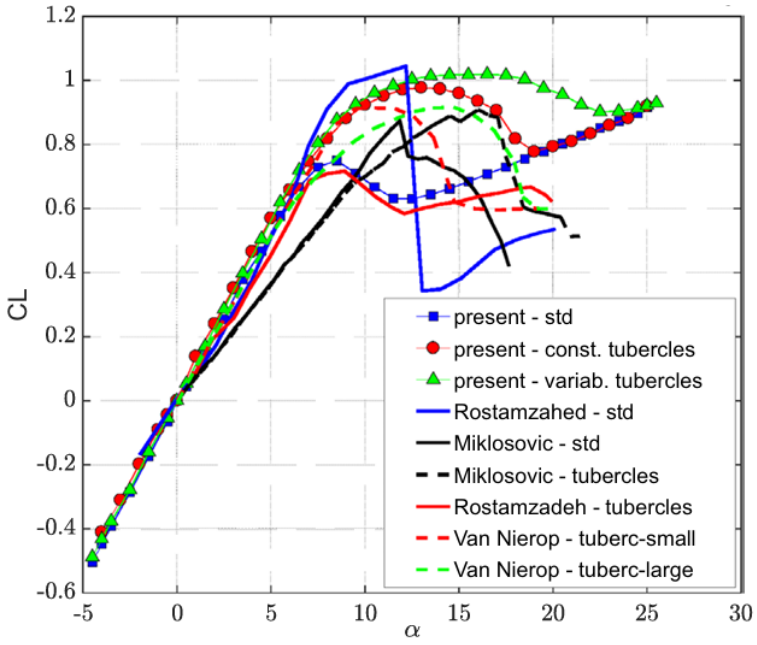

Figure 2.10: Lift coefficient vs. angle of attack graph of Moscato et al.'s wings (denoted with "present") and previous results [26]

Colpitts and Perez [2] took the study of the tubercles one step closer to a real-life scenario, performing a computational study on leading-edge tubercles applied on the blades of a canonical rotor known as the "Caradona and Tung Rotor". The blades were set to a fixed angle of attack, therefor the simulations still belong to the steady aerodynamic regime, but there is a significant spanwise velocity component involved in the flow physics due to the rotation of the blades. They found that wings with sinusoidal shape tubercles improve the coefficient of thrust, but reduce the coefficient of power. They attribute the improvement in rotor performance to the streamwise counterrotating vortices which re-energise the boundary layer and prevent trailing edge separation. Concerning the 3D effects, they suggest these streamwise vortices also prevent tip losses and improve thrust as the interaction between the tip vortex and tubercle vortices compartmentalizes the flow. Colpitts and Perez show this effect reduces spanwise flow along the blade and thus reduces induced drag.

2.4.2. Finite span wings - tubercles, unsteady aerodynamic conditions

The only existing study on finite span wings with leading-edge tubercles under unsteady conditions is Borg's Master Thesis [17] where the author has chosen to analyse in the wind tunnel rectangular wings with various tubercle shapes. The aspect ratio was selected to be $AR = 2.5$ and Reynolds number $Re = 1.3 \times 10^4$. The author chose to perform the oscillations centred around a mean amplitude equal to the static stall angle of the respective wing, with amplitudes of 5° and 7° at a reduced frequency of $k = 0.08$.

The author's conclusions in what concerns the dynamic studies are that the tubercled wings exhibited an increase in the maximum lift generated as well as smaller hysteresis gap between the upstroke and the downstroke phases, when compared to their own static lift curves than the straight leading-edge wings, as exemplified in Figure 2.11. Because the oscillations are centred around different angles, the author does not make any direct comparison between the straight leading-edge wings and the tubercled ones.

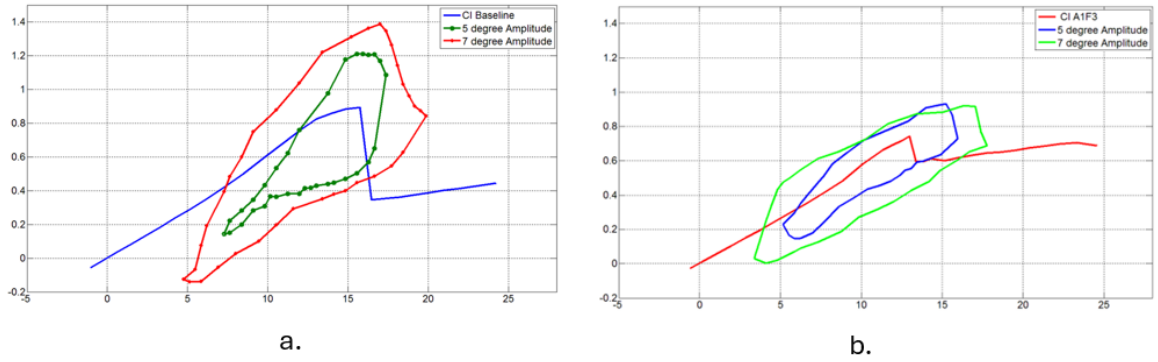

Figure 2.11: Lift coefficient vs angle of attack graph for the dynamic pitching of a. straight LE wing and b. tubercled LE wing [17]

2.4.3. Finite span wings - straight leading-edge, unsteady aerodynamic conditions

The flow mechanisms and characteristics of a tip vortex trailing a stationary wing are fairly well documented, but as Chang and Park [28] show, the evolution of the tip vortex in the case of an oscillating wing is less documented, even though this is an important study case for numerous applications such as helicopter rotors or wind turbine blades. Chang and Park's is an experimental study using Hot Film Anemometry with a triple hot -film probe, investigating the unsteady velocity and vorticity fields in the region of the tip vortex downstream of an oscillating, simple, rectangular wing with a symmetric NACA0015 airfoil, at the reduced frequency of $k = 0.09$ and a Reynolds number of $Re = 3.4 \times 10^4$. Their experimental setup is shown in Figure 2.12a and it is important to note that they imposed on the wing a sinusoidal oscillation of amplitude 15° centred around 15° (i.e. oscillating between 0° and 30°).

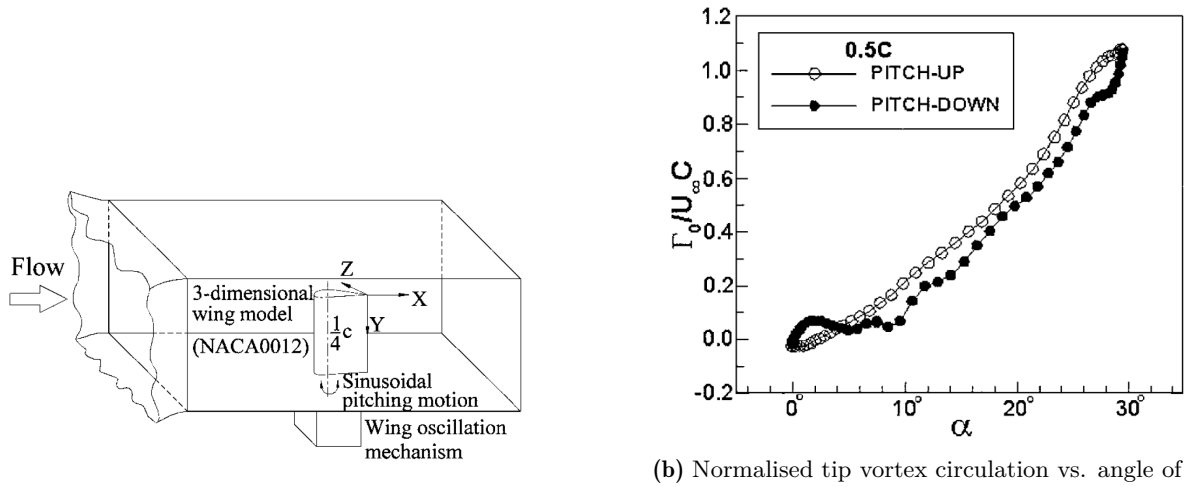

(a) Experimental setup

(b) Normalised tip vortex circulation vs. angle of attack graph at 0.5 chord lengths downstream

Figure 2.12: Results from the experimental study of Chang and Park [28]

Their study shows the vortex region is always suffering from a velocity deficit, which they attribute to the low Reynolds number. This velocity deficit increases with the angle of attack, but the deficit region widened and the magnitude of the deficit decreased during the downstroke, which is attributed to better flow mixing during pitch down. Lastly, the normalised tip vortex circulation is measured at a station half a chord length downstream of the wing and plotted in Figure 2.12b. This exhibits the expected hysteretic behaviour, because tip vortex circulation varies proportionally to the lift.

A similar experimental study was carried out by Birch and Lee [29] with a triple hot-wire probe downstream of a finite wing based also on the NACA0015 profile and also at a reduced frequency $k = 0.09$, but at an order of magnitude higher Reynolds number than the previous study, namely $Re = 1.85 \times 10^5$. They imposed on the wing a sinusoidal oscillation of amplitude $A = 6°$ centred around 18° (i.e. oscillating between 12° and 24°). The tip vortex circulation is normalised in the same way and exhibits a similar behaviour to the Chang and Park study, as shown in Figure 2.13a.

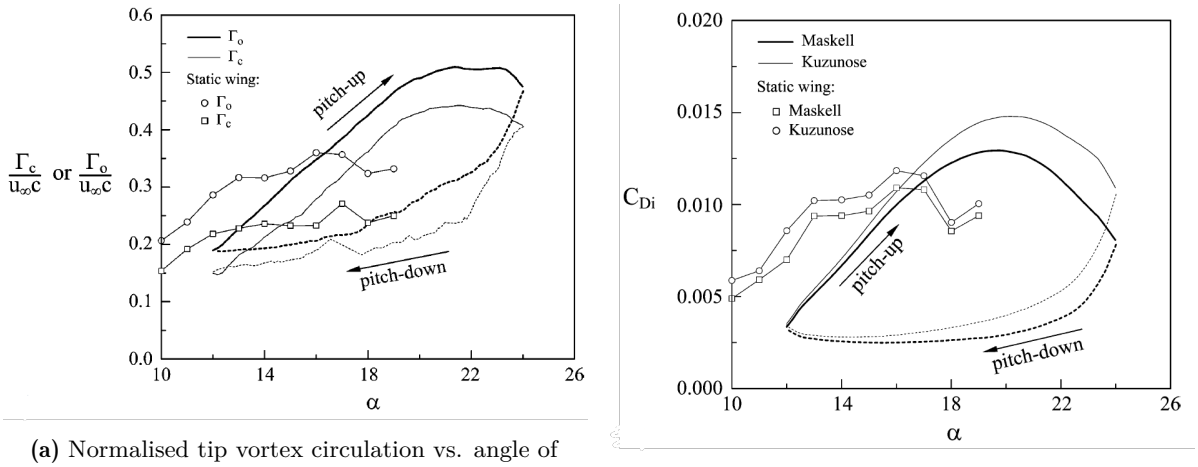

(a) Normalised tip vortex circulation vs. angle of attack graph downstream of the wing

(b) Induced drag coefficient vs. angle of attack graph

Figure 2.13: Results from the experimental study of Birch and Lee [29]

Of note from this study is that they also provide a useful method for computing the induced drag. Birch and Lee use the Maskell induced drag model [30] to compute the induced drag coefficient based on the vorticity inferred from the measured velocity field. This results in the graph shown in Figure 2.13b. What is also interesting from these studies is that both make use of phase averaging to obtain straighter

and higher quality data for comparisons, as their anemometry results tend to be quite noisy due to the unsteady nature of the flow.

2.4.4. Overview of previous experimental methods

An overview of the experimental methods used by previous studies available in literature on wings with leading-edge tubercles is shown below in Table 2.1. While it does not include all previous tests, it offers a good understanding of what flow measurement and visualisation techniques were available to studies in the past. Most studies have relied on obtaining force measurements to draw conclusions about the performance of tubercled wings and a few have applied various (planar) velocimetry methods to gain an understanding into the velocity field and flow structures involved with leading-edge tubercles.

Authors	Year	2D or 3D	Model	Conditions	Flow Measurement Techniques
H. Johari, C. Henoch, D. Custodio, A. Levshin	2007	2D	NACA63-021 base airfoil	Steady	force measurements, tufts
J. Hrynuk and D. Bohl	2020	2D	NACA0012 base airfoil	Unsteady	Molecular Tagging Velocimetry (MTV)
D. Custodio, C.W. Henoch, H. Johari	2015	3D	rectandular finite wing and flipper model	Steady	force measurements, Laser Doppler Velocimetry (LDV)
G.Moscato, J. Mohamed, G.P. Romano	2022	3D	rectangular finite wing and flipper model	Steady	planar Particle Image Velocimetry (PIV)
S.J. Reid, R.E. Perez,A. Asghar	2019	3D	rectangular finite wing	Steady	force measurements, tufts and oil visualisation
D.S. Miklosovic, M.M. Murray, L.E. Howle	2007	3D	rectangular finite wing and flipper model	Steady	force measurements
J. Borg	2012	3D	rectangular finite wing	Unsteady	force measurements

Table 2.1: Overview of literature on tubercle studies using experimental methods

Thanks to the infrastructure and know-how available at the TU Delft, the main method of investigating the effect of the tubercles and answering the research questions will be using 3D Particle Tracking Velocimetry (which will be referred from now on as “PTV”). 3D PTV is an advanced flow measurement technique that involves tracking the movement of seeding particles within a fluid over time and space, enabling the precise measurement of fluid flow characteristics in three dimensions.The working principle of the method will be further detailed in Subsection 3.2.3.

2.4.5. Overview of previous computational methods

The PTV data will be complemented by and compared to data obtained through CFD simulations of the same models under the same flow conditions. Ultimately, the current research aims to include transient CFD simulations of the sinusoidal pitching to better understand the vortex dynamics of this complex system and to obtain force values that will complement the experimental data. An overview of the previous studies on wings with leading-edge tubercles that have made use of computational methods is shown in Table 2.2.

Authors	**Year**	**Title**	**2D or 3D**	**Model**	**Computational Method**
H.T.C. Pedro, M.H. Kobayashi [25]	2008	Numerical Study of Stall Delay on Humpback Whale Flippers	3D	Flipper model	DES
P.W. Weber, L.E. Howle, M.M. Murray, D.S. Miklosovic [24]	2011	Computational Evaluation of the Performance of Lifting Surfaces with Leading-Edge Protuberances	3D	Flipper model	U-RANS
I. Fernandes, Y. Sapkota, T. Mammen, A. Rasheed, C.L. Rebello [16]	2013	Theoretical and Experimental Investigation of the leading-edge Tubercles on the Wing Performance	3D	Rectangular finite wing	RANS
Cai, Zuo, Maeda, Kamada, Li, Shimamoto, Liu [23]	2017	Periodic and Aperiodic Flow Patterns Around an Airfoil with Leading-Edge Protuberances	2D	Rectangular full-span wing	U-RANS
R. Colpitts, R.E. Perez [2]	2023	Application of Leading-Edge Tubercles on Rotor Blades	3D	Canonical Caradonna and Tung rotor geometry	U-RANS

Table 2.2: Overview of literature on tubercle studies using computational methods

It is clear from the literature that the unsteady nature of the flow due to the tubercles requires at least a transient Reynolds-Averaged Navier-Stokes simulation to accurately resolve the problem with some even using DES or LES which resolve the larger eddies as well. The CFD simulation campaign

will therefore rely on transient RANS (also known as U-RANS, for unsteady) simulations usinga k-ω SST turbulence model. Because of the availability through the university, capability, ease of use and post-processing and not least knowledge of the author in using this piece of software, Ansys CFX will be used as a solver. The simulations will be defined in Ansys CFX-Pre and will be post-processed initially using Ansys CFD-Post.

2.5. Applications

Having summarised the effects leading-edge tubercles have on the flow and the kind of known and potential performance effects they produce, it is worth mentioning a few other applications besides the already stated helicopter (or wind turbine) blades.

Because tubercles are accepted to delay stall and extend the lift curve to much higher angles of attack, they are the perfect solution for control and stabilization surfaces such as rudders of both air and sea vehicles, sailboat keels and skegs and various fin stabiliser applications. In the automotive realm, they can be used for their counter-rotating vortices generating effect in applications such as mirror covers, wing endplates or even for the actual downforce producing wings of racecars. One good example is the MP4-29 Formula One racecar entered by the McLaren team in the 2014 season. The second element (or the flap) of the rear wing had a tubercle leading-edge, which can be seen in Figure 2.14 as tool to generate streamwise vortices washing the suction surface of the wing, while not violating minimum radius of curvature or sharp edges rules imposed by the sport's governing body that would make conventional vortex generators illegal. This is most likely done to maintain the flow attached at higher angles of attack and to extend the angle of attack envelope of the wing, as the angle changes due to the pitch of the racecar.

Figure 2.14: McLaren MP4-29 with tubercle leading-edge on the 2nd element of the rear wing [2]

[2] http://www.somersf1.co.uk/2014/07/bite-size-tech-mclaren-mp4-29-new.html

2.6. Research focus

2.6.1. Research gap

By collecting the information that has gone into writing the previous chapters of this literature study report to explain the aerodynamic issues of pitch oscillations and how leading-edge tubercles are a potential solution, a research gap can be identified. Some of the existing, relevant, literature is summarised in Table 2.3 . Only one previous study has been found that investigates the effects of LE tubercles of finite wings undergoing pitch oscillations, but that focuses primarily on the force measurements without investigating the flow structures such as the streamwise tubercle vortices or the effects these have on the tip vortex. Furthermore, only one other study was found that focuses on the use of tubercles in the unsteady regime. This study is focused on a 2D analysis of wings undergoing a rapid ramp-up motion, rather than the sinusoidal oscillation that is found in systems such as rotor blades, as shown in Subsection 1.1.1. One of the more recent studies that investigates tubercled finite wings, but under steady conditions, Moscato et al. [26] even offers the following recommendation: "The present analysis *[i.e. 3D wings, steady conditions]* must be extended to the evaluation of flow fields and performances in unsteady conditions when preliminary indications suggest an even better situation in comparison with standard wings."

Existing research	Steady conditions (with tubercles)	Unsteady conditions (with tubercles)	Unsteady conditions (without tubercles)
2D (airfoil)	[14]	[31]	[32] (among others)
3D (finite wing)	[18] [26] [27]	[17]	[29] [2] [8]

Table 2.3: Overview of existing research and gaps

Therefore, a research gap is identified in the study of the flow structures, in particular that of vortices, and of flow mechanisms involved in periodically pitching finite wings with leading-edge tubercles.

2.6.2. Research questions

The questions that the current research will focus on are:

1. Do the LE tubercles extend the usable angle of attack envelope of finite wings subjected to sinusoidal pitch rate oscillations?
2. How do the streamwise vortices of the LE tubercles interact with the tip vortex under unsteady conditions?
   (a) How do tubercles influence the spanwise distribution of velocities in compartments?
   (b) Are tip and bound vorticity affected by tubercles?
3. Is the induced drag of a finite wing with LE tubercles reduced compared to a SLE wing?

Furthermore, for all three research questions, the impact of two parameters will be investigated, listed in order of priority:

- How does the reduced frequency of the oscillation influence these parameters?
- How does the tip end condition influence these parameters?

3

Methodology

3.1. Overview

3.1.1. Test matrix

To answer the research questions, a test matrix needs to be elaborated, containing the model variables and aerodynamic parameters to be varied.

3.1.1.1. Chosen model geometries

The baseline wing will be a simple, rectangular, straight-cut at the tip wing, with the same airfoil shape throughout, namely the NACA0021 airfoil. The choice of a symmetrical airfoil is justified by the simple and known characteristics in steady conditions, as well as similarity to real life applications such as most helicopter rotor blades [1]. The rather thick airfoil with a 21% thickness-to-chord ratio was chosen both to maintain continuity with previous experiments undertaken in the Aerodynamics department of TU Delft, but also to provide enough space for the 3D printed structure reinforced by carbon spars to be reliably manufactured. This also provides ample torsional and bending rigidity which is a particular point of interest when dealing with an oscillating, cantilevered beam setup. Furthermore, other previous studies have used the NACA0021, such as Borg in 2012 [17].

The planform shape was chosen in order to accurately focus on the effects of tubercles and those of tip end condition and not introduce complications by unknown influences of taper or sweep angle on the effectiveness of the tubercles. The half-wing aspect ratio of 4 chosen for the baseline is aligned with previously undertaken experimental research that usually varies the aspect ratio with values between 3 an 5.

In total, three 3D-printed rectangular wing models will be used: one with a straight leading-edge and two with tubercles, but different end conditions as shown in Figure 3.1. Their relevant geometrical characteristics are summarised in Table 3.1.

Geometrical characteristics	
Base Airfoil	NACA0021
Chord	100 [mm]
Half-span	400 [mm]
Tubercle amplitude	10 [mm]
Tubercle wavelength	25 [mm]

Table 3.1: Overview of geometrical characteristics of the model wings

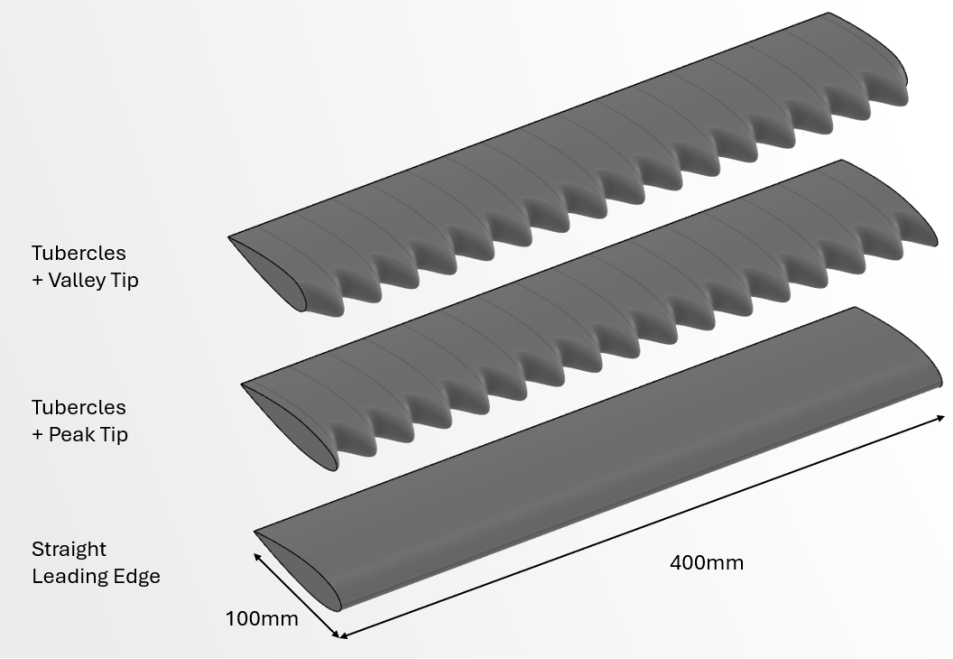

Figure 3.1: The 3 wing models that will be studied - own drawing

Since the goal of the current study is not to optimise the shape of the tubercles, but rather to gain an understanding of their effects in specific conditions, the chosen tubercle shape will not be altered. The only tubercle shape being applied was chosen to follow the same parametrisation method presented earlier in Section 2.2. In planform, they represent a sinusoide of amplitude $A_{tub} = 10mm$ and wavelength $\lambda = 25mm$. In cross-section, the shape is constrained in CAD in such a manner that all airfoils blend back together to the original NACA0021 by the point of maximum airfoil thickness. as can be seen in Figure 3.2.

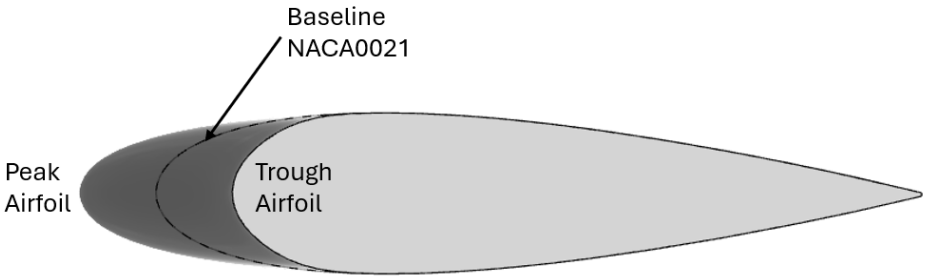

Figure 3.2: Cross-section view of the tubercle wing showing the airfoil shape variation between peak and trough - own drawing

3.1.1.2. Chosen test parameters

In order to build a test matrix, it is worth understanding what parameters need to vary in order to answer the research questions and whether there are limitations on what can be tested. In order to understand whether the tubercles extend the usable angle of attack envelope, which is the first research question in Subsection 2.6.2, a series of oscillations imposed on the wings, each with a larger amplitude. From helicopter literature, as shown in Subsection 1.1.1, it is clear that the angle of attack varies approximately sinusoidally, usually not dropping below 0°, and centred around a non-zero mean angle of attack, but the maximum angles vary throughout literature. Furthermore, the typical regime of the oscillation is at a reduced frequency $k = 0.1$. Therefore, the following 3 oscillations will be tested, plotted in Figure 3.3.

$$\alpha(t) = 5° + 5° \times sin(2\pi ft - \frac{\pi}{2}) \tag{3.1}$$

$$\alpha(t) = 10° + 10° \times sin(2\pi ft - \frac{\pi}{2}) \tag{3.2}$$

$$\alpha(t) = 15° + 15° \times sin(2\pi ft - \frac{\pi}{2}) \tag{3.3}$$

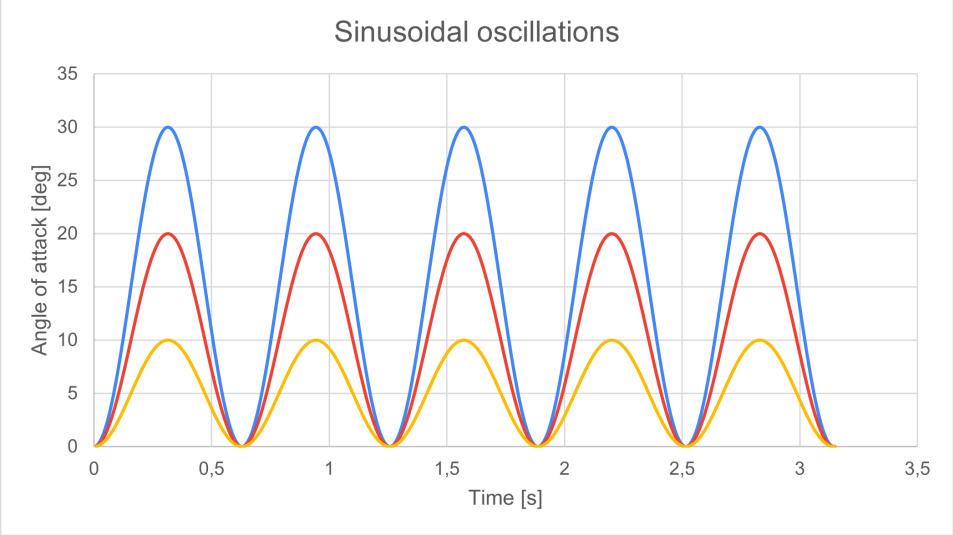

Figure 3.3: The 3 sinusoidal angle oscillations of the testing campaign

In the equations above, f stands for the actual frequency the rotating actuator will oscillate at. In order to obtain $k = 0.1$, the actuator will have to oscillate at $1.59Hz$ if the wind tunnel flow velocity is $5m/s$. Furthermore, to quantify the effect of the reduced frequency on the performance of the tubercles, $k = 0.2$ will be obtained by oscillating at $3.18Hz$. To double the freestream velocity and obtain a higher Re, the actuator would have to oscillate at above $6Hz$, but it is limited in its capabilities to a $5Hz$ oscillation at the biggest amplitude, therefore the wind tunnel speed will be kept at $5m/s$ for all measurements. It is important to state that, taking into account as characteristic length the chord length of the baseline wing, the experiments are characterised by a chord Reynolds number of $Re = 3.3 \times 10^4$. Finally, for the purposes of CFD tuning and validation, a quasi-static measurement will be taken for each wing by sweeping from 0° to 30° angle of attack at a very low $k = 0.01$. All of this is shown in Table 3.2, representing the test matrix which will be performed both in the tunnel and in CFD.

Run nr.	Shape	Frequency f [Hz]	Reduced frequency k [-]	Max Angle [deg]	Code name
1	Valley Tip	0,159	0,01	30	OS_valtip_k001_30
2	Valley Tip	1,59	0,1	10	OS_valtip_k01_10
3	Valley Tip	1,59	0,1	20	OS_valtip_k02_20
4	Valley Tip	1,59	0,1	30	OS_valtip_k01_30
5	straight leading-edge	0,159	0,01	30	OS_straight_k001_30
6	straight leading-edge	1,59	0,1	10	OS_straight_k01_10
7	straight leading-edge	1,59	0,1	20	OS_straight_k01_20
8	straight leading-edge	1,59	0,1	30	OS_straight_k01_30
9	Peak Tip	0,159	0,01	30	OS_peaktip_k001_30
10	Peak Tip	1,59	0,1	10	OS_peaktip_k01_10
11	Peak Tip	1,59	0,1	20	OS_peaktip_k01_20
12	Peak Tip	1,59	0,1	30	OS_peaktip_k01_30
13	Peak Tip	3,18	0,2	10	OS_peaktip_k02_10
14	Peak Tip	3,18	0,2	20	OS_peaktip_k02_20
15	Peak Tip	3,18	0,2	30	OS_peaktip_k02_30

Table 3.2: Test matrix

In the rest of the report, for the sake of brevity, the three different shapes will be referred to as SLE for the wing with a straight leading-edge, ValTip for the wing with tubercles ending in a valley tip and PeakTip for the one with tubercles ending in a tubercle tip shape, respectively.

3.2. Experimental Study

Now that the general flow of the parallel studies was presented, the current section will detail the experimental setup and measurement acquisition methodology that was used to understand the flow behaviour around pitching finite wings with tubercles. Subsection 3.2.1 will deal with the specifications of the wind tunnel and its limitations. Then, the way the wind tunnel models were designed, manufactured and pre-tested will be detailed in Subsection 3.2.2. The full experimental setup designed for 3D PTV image acquisition is explained in Subsection 3.2.4. Finally, Subsection 3.2.5 delves into the algorithms and post-processing scripts used to analyse the experimental data, as well as into the validation of said tools based on results from literature.

3.2.1. Wind tunnel

The wind tunnel testing campaign was undertaken in the W-tunnel, part of the High Speed Laboratory facility at the TU Delft and shown in Figure 3.4. The W-tunnel is an open-loop, subsonic wind tunnel that, with a $0.6 \times 0.6m$ test section, that can practically only reach velocities of up to $15m/s$.

Figure 3.4: W-Tunnel at the TU Delft HSL [33]

An important aspect for both the experimental results, but also for the later tuning and validation of numerical simulations, is the turbulence intensity that the W-tunnel can achieve. According to TU Delft data, the tunnel can achieve a minimum of 0.5% turbulence intensity, but that is in its "cleanest" configuration[1]. For the current experiment, a large soap bubble seeding rake was placed, which is bound to increase the turbulence intensity, however, data on this value is not available from previous studies.

3.2.2. Experimental models

3.2.2.1. Computer-Aided-Design modelling

The three model wings were designed in CAD, using the 3DExperience software available to students of TU Delft. As explained previously, in Subsubsection 3.1.1.1, the shape of the tubercles is defined by a sinusoidal curve. In CAD, this is done by defining the leading-edge guide as a 3D equation-driven curve, as shown below in Figure 3.5. Together with two straight spanwise guides that define the points of maximum thickness of the base NACA0021 airfoil, the sinusoidal leading-edge guide is used to define a multi-section surface that forms the tubercle leading-edge. This is constrained to be tangent to the multi-section surface that defines the trailing portion of the wing, shown highlighted in blue in Figure 3.5, in order to make sure that the shape has blended back to the original one by the maximum thickness point of the wing.

[1] `https://www.tudelft.nl/lr/organisatie/afdelingen/flow-physics-and-technology/facilities/low-speed-wind-tunnels/w-tunnel`

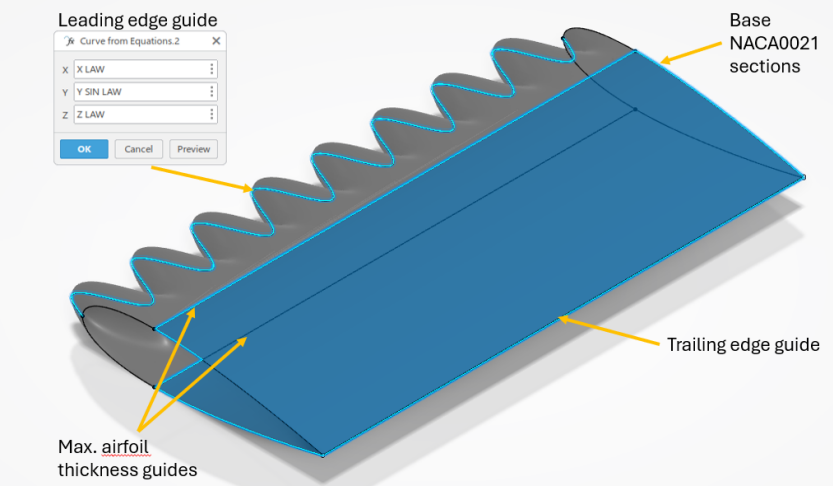

Figure 3.5: CAD representation of wing model wireframe construction

The mechanical assembly of the wing models is also designed in CAD and shown below in Figure 3.6. The wing models consist of a 3D printed plastic shell, reinforced by two carbon spars. These have each an aluminium insert glued-in at the root end of the wing. These threaded inserts receive two M5 bolts that attach the wing to a CNC-ed aluminium adapter. Both the inserts and the adapter are manufactured by the technicians of the High Speed Laboratory in the workshop at the TU Delft. The adapter makes the mechanical connection between the wing model and the rotating actuator, a Zaber RSB [2]. The rotating stage is bolted to the polycarbonate wall of the wind tunnel test section. More importantly, attached to the adapter and the rotating assembly is a digital encoder that converts the measured angle motion into a digital signal. As will be explained later, in Subsection 3.2.4, this is used for both triggering the image acquisition and for verifying the motion of the actuator.

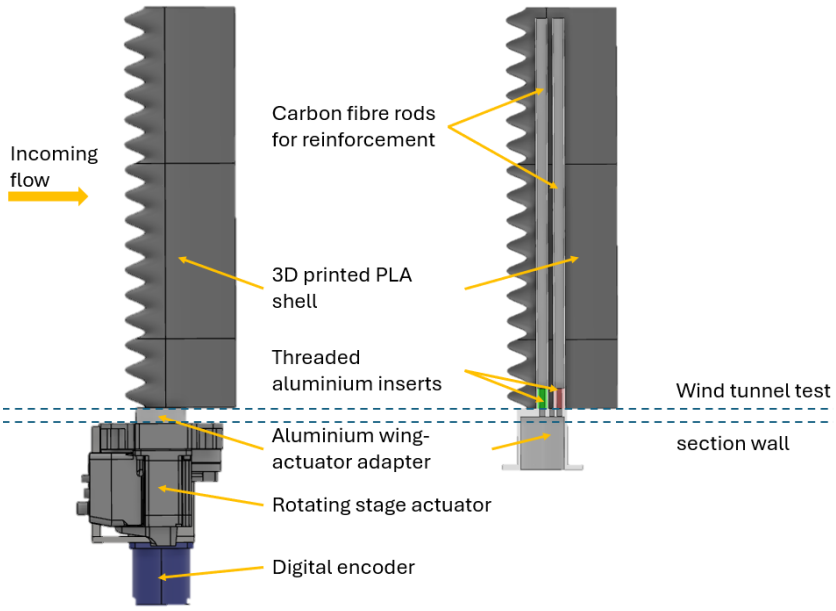

Figure 3.6: CAD representation of wing model attachment and inner structure

3.2.2.2. Model manufacturing

After designing in CAD, the models were manufactured by FDM (Fused Deposition Modelling) 3D printing. This was done on a Creality Ender 5 Pro commercially available 3D printer, out of PLA

[2] https://www.zaber.com/products/rotary-stages/RSB

(polyactic acid, one of the most common types of plastic used for 3D printing). The wings were each printed in 2 vertical sections of half a span each, such that the layers would end up being aligned with the flow and with a thin tetrahedral infill, as shown in Figure 3.7a, with a layer height of 0.2mm. Through the structure, two hollow cylinders were left for the reinforcing pultruded carbon fibre spars, shown inserted in a test printed section in Figure 3.7b.

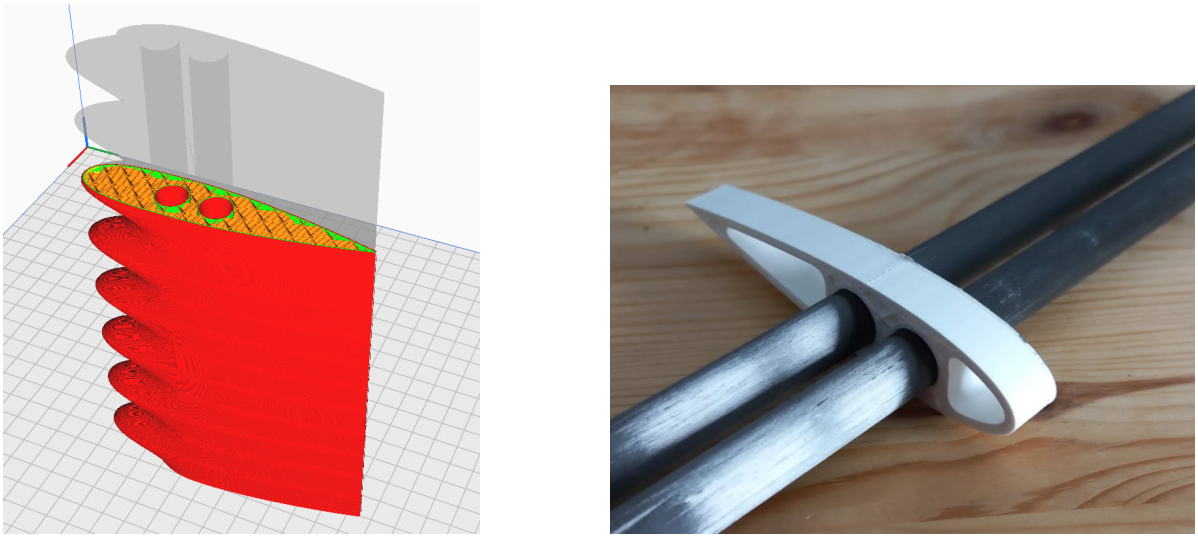

(a) 3D printed wing inner structure

(b) Trial wing section with the carbon rods inserted

Figure 3.7: Wing model manufacturing steps

After printing the wing sections, spars and inserts were assembled and glued together using epoxy resin. Finally, the models were wet-sanded by hand down to a 400 grit sandpaper and spray painted matte black in order to avoid light reflections from the surface, then a further step of sanding and another coat of paint were repeated.

3.2.3. Background on the 3D PTV method

The core of the experimental study on the effects of leading-edge tubercles consists in analysing the flow using Particle Tracking Velocimetry (or PTV). To understand the advantages and limitations of this method, as well as why the setup was designed in a specific manner, a short dive into the background of the method is necessary.

3.2.3.1. Tomographic PIV

For the study of three-dimensional flows with the full characterisation of the velocity field at every instant, 3D or tomographic PIV (Particle-Image-Velocimetry) is used. Below, Figure 3.8 shows a schematic depiction of its working principle, as introduced by Elsinga, Scarano and van Oudheusden [34]. The flow is seeded with tracer particles, typically bubbles. These are illuminated by a pulsed light source, in the region of interest to the study. The resultant scattered light pattern is simultaneously captured from multiple viewing angles using CCD (Charge-Coupled Device) cameras. Ensuring all particles within the entire volume are sharply imaged involves setting an appropriate $f_{\#}$. The 3D distribution of particles (the object) is then reconstructed as a three-dimensional light intensity distribution from their projections on the CCD arrays. Subsequently, the displacement of particles (and thus velocity) within a chosen interrogation volume is determined through the three-dimensional cross-correlation of the reconstructed particle distribution between two exposures. To establish the correspondence between image (projection) coordinates and physical space (the reconstruction volume), a calibration process is required. This consists of camera capturing images of a calibration target (for example a checkerboard with known dimensions) at various depths throughout the volume, allowing the calibration procedure to ascertain the viewing directions and field of view. Accurate triangulation of views from different cameras forms the basis of tomographic reconstruction.

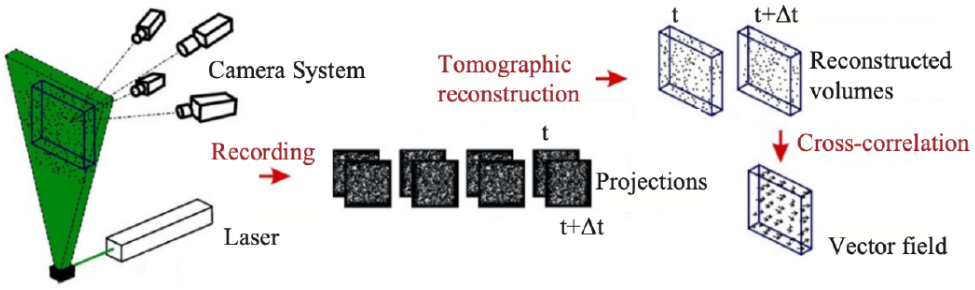

Figure 3.8: Setup and method of tomographic PIV [34]

3.2.3.2. Lagrangian Particle Tracking with the Shake-The-Box algorithm

Particle Tracking Velocimetry (PTV) is a slightly different method to PIV as it relies on Lagrangian particle tracking, which consists of tracking individual tracer particles in a three-dimensional volume. [35]. Traditional tomographic PIV cross-correlation methods, described in Subsubsection 3.2.3.1 necessitate substantial memory and computational resources. They are only effective with low particle image densities (0.05 particles per pixel), as higher densities result in overlapping ghost particles that degrade reconstruction accuracy. This limitation arises from treating each time instant individually, where the intensity distribution is represented in a 3D interrogation box. Cross-correlation is then applied to voxels to reconstruct the velocity field. Additionally, spatial averaging on the voxels hampers visualisation of smaller structures and flattens spatial gradients. To address these issues, a novel algorithm based on Lagrangian particle tracking, such as Shake-The-Box (STB), has been developed. STB utilizes spatial and temporal data to predict particle trajectories from PIV images, correcting tracer positions and eliminating ghost particles. This robust particle tracking algorithm is suitable for high-density tracer particle images.

Schanz et al. [35] outlines the development and application of the Shake-The-Box (STB) technique for Lagrangian particle tracking. This innovative approach is grounded in leveraging temporal information to predict particle distribution for subsequent time steps, combined with an image matching technique to rectify prediction errors and iteratively triangulate particles entering the measurement domain. The STB method, whose working principle is shown in Figure 3.9, is also sometimes called '4D-PTV' for its capability of resolving the temporal dimension very well. It enables the identification of particle trajectories with high spatial accuracy, significantly reducing the occurrence of ghost particles. The shake-the-box method will be used when post-processing the images acquired in the current study's experimental campaign to accurately characterise the flow structures at every timestep of the very fast oscillation.

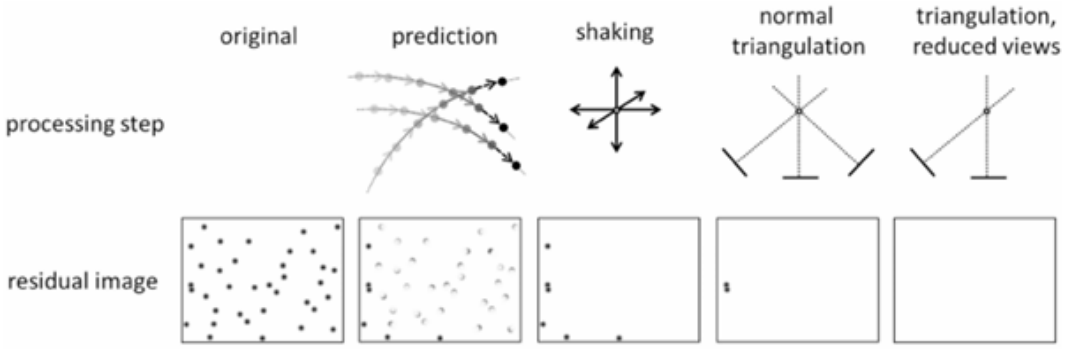

Figure 3.9: Schematic of STB working principle by showing the effect on residual reduction [35]

3.2.4. Experimental setup for 3D PTV acquisition

3.2.4.1. Particle tracer seeding

The current experiment makes use of a particular seeding technology that injects helium-filled soap bubbles (HFSB) into the flow. The management of pumping and pressurising the helium, air and soap liquid supplies is done with the in-house developed Fluid Seeding Unit (FSU), shown in Figure 3.10a. These three component fluids are pumped and injected into the flow through a seeding rake (Figure 3.10b) placed in the settling chamber of the wind tunnel.

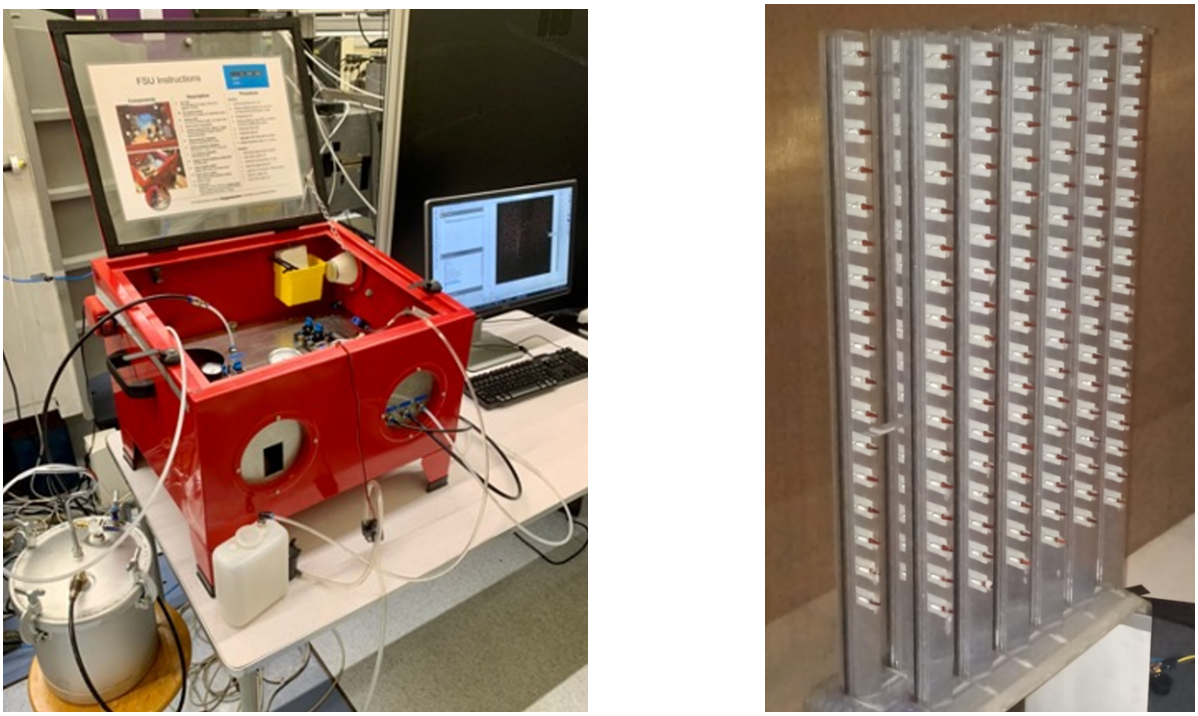

(a) Fluid Seeding Unit (FSU) **(b)** Seeder rake

Figure 3.10: Equipment required for seeding the flow with HFSB

Every red tip on the seeding rake in Figure 3.10b is a nozzle that combines the flow of air, helium and soap, as shown in the detail section-view in Figure 3.11.

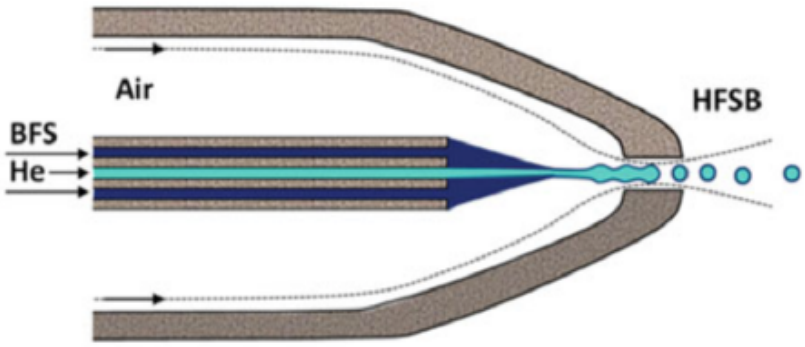

Figure 3.11: Detail of seeding rake nozzle and its component capillaries [36]

3.2.4.2. Optical setup

The image acquisition setup consists of four Photron Fastcam SA1.1 high speed cameras. The sensor of this type of camera has a resolution of 1024x1024 pixels and a maximum frequency of acquisition of 5400Hz [3]. In order to increase the maximum number of images that can be stored in the cameras' internal memories, the sensor is cropped using the Davis software to a 768×1024 pixels resolution which translates to a maximum number of 7276 images that can be recorded in one run. In the current experiment, images are acquired at 2000 Hz. Considering the frequency of the wing's oscillation and the maximum memory of the cameras, this translates to 5 full cycles of the $k = 0.1$ (i.e. 1.59 Hz) oscillation and 10 full cycles of the $k = 0.2$ (i.e. 3.18Hz) oscillation that can be recorded in one run.

As shown in Figure 3.13, the cameras are placed in a horizontal line, at approximately 1m distance from the object (wing), with angles between them of at most 37°. Each camera uses a Nikon 60mm lens. As explained in Subsubsection 3.2.3.1, in order to achieve good focus of the particles and a suitable field of view, in the lighting conditions provided by two high power LEDs visible in Figure 3.13a, an $f_{\#} = 16$ is used. This offers a field of view corresponding to a measurement volume of 270mm x 340mm x 160mm (in x,y,z respectively) focusing on the tip region of the wing, visualized in the context of the coordinate system in Figure 3.12a.

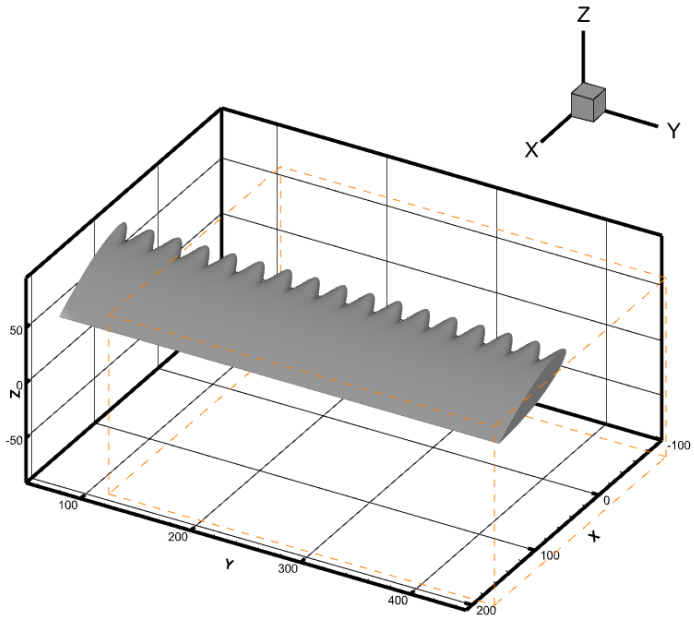

(a) Coordinate system and experimental measurement volume (dashed, orange lines)

Experimental Optical Parameters		
Parameter	**Value**	**Unit**
Sensor size	1024×1024	pixels
Cropped sensor size	768×1024	pixels
Acuqisition frequency	2000	Hz
Max. camera memory	7276	images
$f_{\#}$	16	-
FOV x-size	270	mm
FOV y-size	340	mm
FOV z-size	160	mm

(b) Experimental optical parameters summary

[3] https://techimaging.com/products/legacy/legacy-high-speed/product/photron-fastcam-sa1-1

3.2.4.3. Full setup and procedure

The experimental setup is shown in Figure 3.13

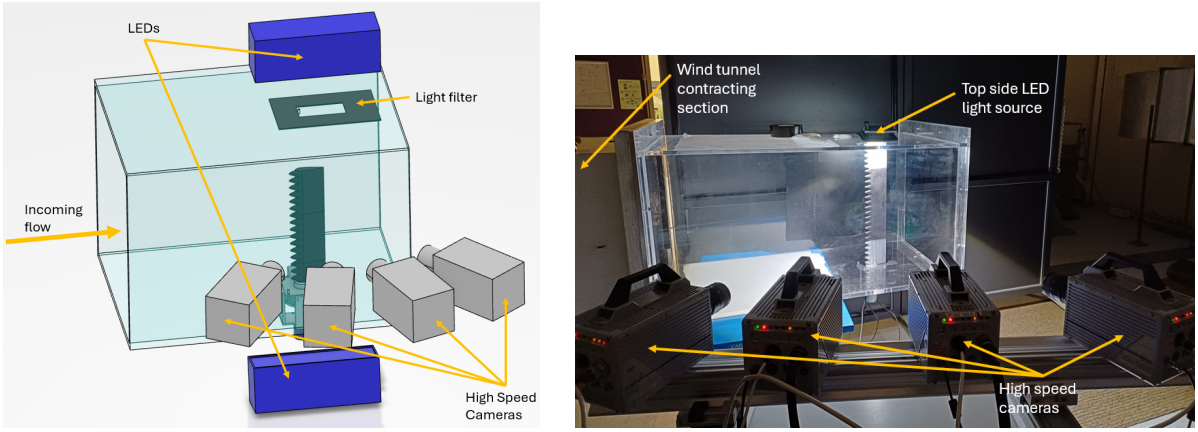

(a) Setup in CAD **(b)** Setup in the W-Tunnel

Figure 3.13: Full experimental setup

Such a complex array of cameras, lights and actuators is complex to coordinate. The operating procedure for one measurement run occurs as follows:

1. The actuator and wing model are homed at zero angle of attack and the encoder reading is zeroed;
2. The wind tunnel power is turned on and the RPM setting adjusted until the velocity stabilises at $5m/s$;
3. The flow seeding is turned on, by opening all the fluid lines of the FSU; once the bubbles are visibly filling the test section volume, the measurement can begin;
4. The motion of the wing is started by running the Python code that controls the rotating actuator;
5. A LabView program reads the encoder measurement of the instantaneous angle value and when it reads a positive 0.05° it sends a signal to the Programmable Timing Unit (PTU);
6. The PTU then sends signals triggering the LEDs and signals triggering the image acquisition of the cameras; the cameras than continously record until they fill their internal memories (7276 frames);
7. The recording stops, as well as the motion;
8. The bubble seeding is turned off, followed by the tunnel and everything is reset for the next run.

The accurate triggering of the LEDs and camera recordings by the PTU based on encoder readings is crucial for ensuring that all the measurements begin at the same time point. This allows for much easier post-processing of the data. Because the start time of the first oscillation is known, phase-averaging the cycles is easier, as well as positioning the data in the context of the wing geometry and animating the wing motion which is necessary for reliable data visualisation.

3.2.5. PTV data post-processing

3.2.5.1. Calibration and OTF

As briefly explained in Subsection 3.2.3, for 3D PTV to be possible a camera volume calibration is needed, through which the X, Y and Z planes are mapped to the cameras' CCD. In the current experiment, a pinhole fit was performed, by taking photos of a 2D (planar) calibration plate with black and white dots. In the centre of the plate, 3 dots are disposed in an L-shape that helps the software define the x-axis and y-axis of the coordinate system. In Figure 3.14, a set of such images is shown after the dots have been identified by the Davis software and the relative angles of the cameras with respect to each other are clearly visible in the way the photos are skewed.

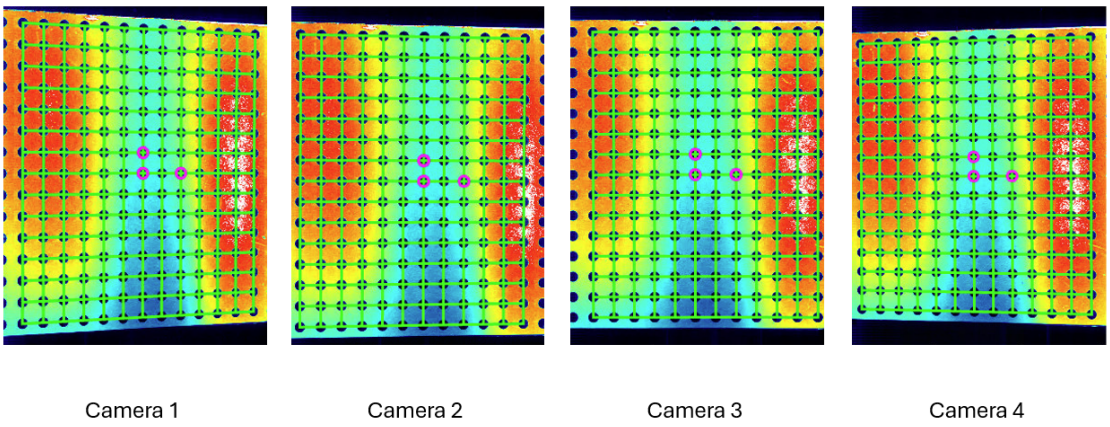

Figure 3.14: Camera calibration photos based on a planar plate with dots

After the camera geometric calibration, a Volume Self-Calibration (VSC) was performed. This is meant to remove any remaining residual disparities between cameras. It is based on images of the flow tracer particles in freestream, without a model placed in the tunnel test section. It involves calculating the disparity vector map, which is then used to correct the perspective calibration. According to the Davis 10.2 software manual [4], the disparity vectors indicate the errors in the perspective calibration due to the lines of sight of a single particle from the different cameras that do not intersect in a single point in space.

One VSC was performed at the start of the set of wind tunnel runs of each of the three wings, based on the flow tracers particle images. After a number of refinement iterations, the resulting calibration was accepted. Then, the Optical Transfer Function (OTF) was calculated, setting the allowed triangulation error equal to 1 to ensure that only the best fitting tracer particles are used for the OTF calculation.

3.2.5.2. Shake-the-box (STB)

For the Lagrangian particles tracking, the algorithm used is the Shake-The-Box (STB). This requires the Volume Self-Calibration (VSC)and Optical Transfer Function (OTF). The parameters used in the present study for the STB algorithm to produce particle tracks are shown in Figure 3.15. These are the result of a compromise between the number/density of tracked particles and the quality/noise of the resulting tracks. The STB algorithm was ran for the entire measurement volume, with particles only being tracked if their intensity peak is higher than 100 counts. Furthermore, a maximum allowed triangulation error was set to 0.5 voxel.

The velocity limits were chosen in order to find all the particles required to fully characterise the flow, knowing that phenomena such as reversed flow and a strong tip vortex are to be expected. Therefore, they were chosen as: $V_x = 5 \pm 9m/s$, $V_y = 0 \pm 6m/s$ and $V_z = 0 \pm 6m/s$.

[4] `https://www.lavision.de/en/downloads/software/`

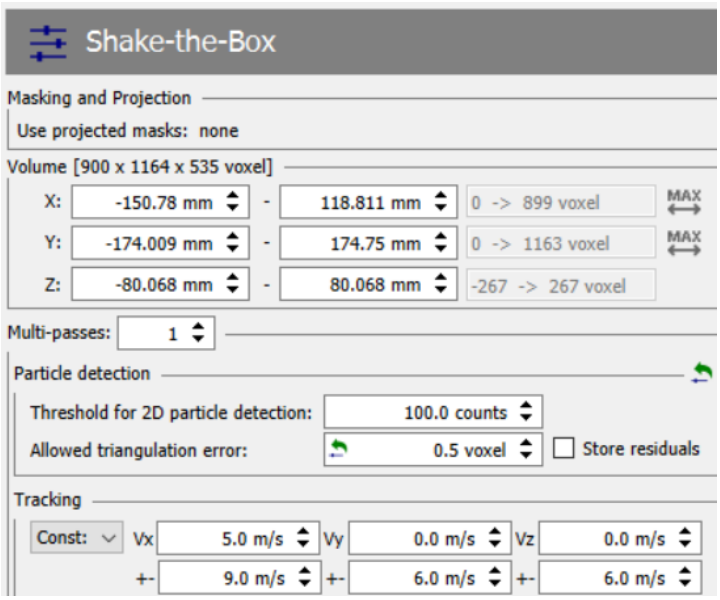

Figure 3.15: Final STB parameters used to obtain the particle tracks

3.2.5.3. Binning

In order to understand the evolution of the flow field over time, data about the instantaneous flow field is required. This is done by grouping the particles from the resultant particle tracks from STB into time and space through a process called binning. This is essentially a local averaging process on small regions of time and space.

Through binning, the velocity from Shake-the-Box track data is converted to a regular grid. Spatial bins are defined in Davis by 3D cubic volumes called "subvolumes" with dimensions expressed in voxels, which are essentially just volumetric pixels. An overlap between the subvolumes is also specified as a percentage. For binning, all tracks in the vicinity of a grid point are used to calculate the velocity at this point. The contribution of a track to this grid point is weighted by the distance of the track from the grid point, using a Gaussian weighting function. With the current setup, 1mm in the data is equivalent to 3 pixels in the image. Therefore a 30 voxels subvolume is equivalent to a cube with a 30 pixels (or $10mm$ side). With an overlap of 83.33%, this results in a resolution of 5 voxels or approximately $1.6mm$.

The time component of binning is defined by the so-called filter length, expressed in frames. As mentioned previously, the current study acquired 2000 frames per second, therefore a filter length of 20 frames is equivalent to grouping in one bin the data contained within $0.01s$. It is also important to view this in the context of the oscillation: the $k = 0.1$ reduced frequency oscillation has a period of $0.63s$. This is relevant in picking the filter length, because one does not want to average over to big a percentage of the oscillation, as information about the instantaneous flowfield and its evolution will be lost.

The final binning parameters that were used are shown in Figure 3.16.

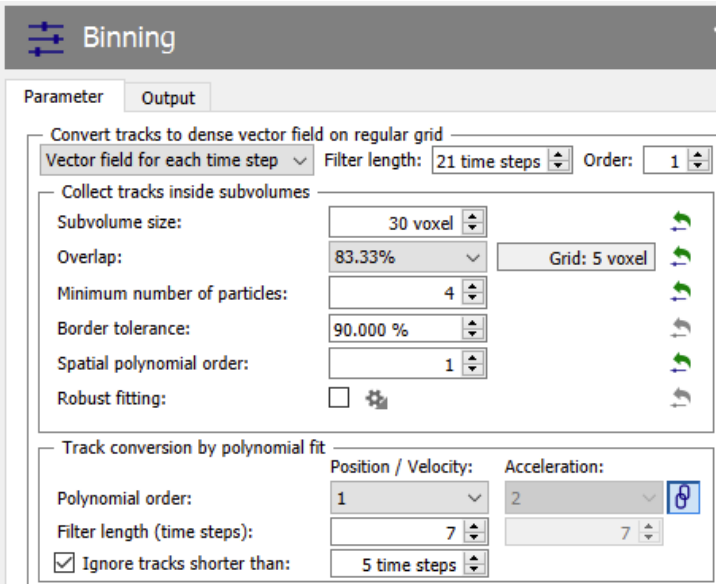

Figure 3.16: Final binning parameters used for visualisation of the instantaneous flow field

3.2.5.4. Phase averaging (+ binning)

In the context of the current study, the same pitching cycle is repeated for a maximum of 5 times during a measurement recording window. Certain aerodynamic phenomena are repetitive and occur at approximately the same time and the same location during every oscillation cycle. For such phenomena, phase averaging can be utilised. This consists of averaging the flow properties, in this case the velocity field, over multiple cycles of the same oscillation. This process produces results that emphasize the coherent and repeatable flow phenomena, by increasing the density of available data points in a certain region of the cycle. Phase averaging removes, however, the transient effects, the flow phenomena that occurs differently from cycle to cycle. Therefore, one must avoid the pit fall of trusting phase averaged data without checking the flow evolution within each individual cycle.

In the present study, phase averaging has been employed by using an externally developed code that takes the resultant particle tracks after STB and exports the averaged vector field as a Tecplot360-readable *.plt* file. The code for phase averaging that was used in the present study was developed by Mitrotta, Sodja and Sciacchitano [37] and further modified by Cueto Corral [38] and is publicly available online [5].

The spatial and temporal binning parameters used post-phase-averaging are the same as for the instantaneous flow field, namely cubic volume bins of 10mm and overlap 75% and time bins of 0.01s.

In the current study, phase averaging has proven to be extremely useful for improving the quality of data and emphasizing the vortical structures associated to the finite wing with tubercles. The location and moment at which both the streamwise tubercle vortices and the tip vortex of the wing are shed varies very little from cycle to cycle. Therefore, as shown in the figure below, it is clear that phase-averaging results in a less noisy, smoother flow field without holes that can be used to understand the general trend of the vortices throughout the oscillations.

[5] `https://github.com/pcuetoco/STB-Phase-Average?tab=readme-ov-file`

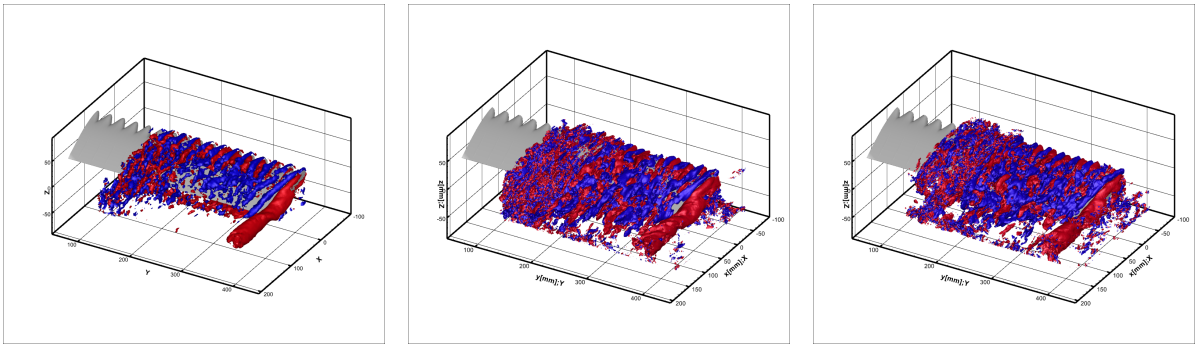

(a) Phase-averaged **(b)** Instantaneous, cycle 1 **(c)** Instantaneous, cycle 2

Figure 3.17: Isometric view of $\omega_x \cdot c/U_\infty = -3$ iso-surface in blue and $\omega_x \cdot c/U_\infty = +3$ iso-surface in red for the PeakTip wing at $k = 0.1$ and $\alpha = 20°$, pitching up, from experimental data

One example where phase averaging hides relevant information about the flow field is the evolution of the separated flow region, particularly in the case of the tubercle wings. Stall is triggered at the tubercle through locations due to induced upwash, as explained in Subsection 2.3.3.

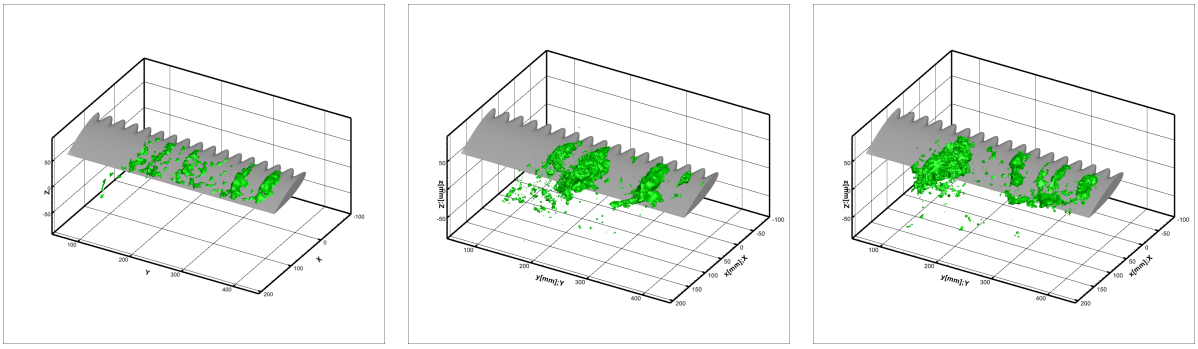

(a) Phase-averaged **(b)** Instantaneous, cycle 1 **(c)** Instantaneous, cycle 2

Figure 3.18: Isometric view of $U = 0m/s$ iso-surface (green) at $k = 0.1$ and $\alpha = 20°$, pitching down, from experimental data

3.3. Computational study

3.3.1. Meshing

The process of meshing starts from the CAD geometry of the wings. The process of designing these is detailed in Subsection 3.2.2. The choice to reproduce the wind tunnel conditions dictates the size of the domain, namely a 0.6x0.6 m cross-section. Furthermore, the inlet and the outlet are both placed at 0.3m upstream and downstream of the wing. The model is exported as watertight geometry.

3.3.1.1. Mesh generation

The chosen method for meshing is the generation of an unstructured, tetrahedral mesh, using Ansys Fluent. This allows for fast mesh alterations and accurate modelling of the very complex 3D shape of the wing with tubercles. A section view of the mesh showing the tetrahedral cells filling the domain around the wing is shown in Figure 3.19

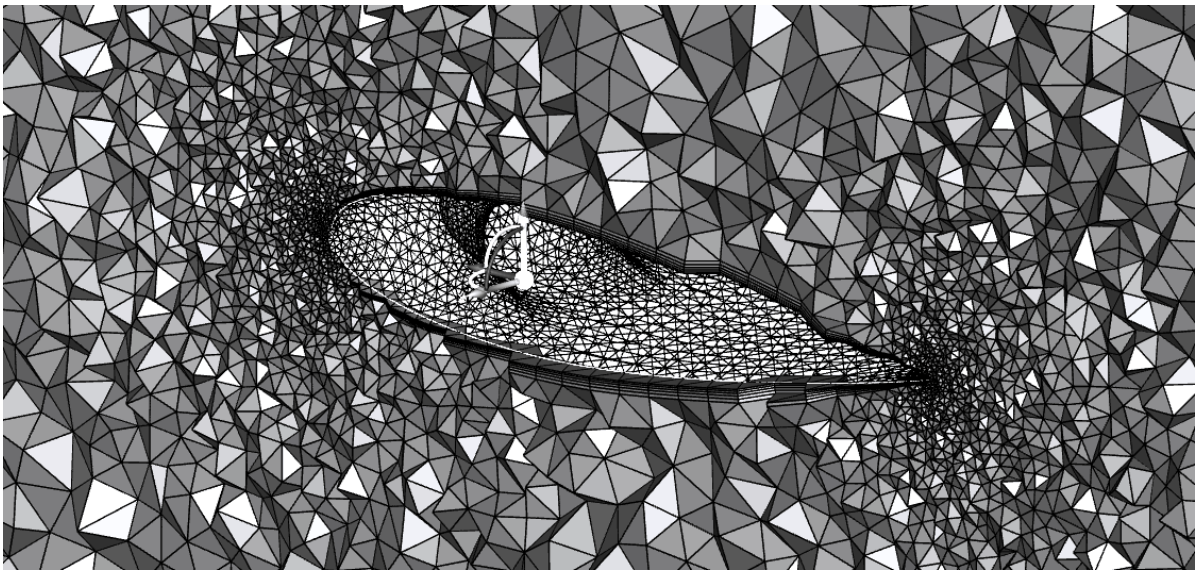

Figure 3.19: Section view of the mesh showing domain filled with tetrahedral cells

In order to achieve a $y+$ smaller than 1 in the boundary layer of the wing and fully solve the flow, rectangular cell refinement layers were added over the wing surface as shown in Figure 3.20.

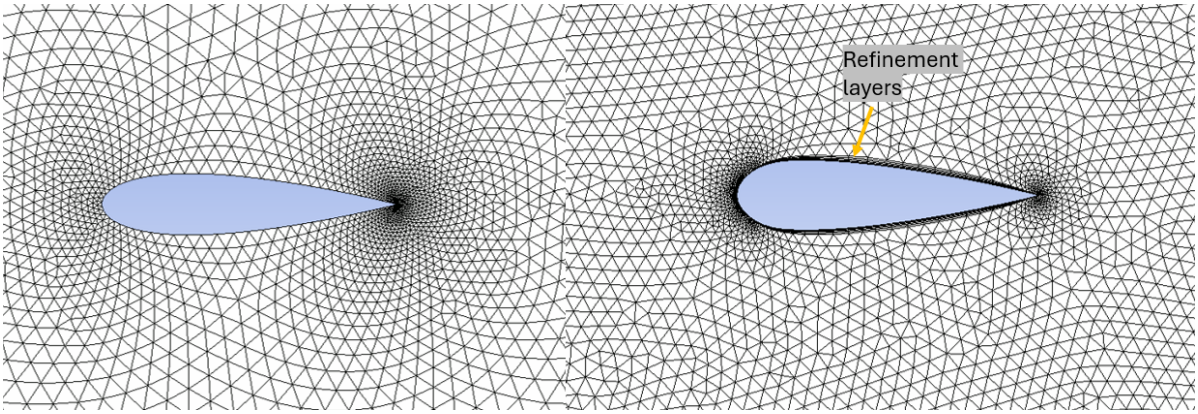

Figure 3.20: Mesh section detail in the proximity of the wing surface

3.3.1.2. Mesh deformation

In order to replicate the sinusoidal pitch oscillation of the wing in CFD, the mesh needs to be adjusted for every time step. This can be achieved by deforming the mesh. In the present study, this is done by specifying the location of the new mesh nodes at every time step as a rotation around the Z-axis of the initial mesh, using the *"Regions of Motion Specified"* function of CFX-Pre. According to the "Ansys CFX-Solver Modelling Guide", the actual mathematical method used by CFX-Pre in this case is that of *displacement diffusion*. This model takes the displacement imposed on a domain boundary and diffuses it to the surrounding mesh points by solving the following equation:

$$\nabla \cdot (\Gamma_{disp} \nabla \delta) = 0 \tag{3.4}$$

Where is δ represents the displacement over the timestep and Γ_{disp} represents the mesh stiffness. According to the CFX-Pre documentation, the mesh stiffness determines the degree to which the movement of regions of mesh points is linked together. The displacement diffusion model is designed to preserve the relative mesh distribution of the initial mesh. For example, if the initial mesh is relatively fine in certain regions of the domain (for example, in boundary layers), then it will remain relatively fine after solving the displacement diffusion equation. In the present study, the mesh stiffness is using the *"Increase Near Small Volumes"* setting. Increasing the stiffness near small mesh volumes has the positive effect that mesh quality will be retained by having more of the mesh rotation be absorbed by the larger control volumes, i.e. mesh quality will be retained in the denser regions around the wing's leading and trailing edges and more of the motion will be undertaken by the big cells in the farfield.

In the present study, the rotation equations in cartesian components, shown in Figure 3.21a, are imposed at the wing boundary and are a function of the instantaneous angle. This is formulated as an expression in CFX-Pre (Figure 3.21b) and has the value of the sinusoidal oscillation function specified earlier in Subsection 3.1.1.

(a) Mesh motion parameters

(b) Expressions governing mesh motion

Figure 3.21: Overview of mesh deformation control

All of the settings described until now allow the mesh to retain its quality and be deformed from 0° to 30° and back down to 0° while being able to have a well converged solution. The minimum (initial mesh) and maximum extent of the deformation can be seen below in Figure 3.22.

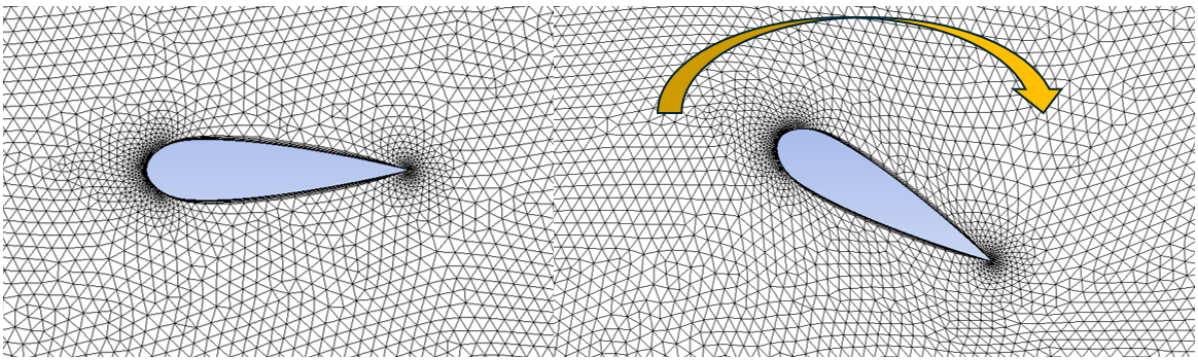

Figure 3.22: Section view of initial mesh and maximum deformed mesh around the wing boundary

3.3.2. Solver

The solver software used in this study is Ansys CFX. Because the original motivation for the numerical study was to complement the experimental method with force measurements and more detailed flow structure, the domain replicates the wind tunnel test section exactly, as shown in Figure 3.23. All the outside walls were modelled as no-slip, smooth, walls, in order to try to model some of the blockage effects of their boundary layers as happens in the wind tunnel, in real life. The wing was also modelled as a no-slip wall, but with a $0.2mm$ roughness size applied, equal to the layer height of the 3D printed model, as mentioned in Subsection 3.2.2.

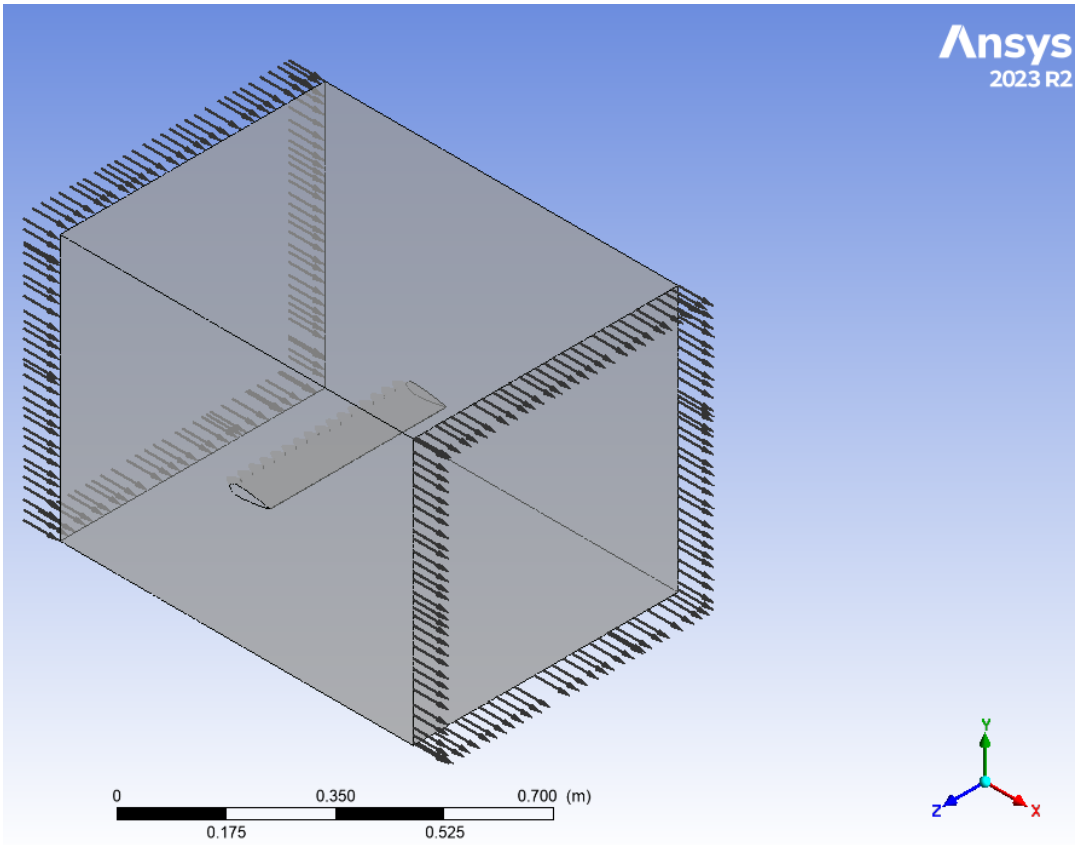

Figure 3.23: Simulation domain visualized in Ansys CFX-Pre with inlet and outlet highlighted

The inlet conditions were prescribed by the cartesian velocity components and a 5% turbulence intensity, shown in Figure 3.24. This turbulence intensity prescribed at the inlet, together with the wing roughness, have been found to be the combination of parameters that best models the flow separation ocurrence and propagation and were chosen for good correlation with the experimental results. It is also important to note the solver uses a $k-\omega$ SST turbulence model, as this has been used before by previous numerical studies on tubercle wings successfully, for example by Cai et al. [23] and it is generally known to work well in predicting flow separation [6].

[6] https://ntrs.nasa.gov/api/citations/20090042511/downloads/20090042511.pdf

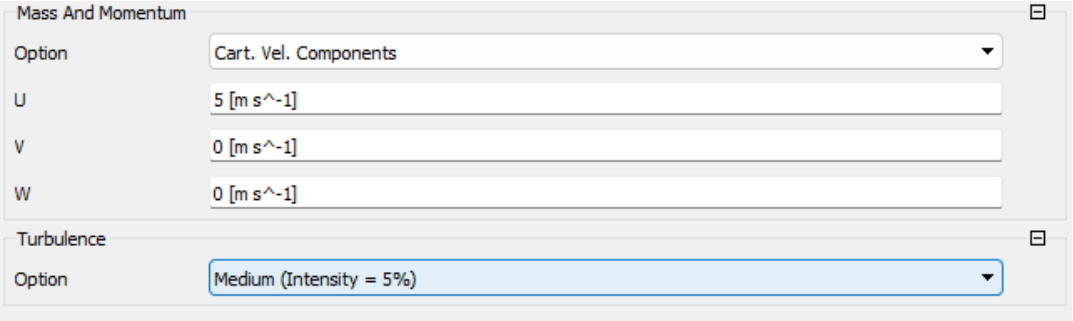

Figure 3.24: Inlet parameters

3.3.2.1. Transient solver parameters

In order to capture the dynamic effects of the pitching oscillation, together with the mesh deformation, a transient U-RANS (Unsteady - Reynolds Averaged Navier Stokes) simulation was used. This was run for a total physical time of $t_{total} = 0.629s$ (i.e. for one period of the oscillation) and with timesteps of $timestep = 0.001s$ in order to achieve RMS Courant number values below 5. The Courant number is a dimensionless measure of the number of mesh cells traveled by the flow at a given timestep, described by the equation below, where u is the freestream velocity, Δt is the timestep and Δx is the length between two consecutive mesh elements [7].

$$C = u\frac{\Delta t}{\Delta x} \tag{3.5}$$

Even though a smaller Courant number, usually below 1, is desired for good solutions of transient problems, computational time constraints meant in this case the timestep could not be made even smaller to reduce the Courant number, as the mesh could definitely not be coarsened, as was explained earlier in Subsubsection 3.3.2.2.

Furthermore, the inner convergence loop was run at every timestep until the maximum residual values all fell below 1×10^{-4} to ensure a good convergence of the solution.

[7] https://www.simscale.com/knowledge-base/what-is-a-courant-number/

3.3.2.2. Mesh refinement tests

The initial tests were performed in both steady and unsteady conditions with an approximately 5 million cells mesh generated as explained above. This produced the lift curves visible in Figure 3.25 and Figure 3.26a. The fact that the static lift curve was monotonously increasing for the SLE wing even after the usual maximum lift coefficient angle, as opposed to slightly dropping as is the expected behaviour at this Reynolds number, prompted an investigation into refining the mesh. Furthermore, the dynamic lift curves with this mesh showed a higher maximum lift coefficient for the tubercle wings which is against expectations, as they should not benefit from the lift overshoot provided by a coherent DSV, as will be further detailed in Chapter 5.

Figure 3.25: Effect of mesh refinement on steady-state lift curve

The addition of refinement layers as shown in Figure 3.20 and the reduction of cell size throughout the domain has resulted in an approximately 7 million cells mesh, that brought the lift curves closer to their expected physical behaviour. Namely, the static lift curve now shows the characteristic drop after $\alpha = 15°$ and in the dynamic curves the mesh refinement has resulted in a slightly higher lift for the SLE wing, which is definitely closer to expectations. Furthermore, this refinement has helped achieve a flow structure, including separated flow regions, that is well correlated with the experimental results, as will be further discussed in Chapter 4.

Perhaps, a further step of refinement, particularly around the wing tip and tubercle leading edge would have provided even more accuracy in the force measurements, but the solution time and computational resources were limited and this was considered sufficient, based on the good phenomenological correlation with experimental and theoretical results.

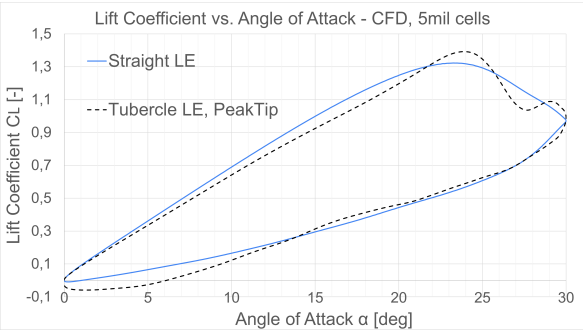

(a) Dynamic lift curves, 5 million cells mesh

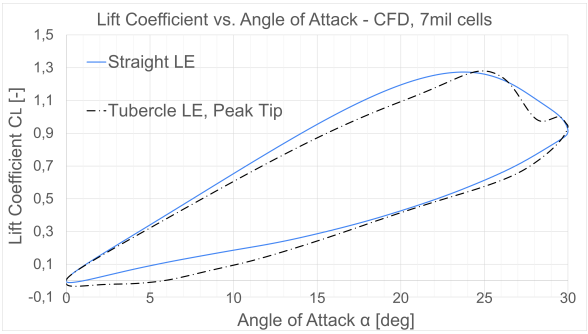

(b) Dynamic lift curves, 7 million cells mesh with refinement layers

Figure 3.26: Effect of mesh refinement on dynamic lift curves

4

Validation

4.1. Experimental method validation

4.1.1. Phenomenological validation

As part of the wind tunnel campaign, a quasi-static measurement (i.e. at a reduced frequency of $k = 0.01$) was taken for each of the wings to use for validation with previous static studies and for CFD correlation. The figure below, Figure 4.1 shows the results of the post-processing chain described above for the *ValTip* wing at $\alpha = 15°$, which is also the mean angle of the later-studied oscillation. The particle tracks were binned using a $\Delta_t = 0.01s$ temporal bin size. To represent the vortices of this system, the x-component of vorticity is normalised as follows:

$$\omega_{x_{norm}} = \omega_x \cdot \frac{c}{U_\infty} \tag{4.1}$$

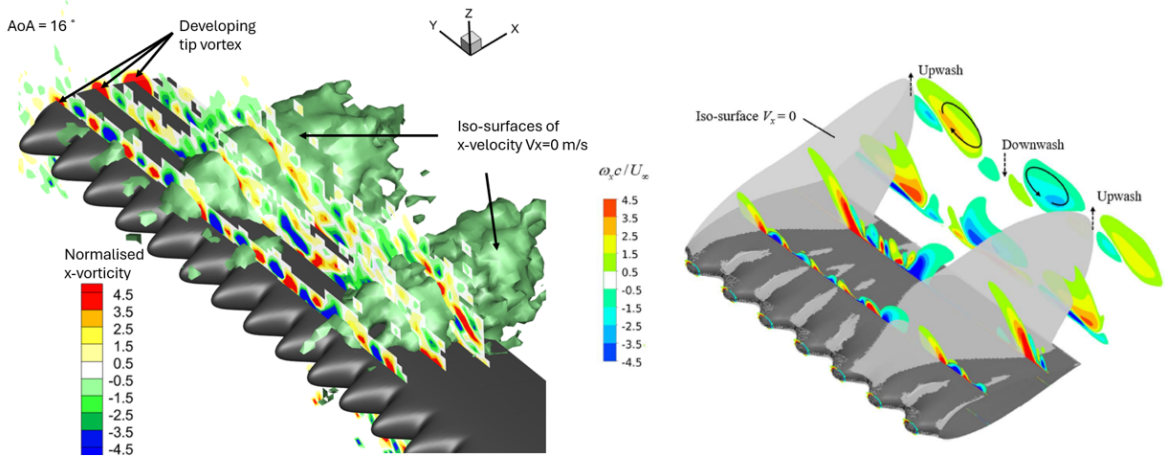

Figure 4.1: Comparison of stall cells and surrounding normalised streamwise vorticity between own results (left) and Cai et al. [23] results (right)

4.1.2. Quantitative validation

4.1.2.1. Tip vortex circulation

One way to quantitatively validate the experimental results is by computing the circulation of the tip vortex. Particularly for the SLE wing, this is proportional to the lift force of the wing, providing a crucial understanding of the evolution of the force over an oscillation cycle. Furthermore, there is experimental data available for SLE wings from previous studies to compare with.

The method consists in integrating the vorticity over a closed surface placed in the control volume. The mathematical basis is provided by Stokes' Theorem [9]. This relates shows that circulation is equivalent to the area integral of the curl of the velocity (i.e. the vorticity) over the chosen surface.

$$\Gamma = \oint_C \vec{V} \cdot d\vec{s} = \int\int_S (\nabla \times \vec{V}) \cdot \vec{n} \cdot dA \tag{4.2}$$

Therefore, to compute the circulation, a virtual circular surface was placed downstream of the wing at half a chord downstream of the quarter-chord point (axis system origin) and perpendicular to the freestream flow direction (i.e. x-axis is the surface normal) that encompasses the tip vortex at all times. The figure below, Figure 4.2 shows the graphical representation of this virtual surface in Tecplot360 applied on ValTip tubercle wing CFD data.

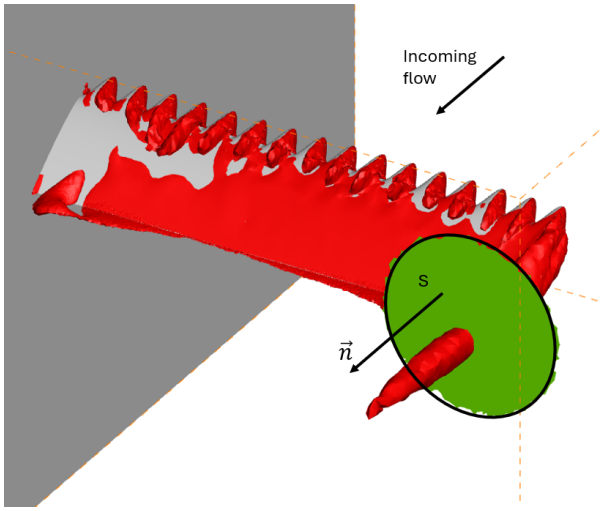

Figure 4.2: Visualisation of integration region, in green, in *Tecplot360*; the isosurface x-axis vorticity $\omega_x = 200[1/s]$ is displayed to locate the tip vortex

Performing this integration over the whole oscillation cycle produces the data shown in the graph below in Figure 4.3, overlapped with existing experimental data from Chang and Park's studies [28] which present the closest scenario to the current one that was found in literature. Namely, their study was performed on a comparable rectangular SLE wing (NACA0012, span of 60cm, chord of 15cm at a Reynolds number of $Re = 3.4 \cdot 10^4$). Furthermore, their oscillation is almost identical to the one used in the present study: a sinusoidal oscillation of amplitude 15° centred around 15° (i.e. oscillating between 0° and 30°) and at the reduced frequency of $k = 0.09$. It is clear from the comparison graph that the present data show a very similar slope and comparable values for both the upstroke and downstroke portions of the graph. The maximum value of circulations is slightly higher in the present study, most likely due to the slightly higher reduced frequency of $k = 0.1$ used (rather than $k = 0.09$) and due to the different airfoil shape used. Also, the hysteretical gap between the upstroke and downstroke values in the present values is likely bigger than the gap in the Chang and Park data due to the lower Reynolds number of the current study which is only $Re = 3.3 \times 10^4$.

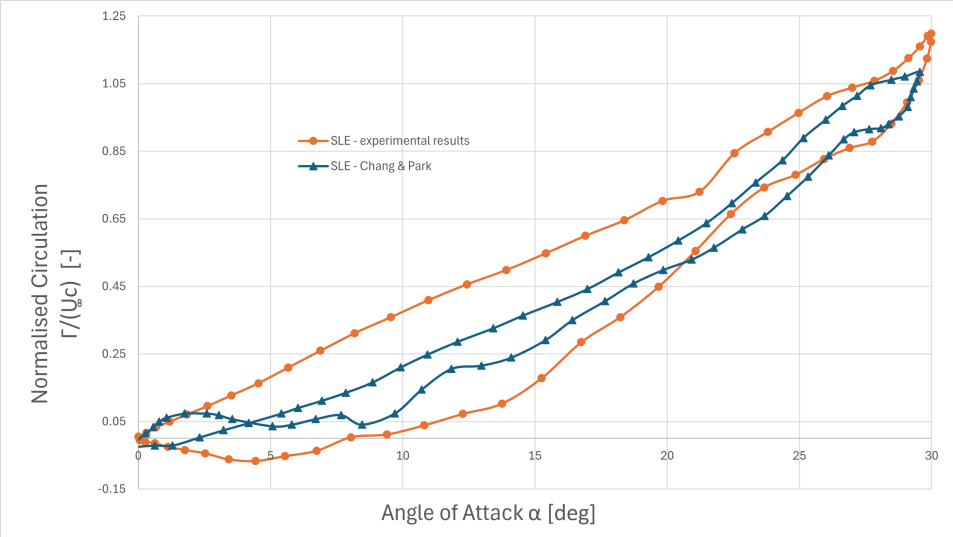

Figure 4.3: SLE wing tip vortex circulation comparison between own experimental results measured at $x/c = 1.5$ and Chang and Parks's [28] results.

4.2. Computational method validation

4.2.1. Phenomenological validation

Once a converged CFD set-up was reached, with the parameters explained in Section 3.3, validating the numerical results can also be done. First of all, Figure 4.4 shows that the CFD is able to replicate the flow structure very well, at least in steady conditions (fixed wing). In particular, the CFD is able to predict the existence of stall cells of a similar dimension to the one visible in experimental results and accurately placed at the tubercle trough locations. Furthermore, it is clear the alternating pattern of counter-rotating vortices shed by the tubercles is accurately predicted by CFD as well. More on the flow structure in the unsteady regime will be discussed in Section 5.2.

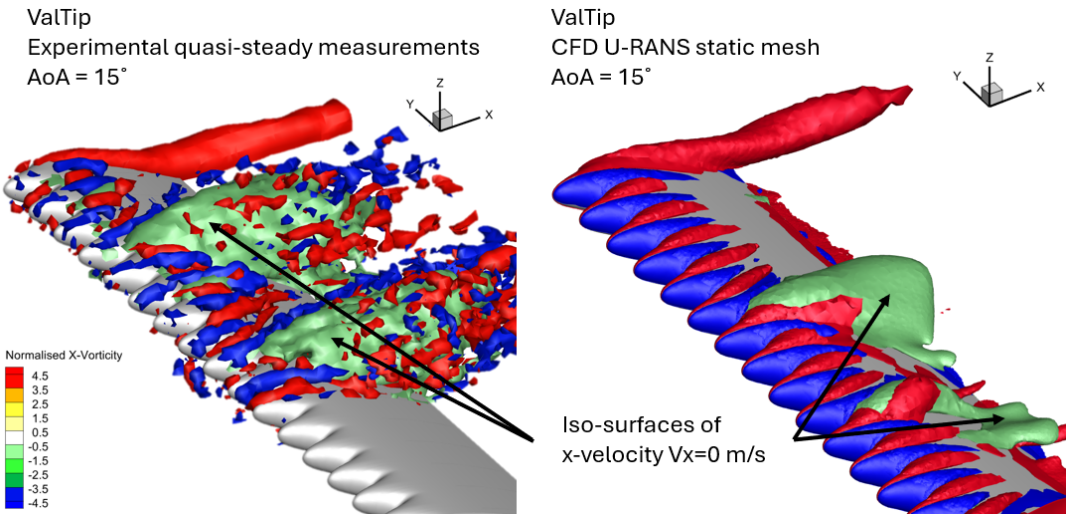

Figure 4.4: Comparison of flowfield structures ($\omega_x \cdot c/U_\infty = -4$ iso-surface in blue and $\omega_x \cdot c/U_\infty = +4$ iso-surface in red and stall in green) between experimental results (left) and CFD results (right) of the *ValTip* tubercle wing in steady conditions

The stall cells' location at the tubercle trough spanwise locations is justified by the difference in perceived (or effective) angle of attack between peak and valley locations. This was documented by previous steady studies, as shown in Subsection 2.3.3, but it is useful to see that the CFD results correlate well with the

theory. Axial velocity contour plots of two spanwise slices at peak and trough locations in Figure 4.5 show the smoother velocity gradient in the tubercle peak locations and the more adverse gradient in the trough locations that forces the separation to first occur at the troughs.

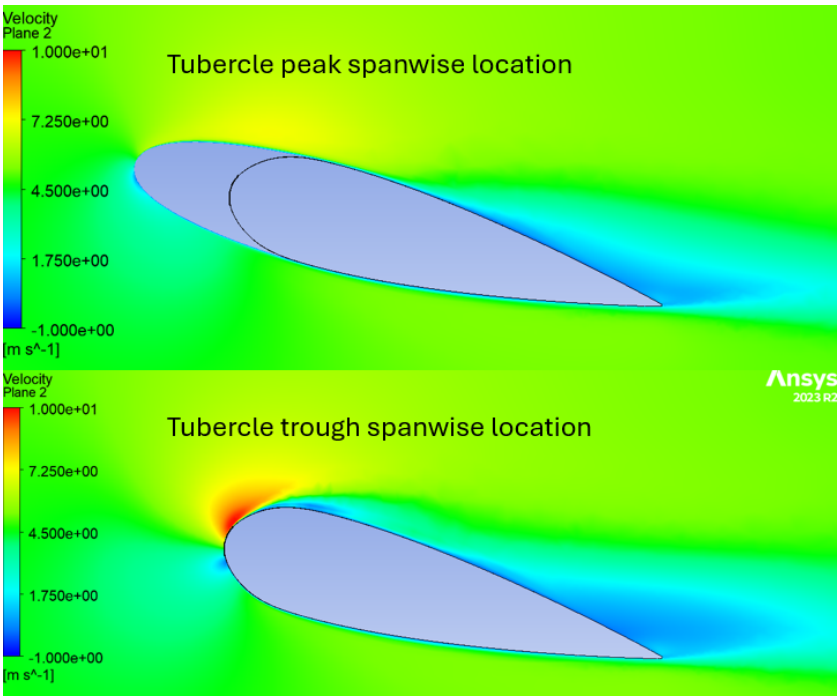

Figure 4.5: Comparison of contour plot of X-velocity at tubercle peak and tubercle trough locations from steady CFD results

4.2.2. Quantitative validation

The first type of quantitative validation conducted concerns a crucial result of the simulations: **the lift curve of the pitching wing**. For ease of comparison with literature, it was first conducted on steady-state simulations of the SLE wing and the ValTip tubercle wing, obtaining the graph shown below in Figure 4.6a.

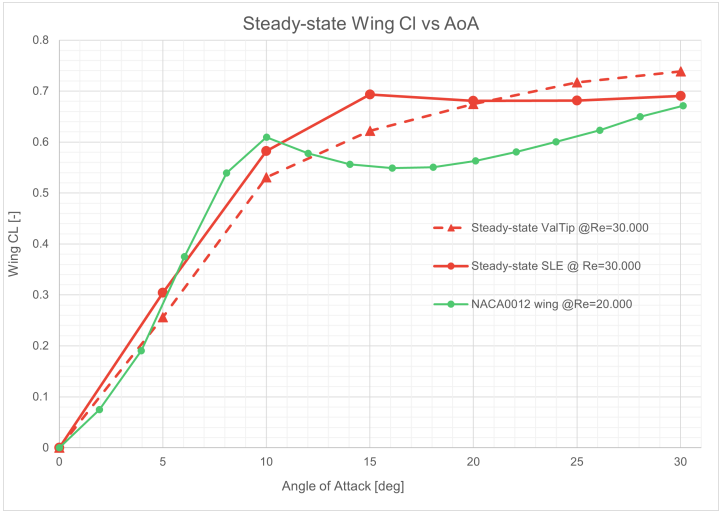

(a) Wing lift coefficient vs. angle of attack graph comparison between CFD results and results from Yasuda et al. [39]

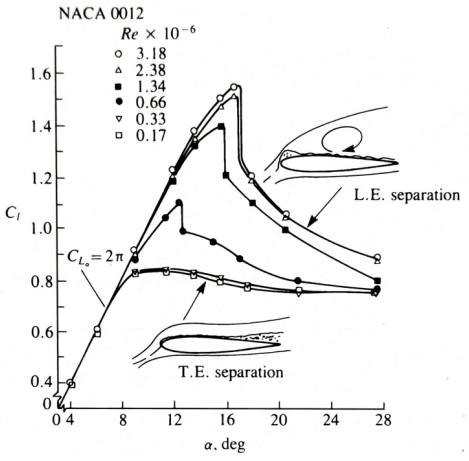

(b) Effect of Reynolds number on the lift coefficient of a NACA0012 airfoil [40]

Figure 4.6: Steady-state lift curves for low Reynolds numbers

A number of interesting observations can be made from the above lift curve. First of all, the SLE wing has a higher maximum lift coefficient which aligns with literature. It is perhaps surprising to note that the SLE lift curve only exhibits a subtle drop in lift coefficient after the $C_{L_{max}}$ point. This is explained by Winslow et al. [41] in their study on airfoil characteristics at very low Reynolds numbers: because the Re is so low in the current case (approx. $Re = 3.3 \times 10^4$) the laminar separatio point is delayed until close to the trailing edge of the wing, even at very low angles of attack, because of the increased stability of the boundary layer, which is more resistant to flow transition. As the angle of attack increases, the separation point moves toward the leading-edge, resulting in the airfoil being effectively in trailing edge stall for most of its operational range. That is also shown by the lift curve extracted from the study for a $AR = 6$ wing based on the NACA0012 airfoil, tested at $Re = 2 \times 10^4$, which is the closest found result from literature. The tubercle wing has a similar behaviour, also aligning in ballpark value and slope with the available literature, value shown in Subsection 2.4.1, even though most other studies are conducted in at least an order of magnitude larger Reynolds number regimes. Another useful source for understanding this flat lift curve behaviour is the study conducted by Ericsson and Redding [40] that produced the lift curves shown in Figure 4.6b.

4.3. Comparison between experimental and computational results

4.3.1. Parallel studies

The current study on pitching wings with leading tubercles consists of two parallel branches, one experimental and one numerical. While both methods were detailed in Section 3.2 and Section 3.3 respectively, it is important to present an overview of the whole process and how their results can be compared. Because several different pieces of software and methods are used, a bigger picture view is necessary to keep track of the operations executed on the data to reach a point where they can be compared directly to each other. This is presented in the flowchart in Figure 4.7.

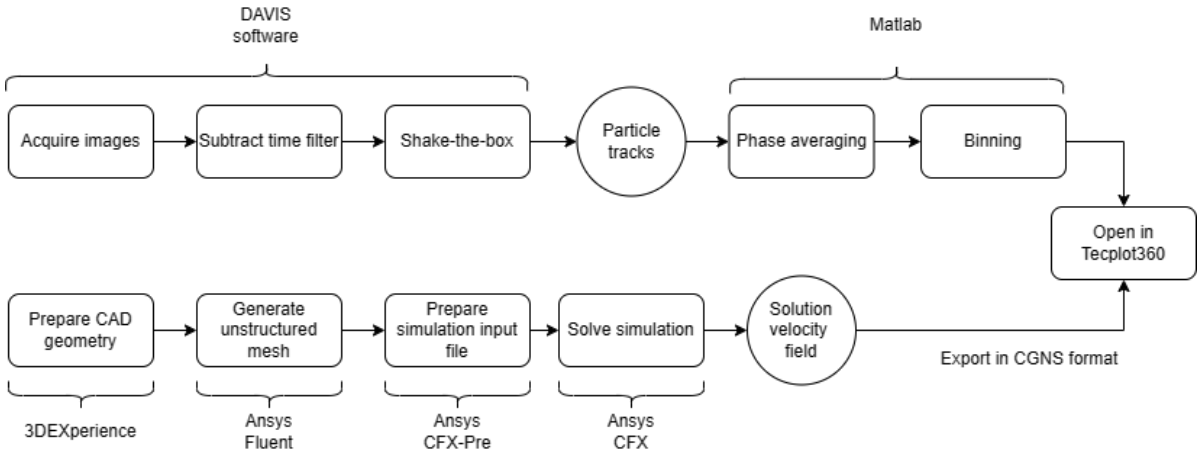

Figure 4.7: Flowchart of parallel experimental and computational methods procedures

The first branch, the experimental one, first makes use of the Davis software to acquire the photos of the particles injected in the airflow and to perform the initial post-processing that produces the particle tracks. After the velocity field around the wings is known, an externally-developed MATLAB algorithm is used to phase-average the data, making use of the multiple recorded cycles to improve the quality of the data, and to collect the particles into bins that allow for the smooth visualisation of data. Finally, this data is exported and aligned to the correct coordinate system in Tecplot360, where the comparison to numerical data is performed.

The numerical study branch makes use of the 3DExperience CAD software to design the models required to create the mesh. Then, the generation of an unstructured mesh, as well as the solving and initial postprocessing are performed using the Ansys software suite. The obtained velocity field is also exported in *.cgns* format to Tecplot360 where the comparison to the experimental data is performed.

4.3.2. Differences

Section 4.1 and Section 4.2 showed how the experimental and computational methods were validated by comparison to prior results available from literature. The more interesting comparison, however, is how the results of these two methods stack up against each other in the present study. The previous sections of this chapter have mostly touched upon how both methods reveal similar aspects of the flow field, but the present section deals with the differences, because there are a number of significant ones that need to be taken into account before drawing conclusions. Also, while this section deals with the differences between CFD and experimental results, the similarities will be discussed in more detail in Chapter 5, while exploring the evolution of the flow-field.

One difference that was observed throughout the data analysis is that the CFD underpredicts the values of vorticity. The iso-surfaces shown in Figure 4.8 are shown in blue for $\omega_x \cdot c/U_\infty = -3$ and in red for $\omega_x \cdot c/U_\infty = +3$. It becomes clear that for the same iso-surface value, the CFD shows shorter surfaces suggesting the vorticity is diffused quicker in the CFD results than in real-life.

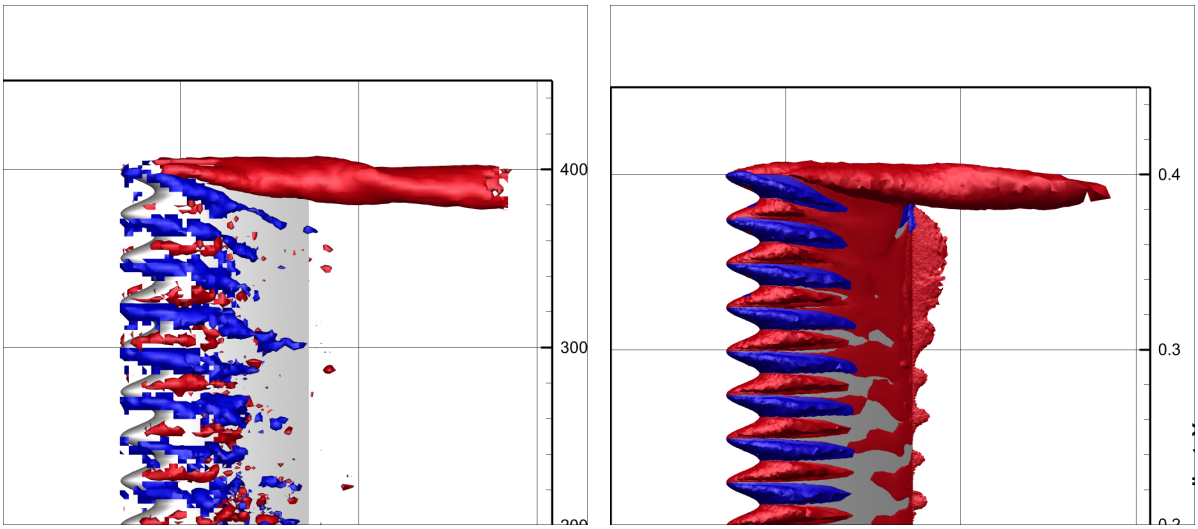

(a) $\alpha = 15°$ pitching up, experimental **(b)** $\alpha = 15°$ pitching up, CFD

Figure 4.8: Z-axis view of $\omega_x \cdot c/U_\infty = -3$ iso-surface in blue and $\omega_x \cdot c/U_\infty = +3$ iso-surface in red for the PeakTip wing at $k = 0.1$ and $\alpha = 15°$

The underpredicting of vorticity from CFD becomes even more clear when analysing a contour plot of the normalised streamwise vorticity on a transversal plane located at 1.5 chord lengths behind the quarter-chord line of the wing, as shown in Figure 4.9. The contour lines for the lowest value, $\omega_x \cdot c/U_\infty = 2$ show a similar diameter, which is why the iso-surfaces also look similar in diameter in Figure 4.8. But inside of that iso-surface, the peak values of vorticity seen in the experimental data are much higher.

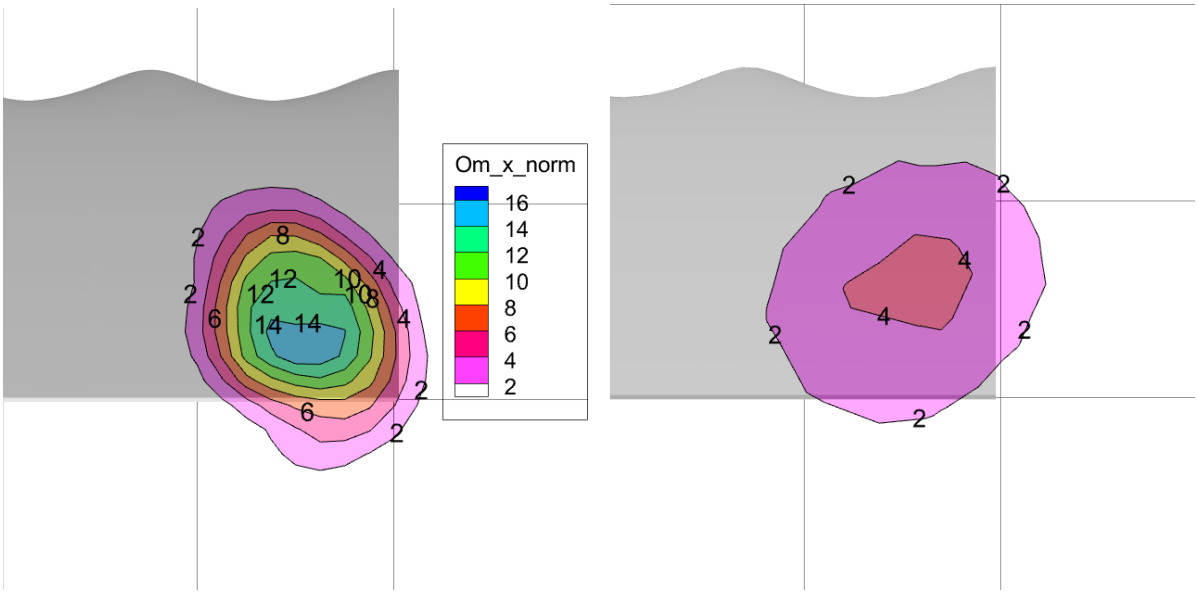

(a) $\alpha = 15°$ pitching up, experimental **(b)** $\alpha = 15°$ pitching up, CFD

Figure 4.9: Normalised streamwise vorticity contours focused on the tip vortex location - Exp vs. CFD

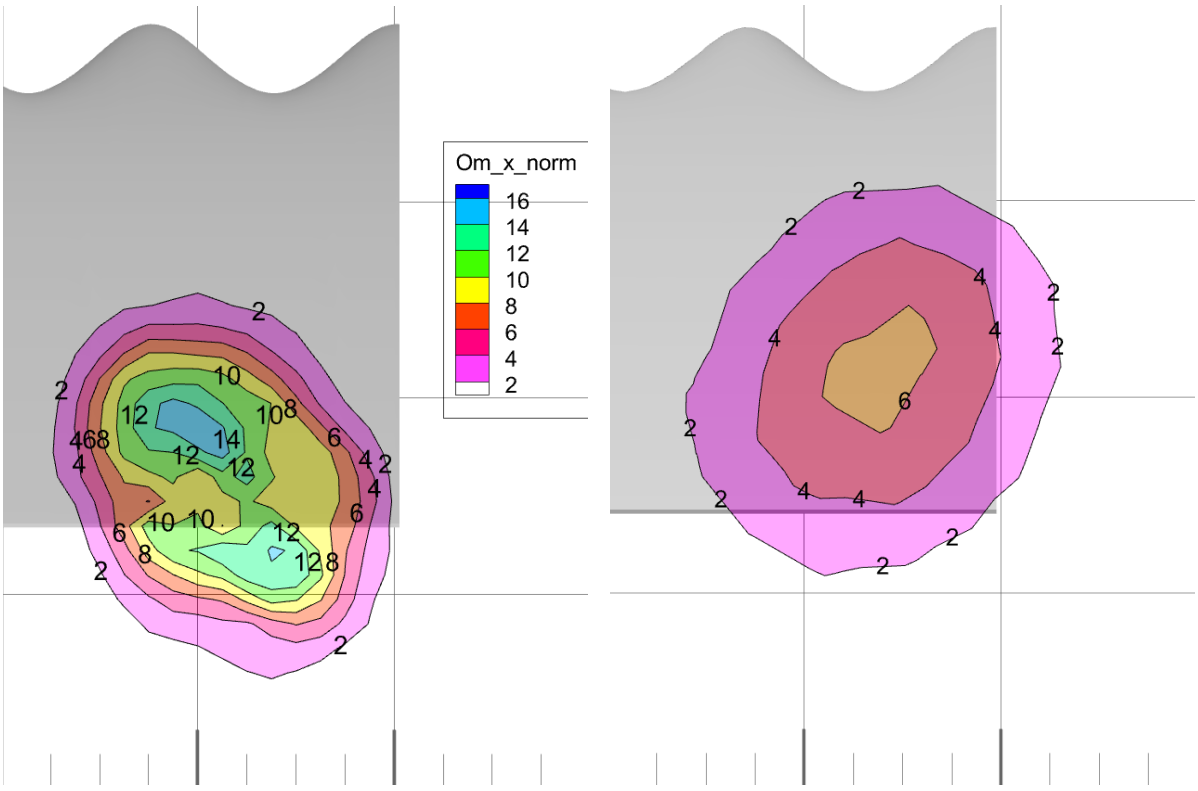

(a) $\alpha = 25°$ pitching up, experimental **(b)** $\alpha = 25°$ pitching up, CFD

Figure 4.10: Normalised streamwise vorticity contours focused on the tip vortex location - Exp vs. CFD

Plotting the tip vortex circulation over one cycle of the oscillation obtained from CFD data on top of the same graphs obtained from experimental data, produces the plot shown in Figure 4.11. A number of observations can be made on the comparison between graphs of circulation obtained from CFD and from experimental data:

- The linear increase portion of the CFD graph makes sense as a trend, but the value is approx 50% of that for the experimental results.

- CFD results do not characterise well the lift overshoot in the case of the of the SLE vs. tubercles. Even though the CFD flow field shows the DSV vorticity being more discretised and torn apart by the tubercles, and the SLE having a coherent DSV, this does not manifest in the expected lift overshoot (and hence circulation overshoot) of the SLE case.

- The hysteretical gap between the upstroke and the downstroke phases of the oscillation is significantly tighter in the CFD results than in the experimental results, again suggesting that the CFD simulations are not entirely capable of modelling accurately the dynamic effects.

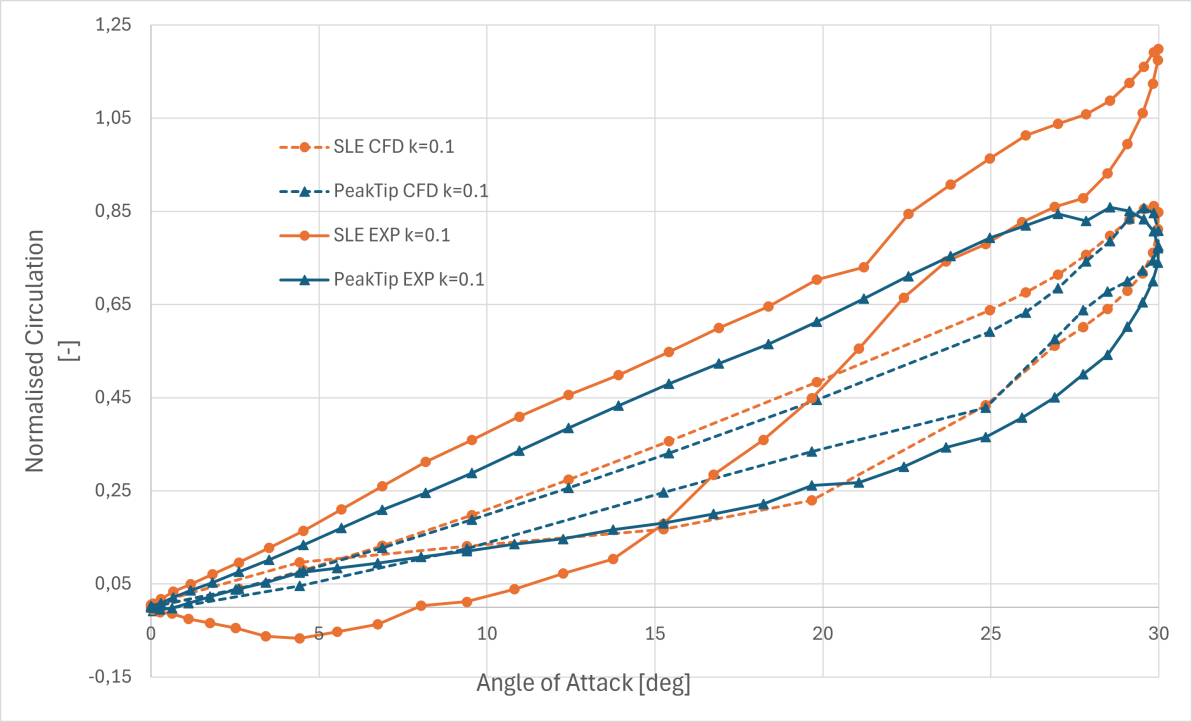

Figure 4.11: Normalised tip vortex circulation comparison between experimental results and CFD results measured at $x/c = 1.5$

Interestingly enough, the simulations were run also for a higher reduced frequency $k = 0.2$ only for the PeakTip tubercle wing and the normalised circulation (not compensated for phase-lag) shows a better correlation with that obtained from experimental results, as visible in Figure 4.12. As a general statement, the hysteretical gap between upstroke and downstroke is smaller thanks to the higher oscillation frequency which means the flow has less time to respond.

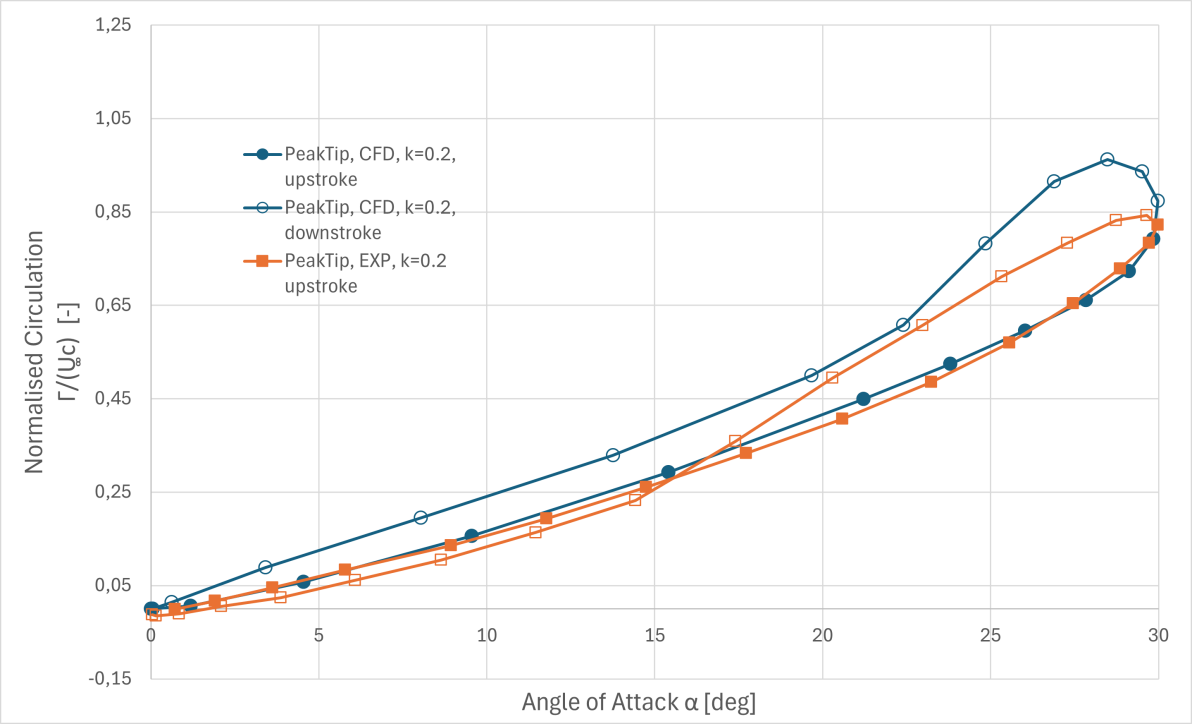

Figure 4.12: Normalised tip vortex circulation comparison between experimental results and CFD results (not compensated for phase-lag)

5

Results and Discussion

5.1. Experimental full flow field characterisation

The ground truth of this study is considered to be represented by the experimental results. As was shown in Section 4.1, the validity of the experimental method has been proven. The present section will delve into more detail into the evolution of the flow field over an oscillation cycle. The main tools for understanding the flow structure are iso-surfaces, as follows:

- Negative normalised x-vorticity (streamwise): $\omega_x \cdot c/U_\infty < 0$ in blue
- Positive normalised x-vorticity (streamwise): $\omega_x \cdot c/U_\infty > 0$ in red
- Positive normalised y-vorticity (spanwise): $\omega_y \cdot c/U_\infty > 0$ in pink
- Separated flow regions: iso-surface of $U = 0m/s$ in green

This colour convention will be maintained for both experimental and CFD results regardless of wing or flow conditions.
First, Figure 5.1 and Figure 5.2 show the 3D flow-field sampled from phase-averaged experimental data at four important points during the oscillation cycle:

- $\alpha = 15°$ pitching up, which falls in the linear monotonous lift increase regime
- $\alpha = 25°$ pitching up, which is close to the maximum lift value for all wings as will be shown later in Subsection 5.4.1
- $\alpha = 25°$ pitching down, which shows the initial downstroke regime and the flow's tendency to re-attach (or not)
- $\alpha = 15°$ pitching down, which falls in the monotonous lift decrease regime and exhibits clear flow re-attachment.

Starting off with Figure 5.1, the SLE baseline wing exhibits a clear, coherent, tip vortex at all angles of attack. With the exception of the tip vortex, vorticity is only produced at the boundary of the separated region. To illustrate the flow field over a wing with tubercles, the PeakTip wing is used in this comparison. The tubercle wing also shows a clear and coherent tip vortex, but weaker than the SLE vortex, visible by the smaller diameter of the iso-surface of the same normalised vorticity value. Furthermore, the tubercle wing results show clearly the existence of the counter-rotating vortex pairs shed by the angled edges of the tubercles. All the streamwise vortices are drawn inboard, towards the wing's root by the low static pressure area of the separated flow.

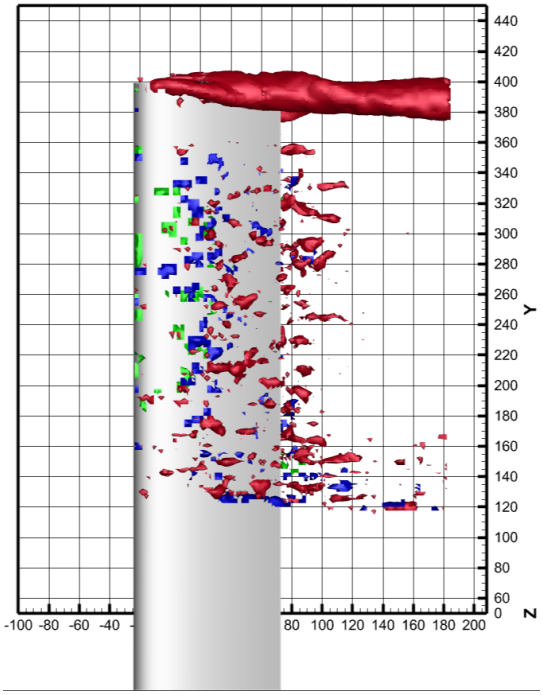

(a) SLE $\alpha = 15°$ pitching up

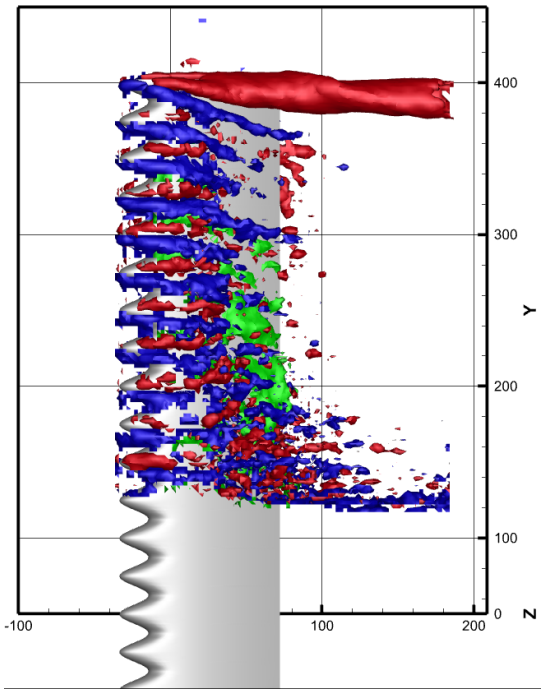

(b) PeakTip $\alpha = 15°$ pitching up

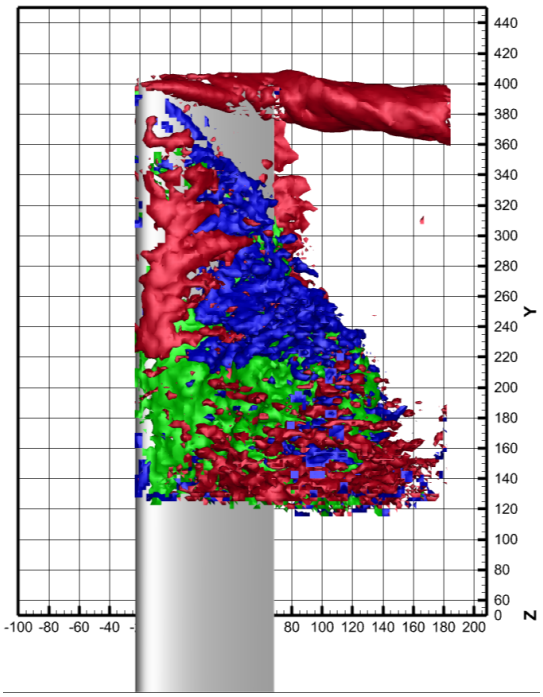

(c) SLE $\alpha = 25°$ pitching up

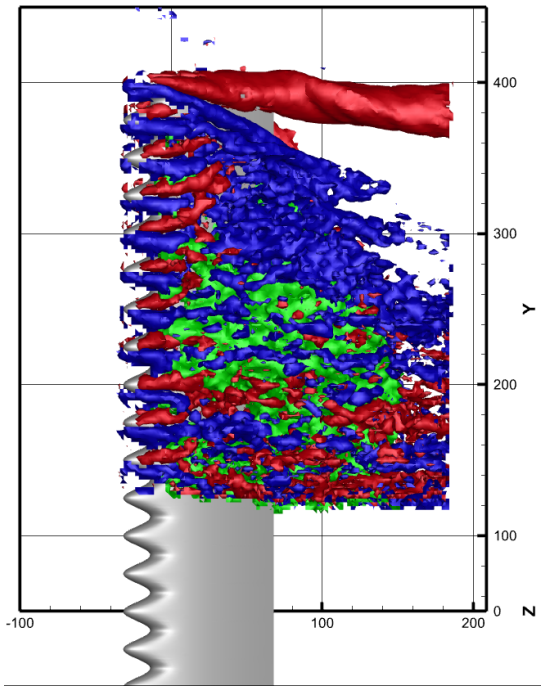

(d) PeakTip $\alpha = 25°$ pitching up

Figure 5.1: Z-axis view of $\omega_x \cdot c/U_\infty = -4.8$ iso-surface (blue) and $\omega_x \cdot c/U_\infty = +4.8$ iso-surface (red) for phase-averaged $k = 0.1$ experimental data, upstroke

The downstroke phase of the oscillation cycle is shown in Figure 5.2. The tip vortex of the SLE wing is somewhat violently sheared from the tip in the initial part of the downstroke, while the tip vortex appears a lot more stable in the PeakTip case. The PeakTip wing shows a re-stabilisation of the flow following the maximum amplitude with the tubercle streamwise vortices re-aligning with the flow

and compartmentalising the separation regions, concentrating them at the tubercle trough locations, whereas the separation region continues to stretch over almost the entire span in the SLE case, even down to angles of $\alpha = 15°$ where the tubercle wing's flow has almost entirely re-attached.

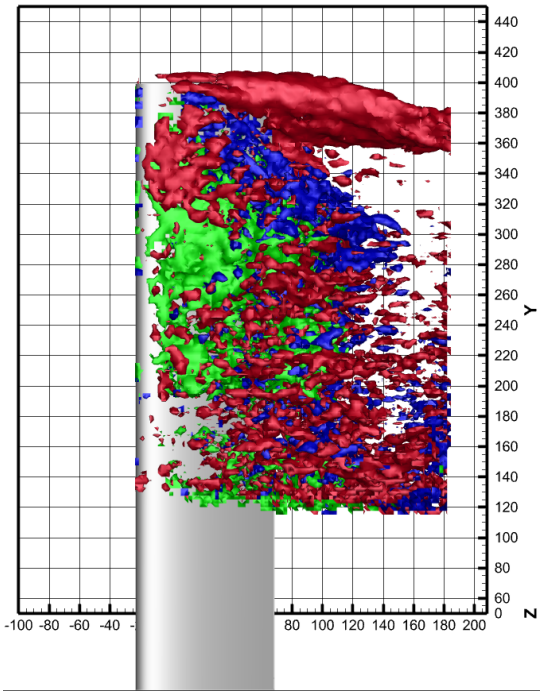

(a) SLE $\alpha = 25°$ pitching down

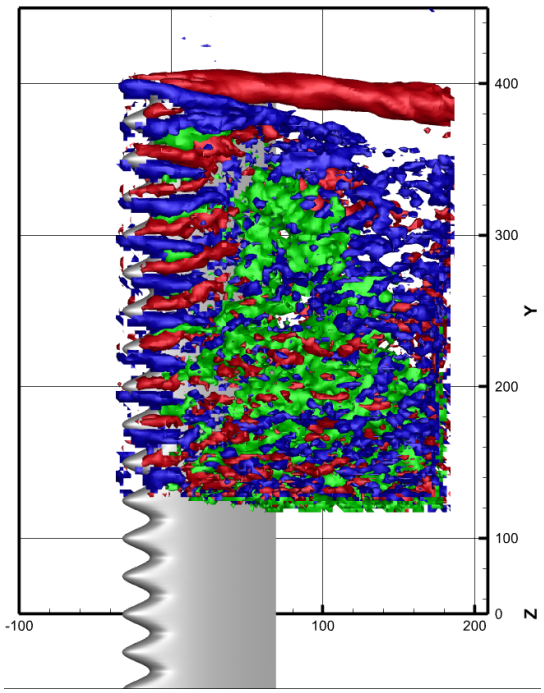

(b) PeakTip $\alpha = 25°$ pitching down

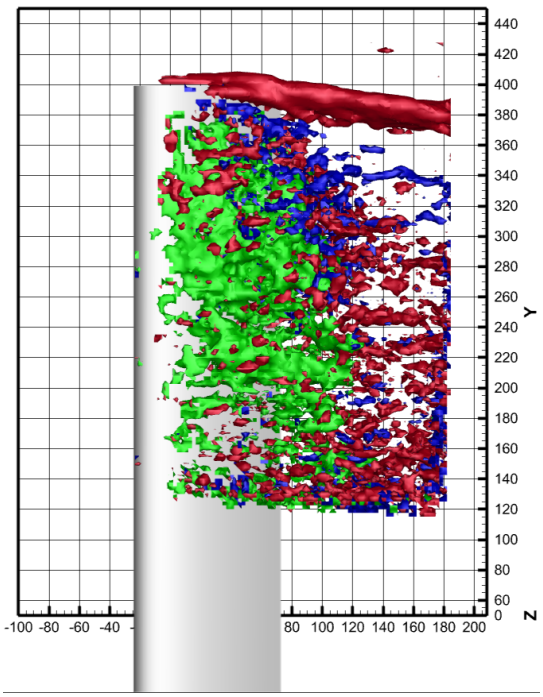

(c) SLE $\alpha = 15°$ pitching down

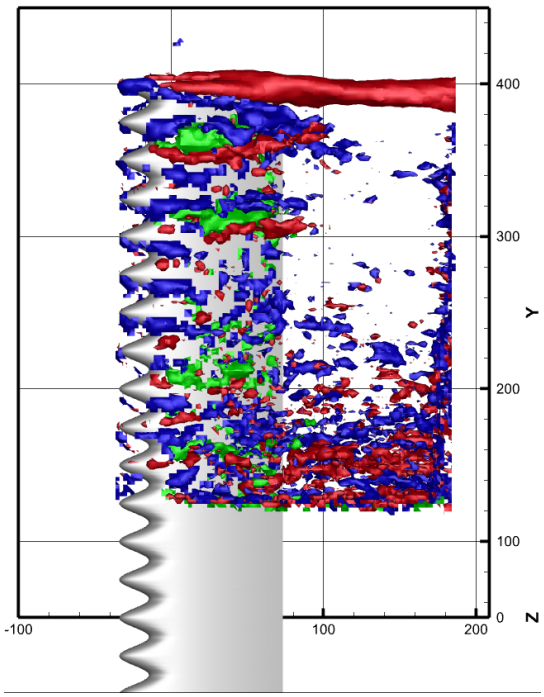

(d) PeakTip $\alpha = 15°$ pitching down

Figure 5.2: Z-axis view of $\omega_x \cdot c/U_\infty = -4.8$ iso-surface (blue) and $\omega_x \cdot c/U_\infty = +4.8$ iso-surface (red) for phase-averaged $k = 0.1$ experimental data, downstroke

The evolution of the separated flow region is worth having a more detailed look at. The upstroke phase comparison is shown in Figure 5.3. In the SLE case, the iso-surface of axial velocity zero shows a fairly consistent spanwise development, spreading and forming a big separation region. The flow over the near-tip region of the SLE wing stays permanently attached up to the highest angles of attack thanks to the induced downwash from the tip vortex. The behaviour in the tubercle case is different to the one of the SLE wing in that the separation occurs first near the trailing edge region, aligned with the spawnwise locations of the troughs. This makes sense because these regions experience reduced axial velocity naturally near the trailing edge that is now also coupled with the induced upwash from the streamwise vortices. As the angle of attack increases, small stall cells form near the leading-edge of the trough location, bordered by the tubercle vortices. Near the maximum angle of attack the separated region has propagated spanwise over the wing, with the exception of the near-tip region that remains attached due to the strong downwash induced by the tip vortex.

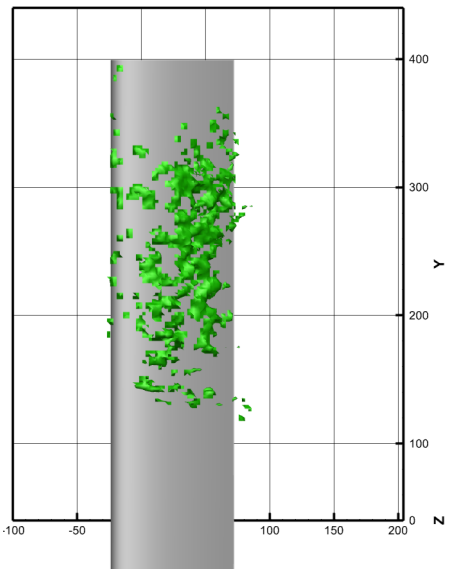

(a) SLE $\alpha = 15^\circ$ pitching up

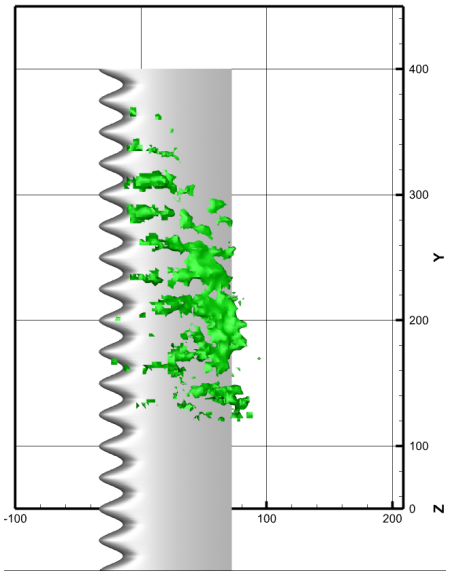

(b) PeakTip $\alpha = 15^\circ$ pitching up

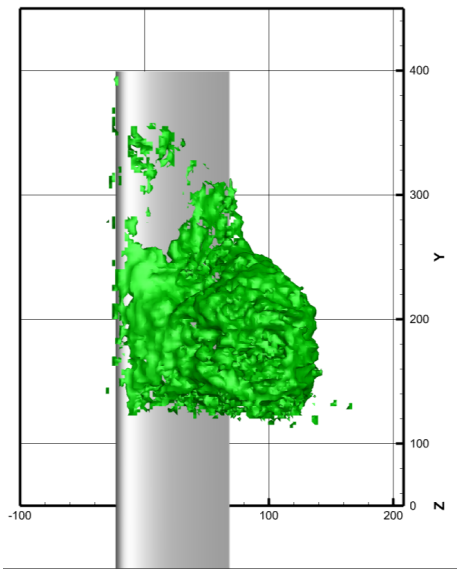

(c) SLE $\alpha = 25^\circ$ pitching up

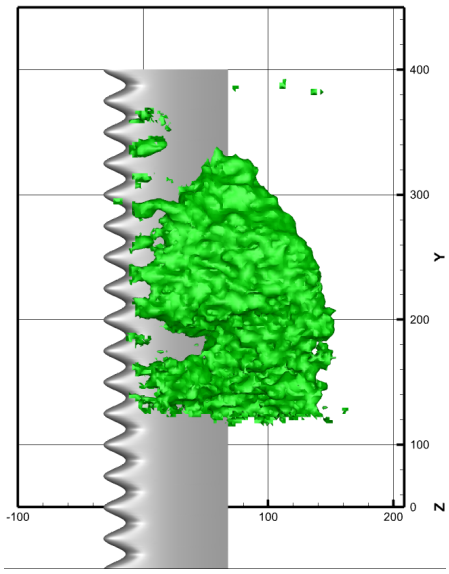

(d) PeakTip $\alpha = 25^\circ$ pitching up

Figure 5.3: Z-axis view of $U = 0m/s$ iso-surface (green) phase-averaged $k = 0.1$ experimental data, upstroke

One other significant difference to the SLE case is the behaviour on the downstroke, shown in Figure 5.4. In the tubercle wing's case, the flow re-attaches over certain parts of the wing already by the point of $\alpha = 25°$, again seeing the separated flow being split into stall cells that persist in the tubercle trough locations until very low angles of attack.

Another interesting aspect about the separated flow in the SLE case is that shown by Figure A.1, namely that separation bubbles are shed by the wing at two moments in the oscillation and in a fairly consistent manner considering these releases are clear in phase-averaged data. This occurs around $\alpha = 27°$ on the upstroke and around $\alpha = 29.5°$ on the downstroke.

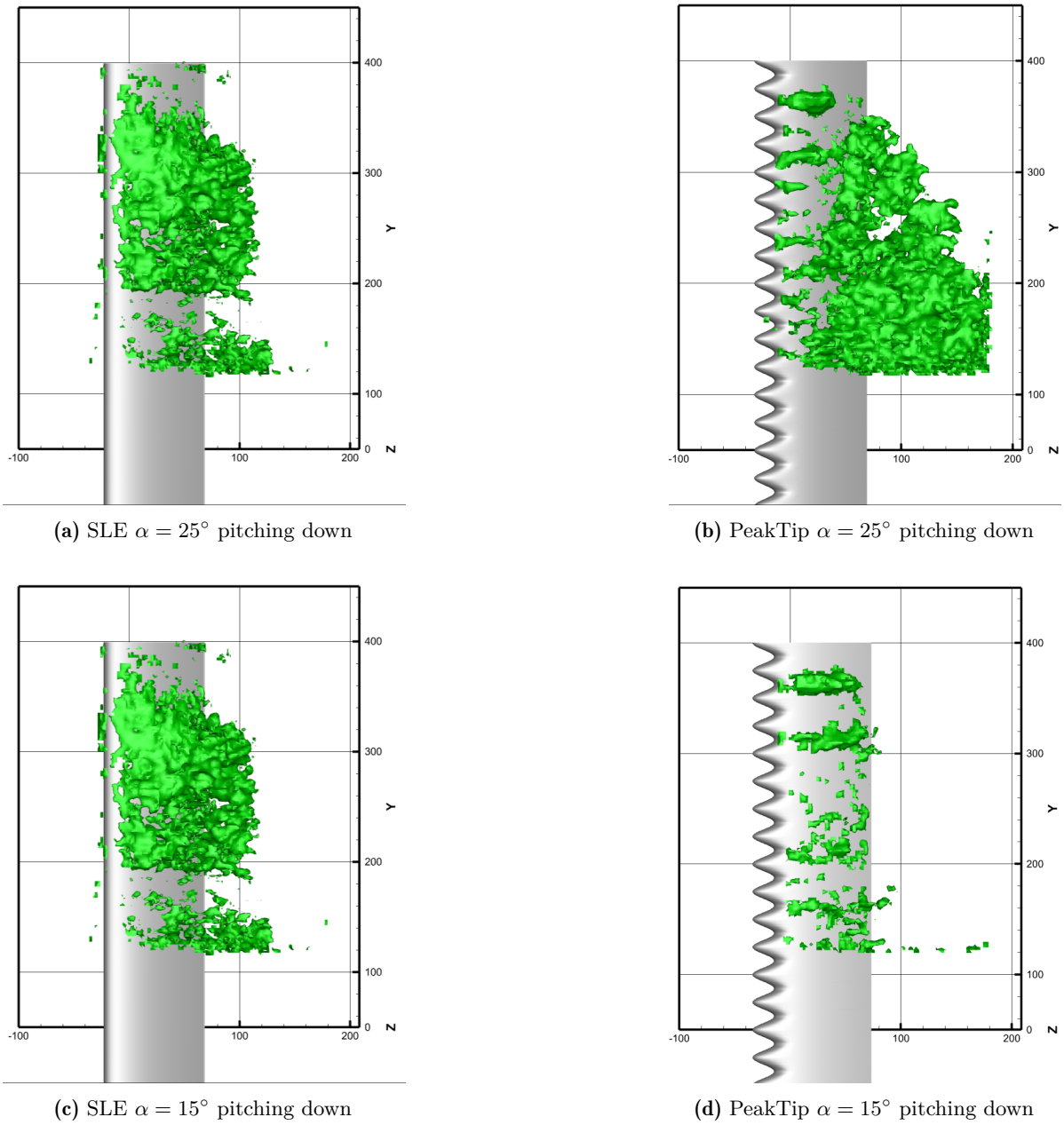

(a) SLE $\alpha = 25°$ pitching down

(b) PeakTip $\alpha = 25°$ pitching down

(c) SLE $\alpha = 15°$ pitching down

(d) PeakTip $\alpha = 15°$ pitching down

Figure 5.4: Z-axis view of $U = 0m/s$ iso-surface (green) phase-averaged $k = 0.1$ experimental data, downstroke

Another important aspect needs to be mentioned and that regards the formation and shedding of the DSV. The dynamic stall vortex (DSV) was introduced in Subsection 1.1.2 as being responsible for the characteristic lift overshoot followed by sharp drop in lift of straight leading-edge wings undergoing pitch oscillations. This is visible in Figure A.2 in the form of iso-surfaces of positive normalised spanwise vorticity. It is apparent that the SLE experimental results do show a coherent vortical structure forming from the leading-edge and being convected over the wing. The tubercle wings, on the other hand, break down this sheet of vorticity and do not allow for the formation of a coherent spanwise vortex. This is further reinforced by the data in Subsection 5.4.1 that show the SLE wing having an overshoot in the circulation (hence in the lift), while the tubercle wings do not exhibit such a behaviour.

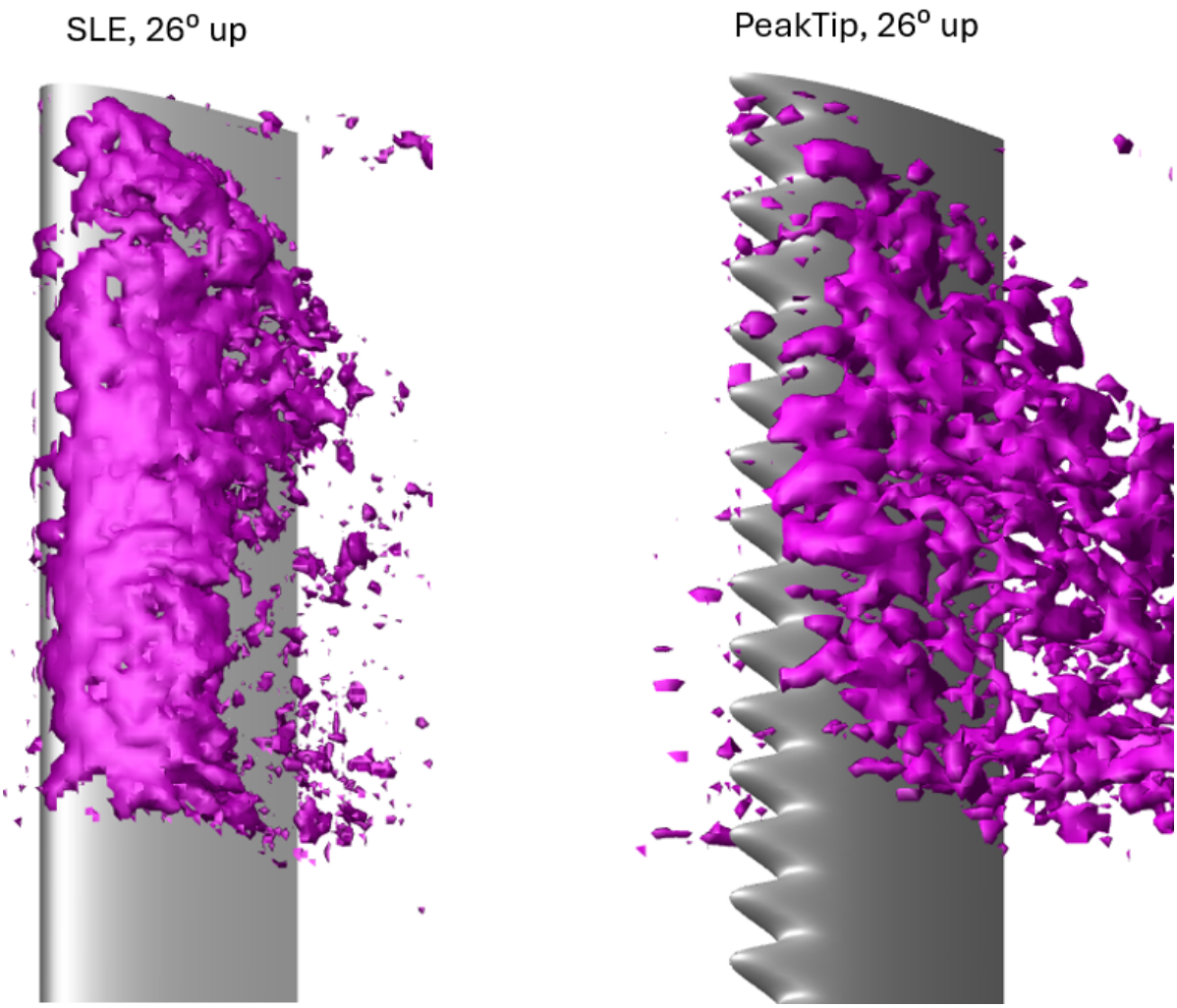

Figure 5.5: Slanted top view with the wing root at the bottom and the wing tip at the top of $\omega_y \cdot c/U_\infty = 6$ iso-surface for phase-averaged, $k = 0.1$ experimental data

5.2. CFD full flow field characterisation

The following subsection will present the same steps through the oscillation as Section 5.1, but as produced by the CFD analysis described in Section 3.3. The flow-field is shown in Figure 5.7. The main reason for the parallel CFD analysis has been, from the beginning, obtaining force data for the different wing models. Therefore, plotting the wing lift coefficient resulting from the CFD analysis produces the graph shown in Figure 5.6. A number of observations can be made and corroborated between the force graph and the flow-field.

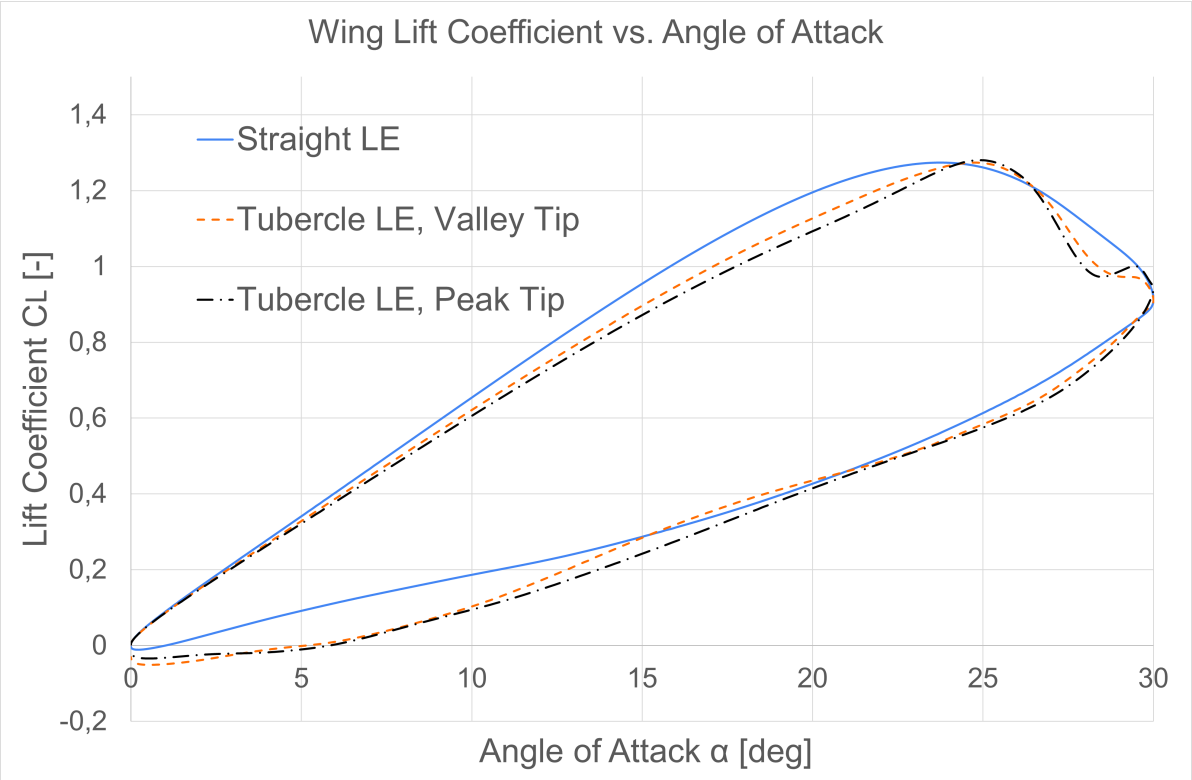

Figure 5.6: Lift curve over the oscillation cycle produced from CFD results

Starting with the upstroke phase of the oscillation:

- From $\alpha = 0°$ to around $\alpha = 20°$ the lift slopes align with theory: the lift slope is almost linear for both the straight and the tubercle wings and the lift is higher for the SLE at any angle of attack; In terms of flowfield, Figure 5.7a and Figure 5.7b show how both the SLE and the PeakTip wings exhibit a coherent tip vortex and separation regions that start from the trailing-edge due to the low Reynolds number, as explained in Subsection 4.2.2. In particular, the tubercle wing shows this separation occurring at the trailing-edge, but in the spanwise locations aligned with the tubercle troughs, same as the experimental results shown in Figure 5.3. Also aligning with experimental results is the pattern of alternating counter-rotating vortices shed by the tubercles.

- From $\alpha = 20°$ to around $\alpha = 25°$ is the region where the wings generate their maximum lift under this dynamic pitching. The $C_{L_{max}}$ occurs at an angle of attack higher by approximately 1° in the case of the tubercle wings compared to the straight wing, which would align with expectations on the delay of stall by the tubercles and from the literature. However, the $C_{L_{max}}$ value itself is almost identical for both straight wing and tubercle wings, which is not expected. According to both literature and to the flow field snapshots shown previously that suggest the DSV is less powerful and coherent in the tubercle case, the straight wing was expected to exhibit a higher $C_{L_{max}}$, due to the dynamic lift overshoot. More detail into the differences between CFD and experimental results that suggest the maximum lift prediction from CFD is underpredicted in the SLE case is shown in Section 4.3. The flowfield structure, however, correlates well with that

from experimental results: Figure 5.7c shows how the separation regions propagates towards the leading-edge and almost covers the entire span with the exception of the tip region, in the SLE case. Figure 5.7d shows how the separation region also propagates further forward in the tubercle case, linking with the tubercle trough locations on the leading edge, forming an incipient form of stall cells, delimited by the streamwise vortices.

- From $\alpha = 25°$ to the maximum angle $\alpha = 30°$ the wings are in the deep stall regime. While the wing continues to pitch up past the α_{max}, the tubercle wings exhibit a somewhat unexpected behaviour of an initial quite sudden drop in lift, followed by the reattachment of the flow generating a second, smaller peak in lift around $\alpha = 29°$. All of this, while the SLE wing losses lift monotonously and with a shallower slope.

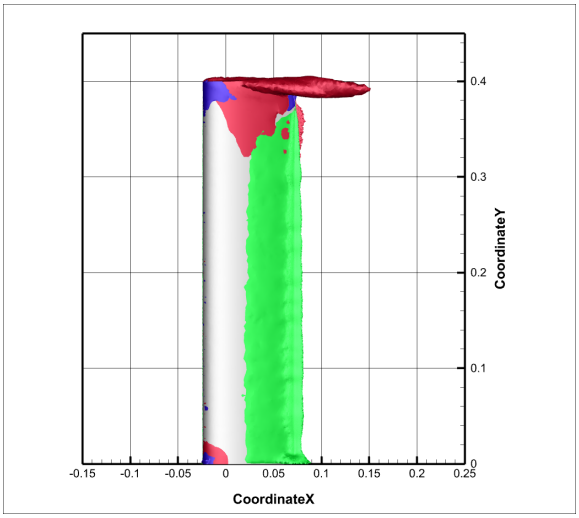

(a) SLE $\alpha = 15°$ pitching up

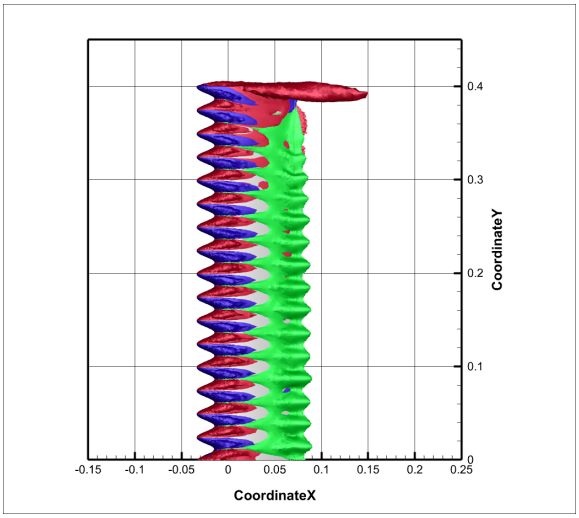

(b) PeakTip $\alpha = 15°$ pitching up

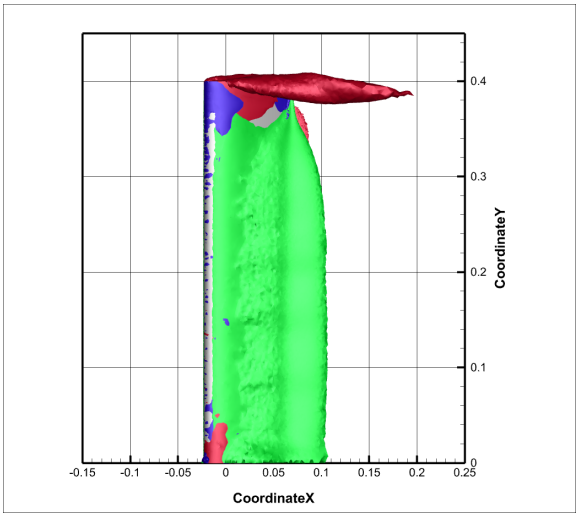

(c) SLE $\alpha = 25°$ pitching up

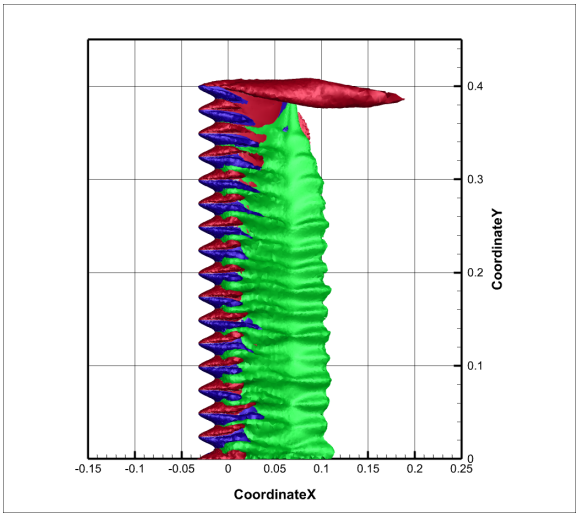

(d) PeakTip $\alpha = 25°$ pitching up

Figure 5.7: Z-axis view of $\omega_x \cdot c/U_\infty = -4.8$ iso-surface (blue) and $\omega_x \cdot c/U_\infty = +4.8$ iso-surface (red) and $U = 0m/s$ iso-surface (green) for $k = 0.1$ CFD data

A number of interesting observations can also be made about the downstroke phase of the oscillation cycle:

- From the maximum angle $\alpha = 30°$ down to $\alpha = 25°$, the force graph suggests the SLE wing losses lift at a slower rate than the tubercle wing and that is most likely thanks to the separated

flow bubble being detached and shed by the wing after reaching its maximum pitching amplitude. However, the flow-field pictures at $\alpha = 25°$ show very different phenomena between the two wings: the SLE wing appears to still be very much separated, starting from very close to the leading edge, as shown by Figure 5.8a. The tubercle wing shows the flow re-attaching close to the leading-edge thanks to the streamwise vortices that appear to carve the separation region into coherent stall cells located at the trough locations. This is very well aligned with the flow-field structure shown by experimental results at the same angle of attack.

- From $\alpha = 25°$ down to $\alpha = 0°$ the lift is returning more or less linearly to zero for both the SLE and tubercle wings with no great differences between them. This again, suggests that the force graph should be used cautiously as the flow-field is suggesting a different evolution of the flow. Namely, by $\alpha = 15°$, Figure 5.8c is showing an SLE wing where the flow has re-attached everywhere except a strip around the quarter-chord which is very different from the experimental result from Figure 5.4 that still shows an almost fully separated SLE wing by this point. The tubercle wing's flow structure correlates better with the experimental results, showing the compartmentalisation of the separated region into stall cells very clearly. Their size is also aligned with that from previous steady-state studies such as Cai et al. [23].

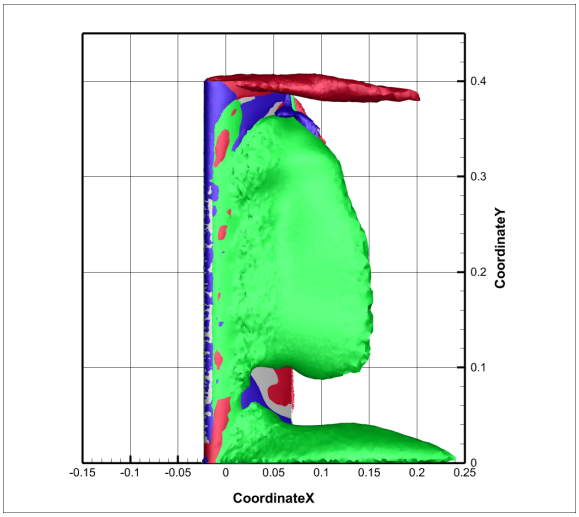

(a) SLE $\alpha = 25°$ pitching down

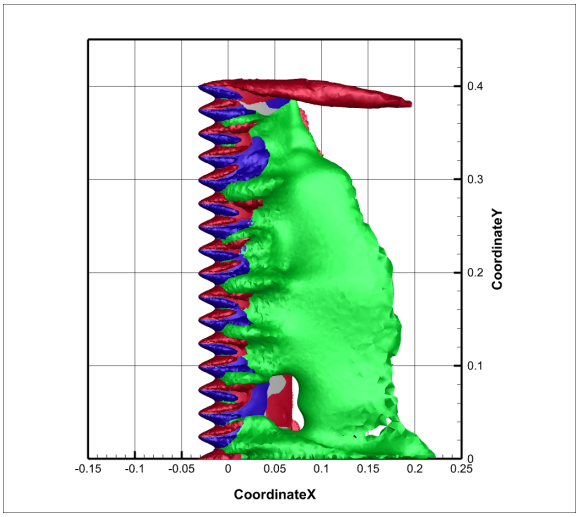

(b) PeakTip $\alpha = 25°$ pitching down

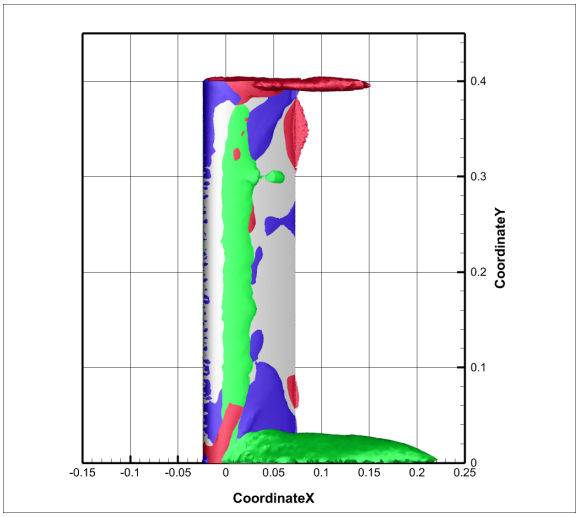

(c) SLE $\alpha = 15°$ pitching down

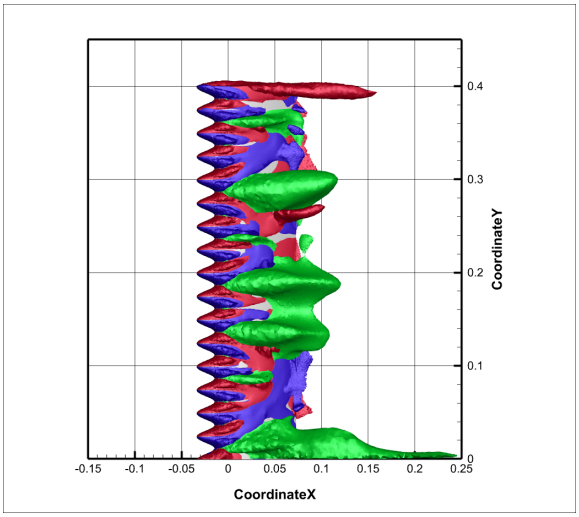

(d) PeakTip $\alpha = 15°$ pitching down

Figure 5.8: Z-axis view of $\omega_x \cdot c/U_\infty = -4.8$ iso-surface (blue) and $\omega_x \cdot c/U_\infty = +4.8$ iso-surface (red) and $U = 0m/s$ iso-surface (green) for $k = 0.1$ CFD data

5.3. Effect of tubercles under higher reduced frequency

One of the aspects that was intended to be studied is whether a higher reduced frequency (i.e. $k = 0.2$) and highly unsteady flow conditions would affect the effect the leading-edge tubercles have on the flow-field. To that end, CFD simulations were carried out at $k = 0.2$ only for the SLE and PeakTip wings.

The dynamic lift curves produced from CFD simulation results is shown in Figure 5.9, overlapped with those shown previously in Figure 5.6 for the lower $k = 0.1$. It is clear looking at these results that the lift produced by both the straight and the tubercle wings is higher with the higher frequency, thanks to a stronger DSV. Furthermore, because of the higher oscillation frequency, the lift curve keeps increasing almost linearly all the way up to the maximum oscillation angle of attack, as the flow field has less time to react to the angle change. This means that the so-called "deep stall" region where the wing is still pitched up past its stall point is not visible on the new lift coefficient graphs, as opposed to the lift decrease region in the $k = 0.1$ data between $\alpha = 25°$ and the maximum angle $\alpha = 30°$.

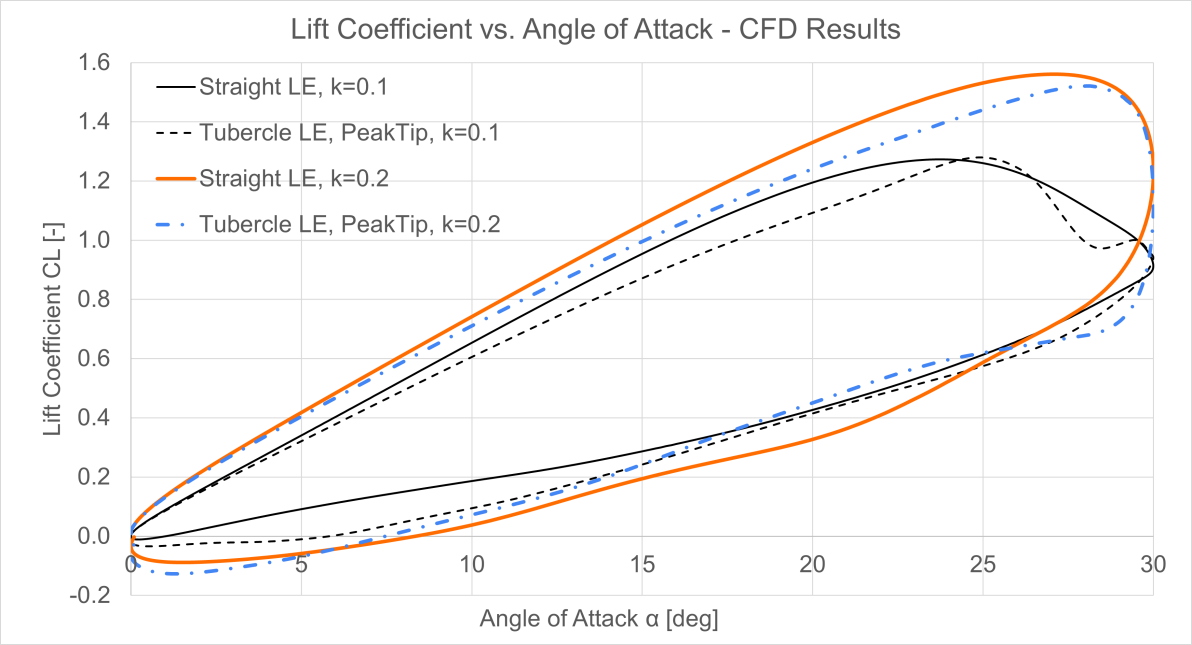

Figure 5.9: Lift curve over the oscillation cycle produced from CFD results for reduced frequencies of $k = 0.1$ and $k = 0.2$

The flow-field evolution in this faster pitching case is very similar to the $k = 0.1$ case for both the tubercle wing and the SLE wing, as can be observed from the snapshots picked in Figure 5.10. The flow separation propagates from the trailing-edge toward the leading-edge as the wing pitches up. More significant phenomena occur on the downstroke phase of the oscillation. The lift curves of both wings show a stepped behaviour in the graph, corresponding to moments when the separation bubbles are violently detached and shed from the wing. The flow mechanism of compartmentalisation that splits the separation region into stall cells using the tubercle-shed streamwise vortices is perhaps even more visible in this faster pitching scenario. The lift curve also shows a bigger reduction in the hysteretical gap brought by the leading-edge tubercles at the higher reduced frequency, than at the lower one.

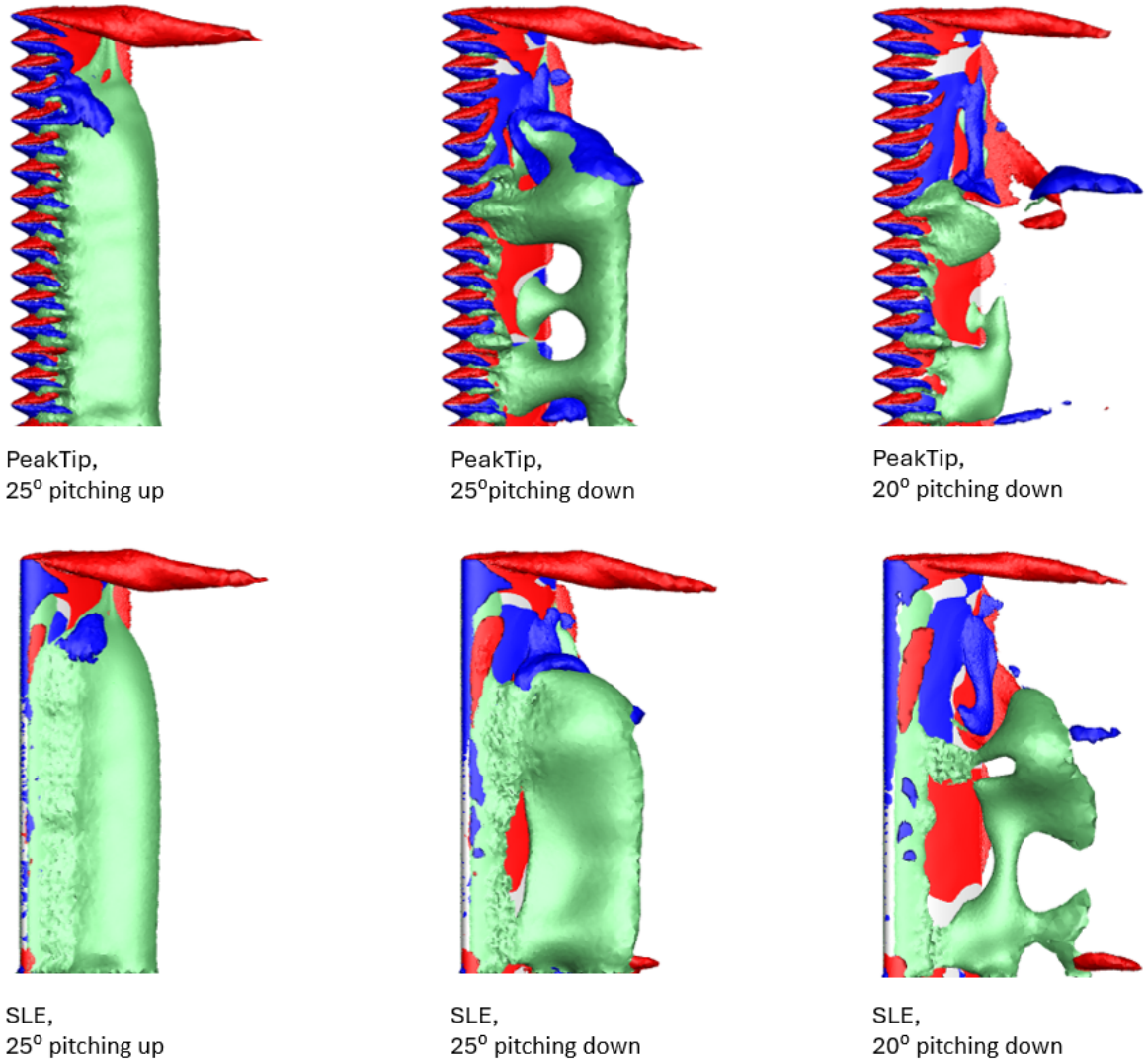

Figure 5.10: Z-axis view of $\omega_x \cdot c/U_\infty = -4.8$ iso-surface (blue) and $\omega_x \cdot c/U_\infty = +4.8$ iso-surface (red) and $U = 0m/s$ iso-surface (green) for $k = 0.2$ CFD data

The bigger maximum lift difference between the SLE and PeakTip wings seen at this higher reduced frequency is most likely due to the bigger difference in how the DSV is shed and convected over the wing. The flow-field snapshots produced from CFD in Figure 5.11 provide an interesting look. It is clear that for the same values of the spanwise vorticity iso-surface, the DSV is weaker and forms later in the case of the tubercle leading-edge wing than in that of the SLE wing.

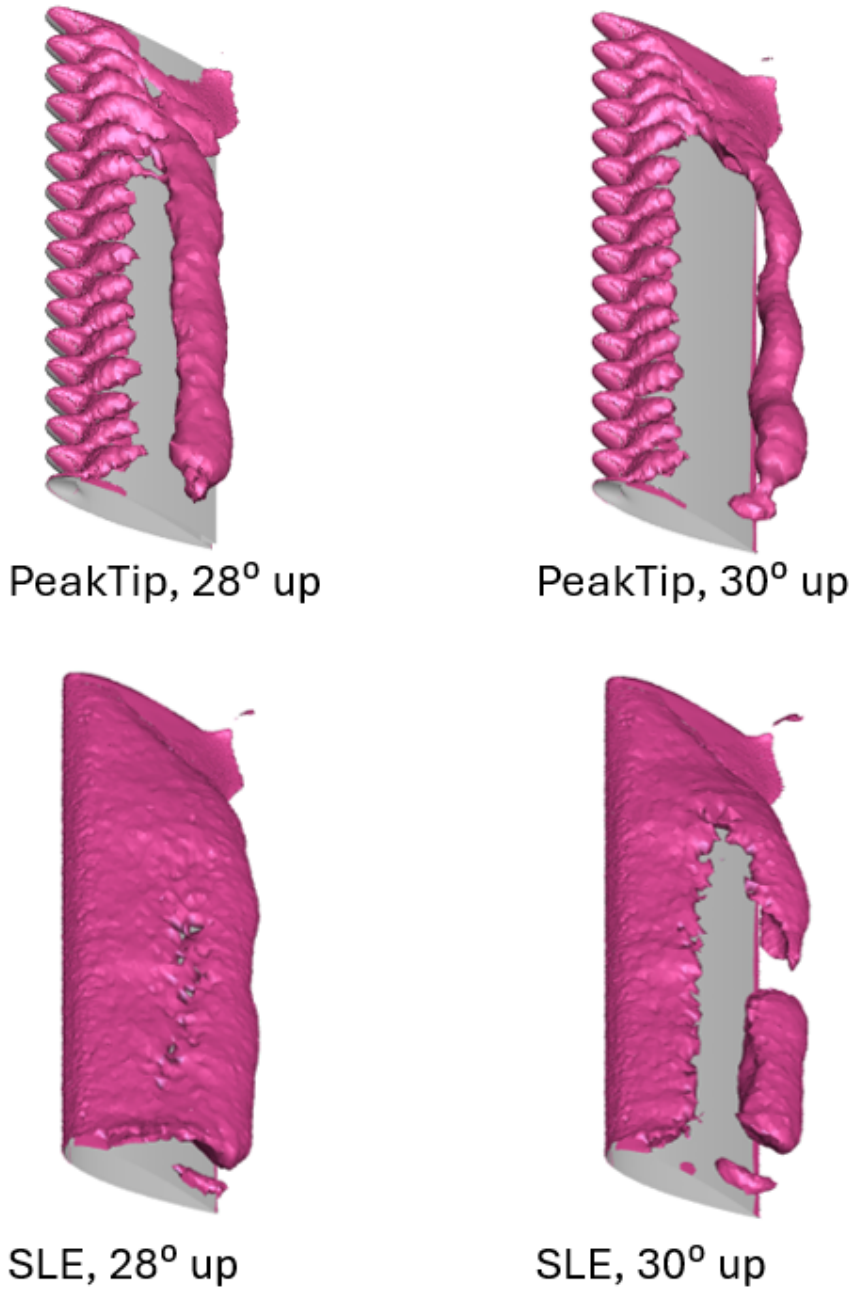

Figure 5.11: Slanted top view with the wing root at the bottom and the wing tip at the top of $\omega_y \cdot c/U_\infty = 6$ iso-surface for $k = 0.2$ experimental data

5.4. Effect of tubercles on the tip vortex

5.4.1. Effect of LE tubercles on the tip vortex circulation

A good way of evaluating the evolution of the tip vortex throughout the oscillation cycle is by plotting the evolution of its circulation. This is computed by using the same method for integrating the x-axis vorticity ω_x over a virtual disc surface placed transversally to the flow downstream of the wing that encompasses the tip vortex. Performing this integration for every time step of the phase-averaged experimental data for the SLE, PeakTip and ValTip wings produces the graph shown in Figure 5.12. It is important to note that the point in the SLE graph corresponding to an angle of 22 degrees and the point in the PeakTip graph corresponding to an angle of 25 degrees are considered to be outliers due to imperfections in the data that even when phase-averaged is still not perfectly dense. The ValTip graph showing no such outliers suggests this is also what the PeakTip graph should look like without the outlier point.

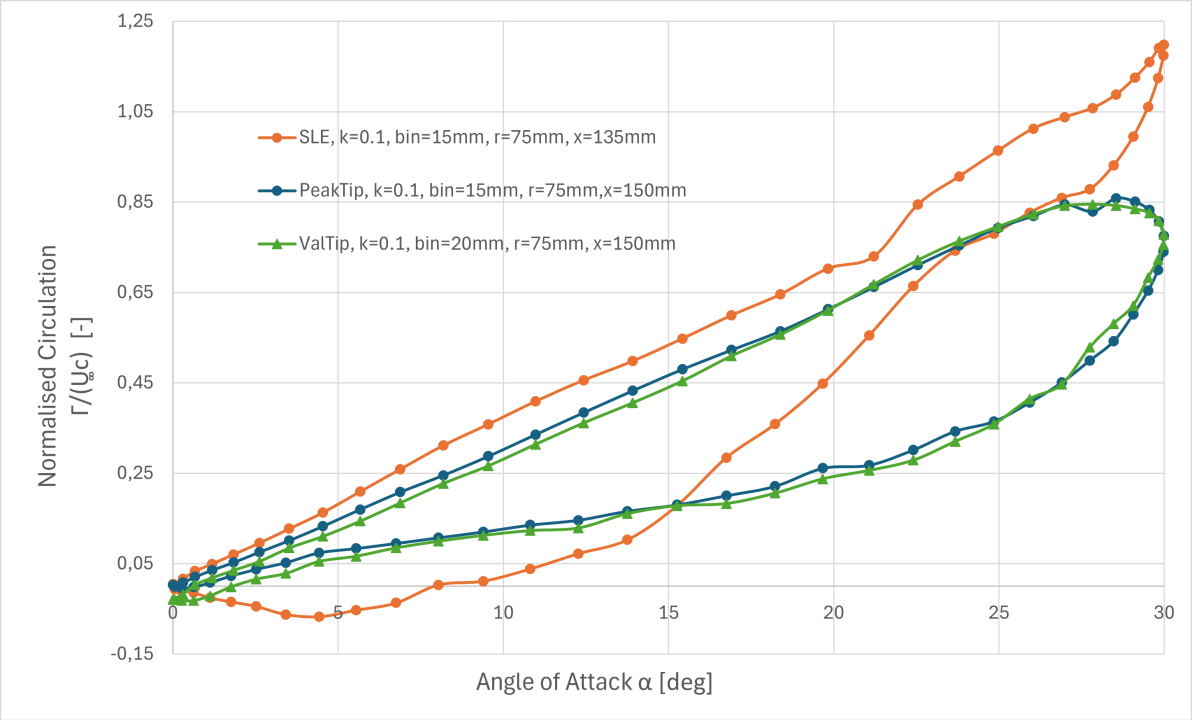

Figure 5.12: Normalised circulation comparison obtained from phase-averaged experimental data

Interpreting the graphs in Figure 5.12, the following observations can be drawn:

- The SLE graph was presented and validated with literature results also in Section 4.1. It exhibits an almost linear increase portion on the oscillation upstroke, followed by a sharp increase up to the maximum oscillation amplitude caused by the dynamic lift overshoot that is well-documented for the straight leading-edge pitching wings (Subsection 1.1.2);

- The downstroke phase starts with a sharp drop followed by a hysteretical return to 0 that appears to be done in steps. This could be attributed to the shedding/release of the separation bubbles shown in Figure A.1;

- The tubercle wings both follow a very similar path, again with an almost linear increase of circulation on the upstroke portion of the oscillation. The drop of circulation after the maximum point is a lot shallower and more benign which agrees with the known effects of tubercles on lift even from the steady studies conducted before. This is attributed to the braking up of the DSV by the leading-edge tubercles which discourage the formation of a strong coherent vortex. This is visualized in Figure 5.14 as iso-surfaces of spanwise vorticity.

- The hysteretical gap between upstroke and downstroke is smaller in the case of the tubercle wing, that also exhibit a very linear and progressive re-attachment.

The pressure difference between the suction side and the pressure side of the wing creates a spanwise pressure gradient, causing air to flow around the wingtip and form vortices at the tips [9]. The tip vorticity (and, when integrated, the circulation) is proportional to the lift force produced by the wing and can therefore offer an insight into the evolution of the lift force for the experimental case where force balance measurements were not possible. In order to infer information about the lift from the tip circulation data, a phase-lag compensations needs to be applied. It takes the vortex information time to convect downstream from the formation region to the measurement region. The measurements for the data in Figure 5.12 are taken over a disc positioned at $x = 150mm$ or 1.5 chord-lengths behind the quarter-chord line of the wing. The aerodynamic force and the tip vortex are assumed to be generated at the quarter-chord location. To estimate the velocity at which the vortex is convected downstream, Chang and Park [28] use the mean axial velocity in the tip vortex region at 0.5 chord-lengths behind the trailing edge. Birch and Lee [29] have a simpler approach, assuming that the vortex convection velocity is equal to the freestream velocity. Furthermore, Birch and Lee [29] show that the difference between the two methods is negligible. Therefore, the current results wer also obtained by assuming the vortex is convected downstream with the freestream velocity of $U_\infty = 5m/s$. This translates into a time delay of $\delta_t = 0.03s$ for a change in force to register as a change in circulation at the measurement plane. Shifting the circulation values by this time delay backwards in time, to better reflect the situation at the wing, produces the graph shown in Figure 5.13.

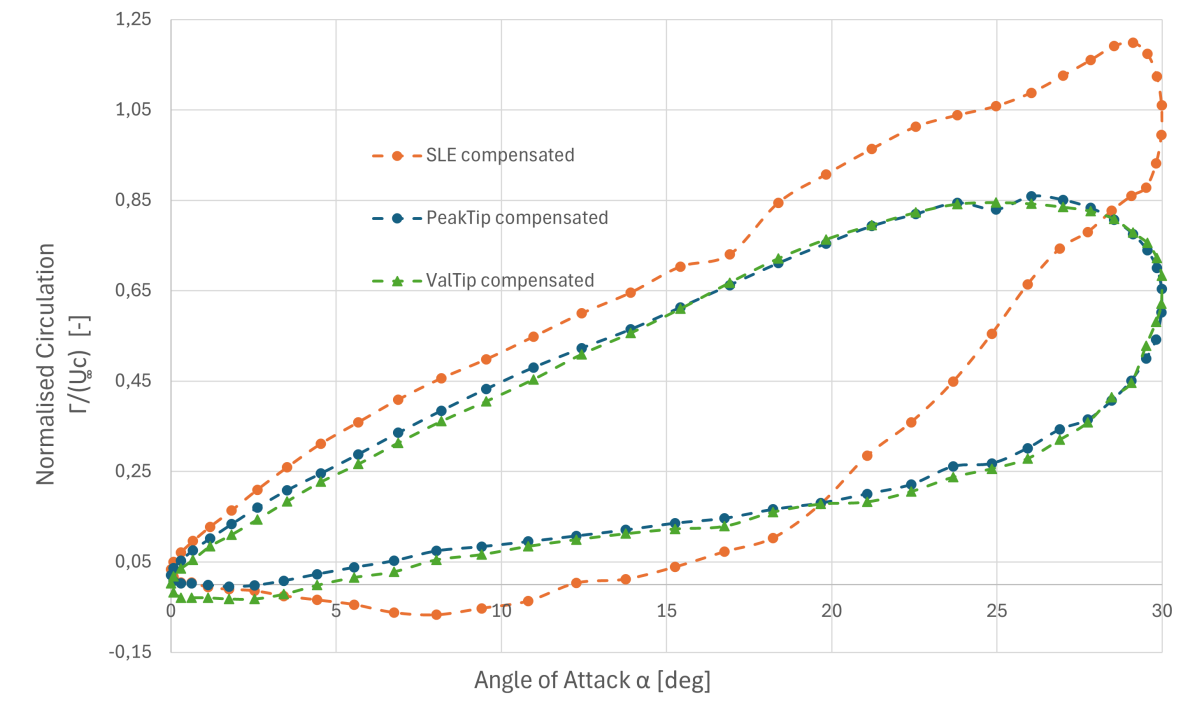

Figure 5.13: Normalised circulation comparison obtained from phase-averaged experimental data, compensated for time delay

While the time-compensated graph in Figure 5.13 does not exhibit any different trends to the one in Figure 5.12, it gives a better idea of the angle of attack corresponding to the maximum lift produced by these wings. Perhaps contrary to the expectations formed from literature on the lift curve in static conditions (as detailed in Subsection 2.4.1), the SLE wing produces its maximum lift at a higher angle of approximately $\alpha_{max} = 29°$ than the tubercle wings which produce it at lower $\alpha_{max} = 25 - 26°$. However, this agrees with the general trend shown in the dynamic, pitch oscillation results of Borg [17], shown in Figure 2.11.

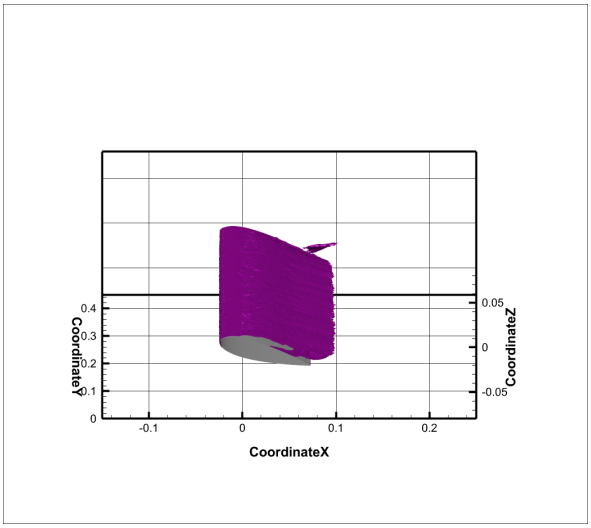

(a) $\alpha = 15°$ pitching up

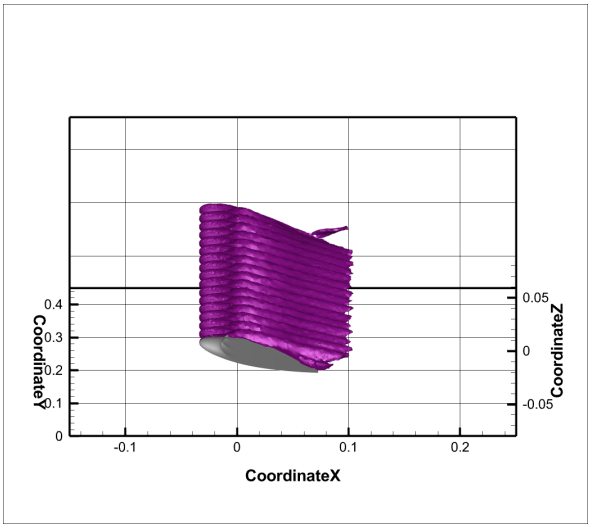

(b) $\alpha = 15°$ pitching up

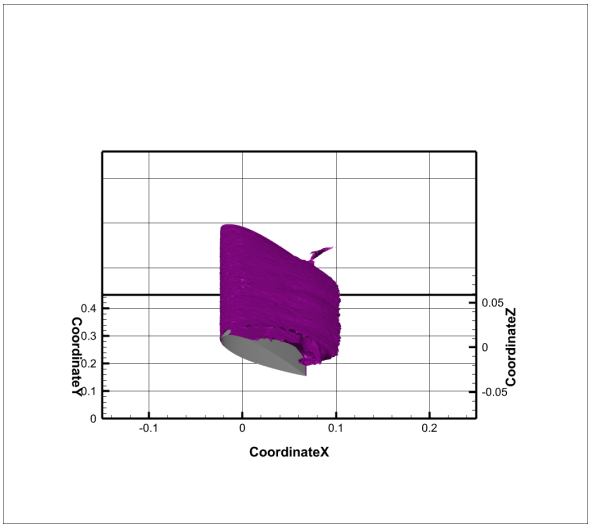

(c) $\alpha = 25°$ pitching up

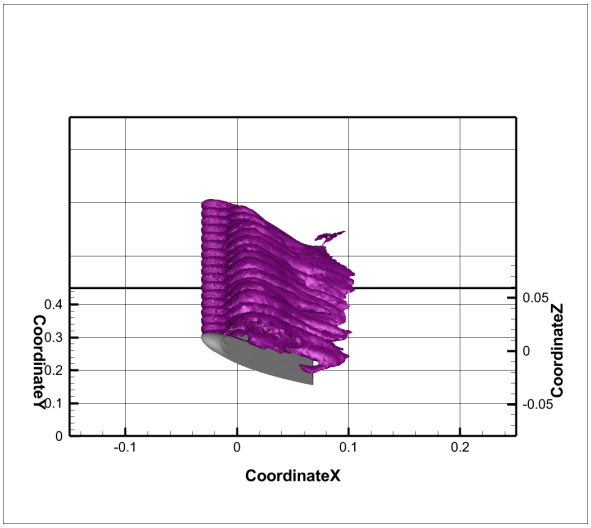

(d) $\alpha = 25°$ pitching up

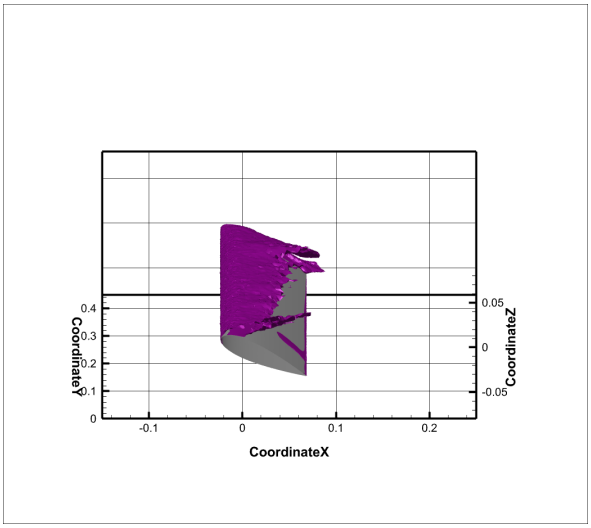

(e) $\alpha = 25°$ pitching down

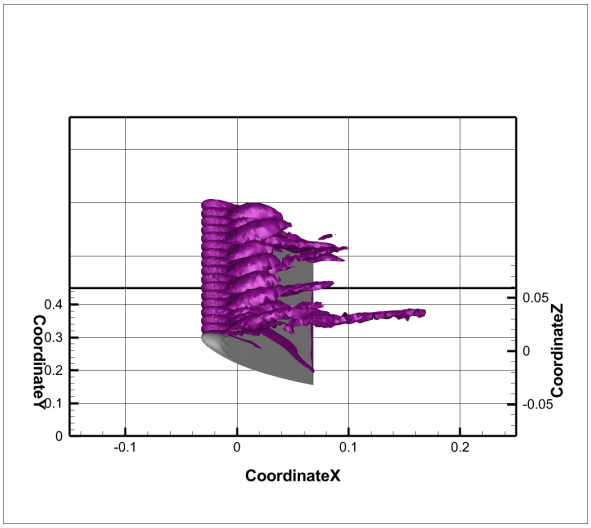

(f) $\alpha = 25°$ pitching down

Figure 5.14: Side view from the wing root of $\omega_y \cdot c/U_\infty = 6$ iso-surface for $k = 0.1$ CFD data

5.4.2. Influence of tip end condition on the flow in the tip region

Both the non-compensated and the time-compensated graphs of tip vortex circulation show there is a small, but fairly constant throughout the oscillation between the average tip vortex circulation of the PeakTip wing and that of the ValTip wing. The PeakTip wing therefore produces a consistantly stronger tip vortex.

There are two aspects believed to be the source of this difference:

1. In the PeakTip case, the tip vortex has one single, longer, continous edge over which vorticity is built up progressively, whereas in the ValTip case, due to the way the geometry was constructed there are two effective shedding edge, one which is the angled edge of the last tubercle and the other is the remaining straight edge of the wing, generating two discrete shedding locations, as shown in Figure 5.15.

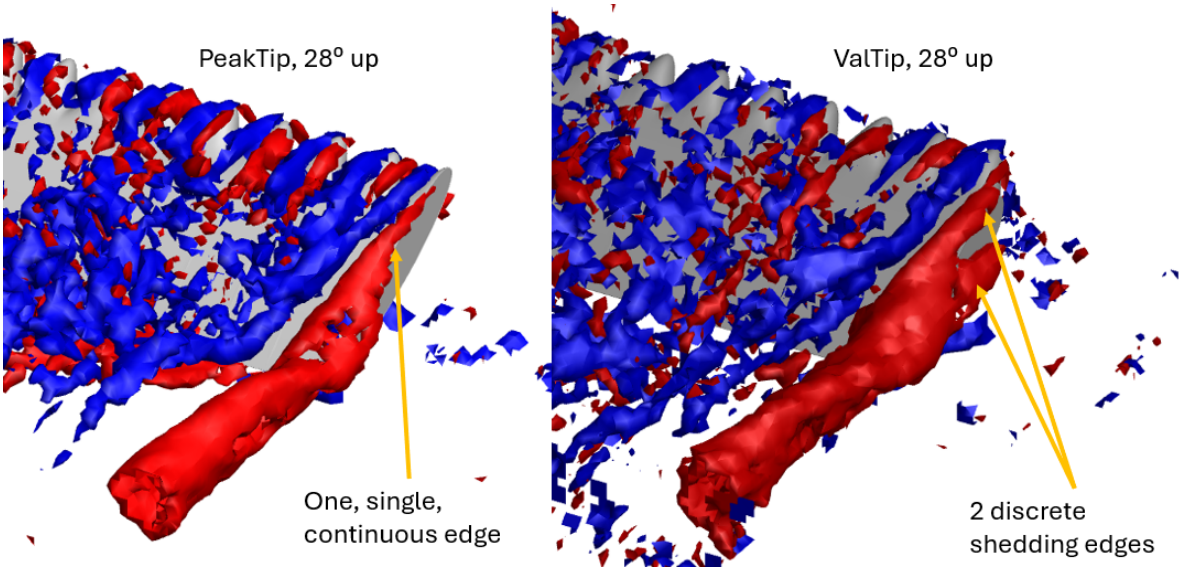

Figure 5.15: Tip detail view of $\omega_x \cdot c/U_\infty = -3$ iso-surface (blue) and $\omega_x \cdot c/U_\infty = +3$ iso-surface (red) for phase-averaged $k = 0.1$ experimental data

2. In the PeakTip case, the first blue vortex is formed approximately half a tubercle wavelength (0.5λ) closer to the shedding edge of the tip vortex than in the ValTip case. This results in a stronger downwash in between the tip vortex and the first blue vortex in the PeakTip case. This is shown by a contour plot of vertical velocities at the X-plane corresponding to the quarter-chord line of the wing in Figure 5.16. Because of this stronger early downwash, the two counter-rotating vortices move further apart in the PeakTip case than in the ValTip case.

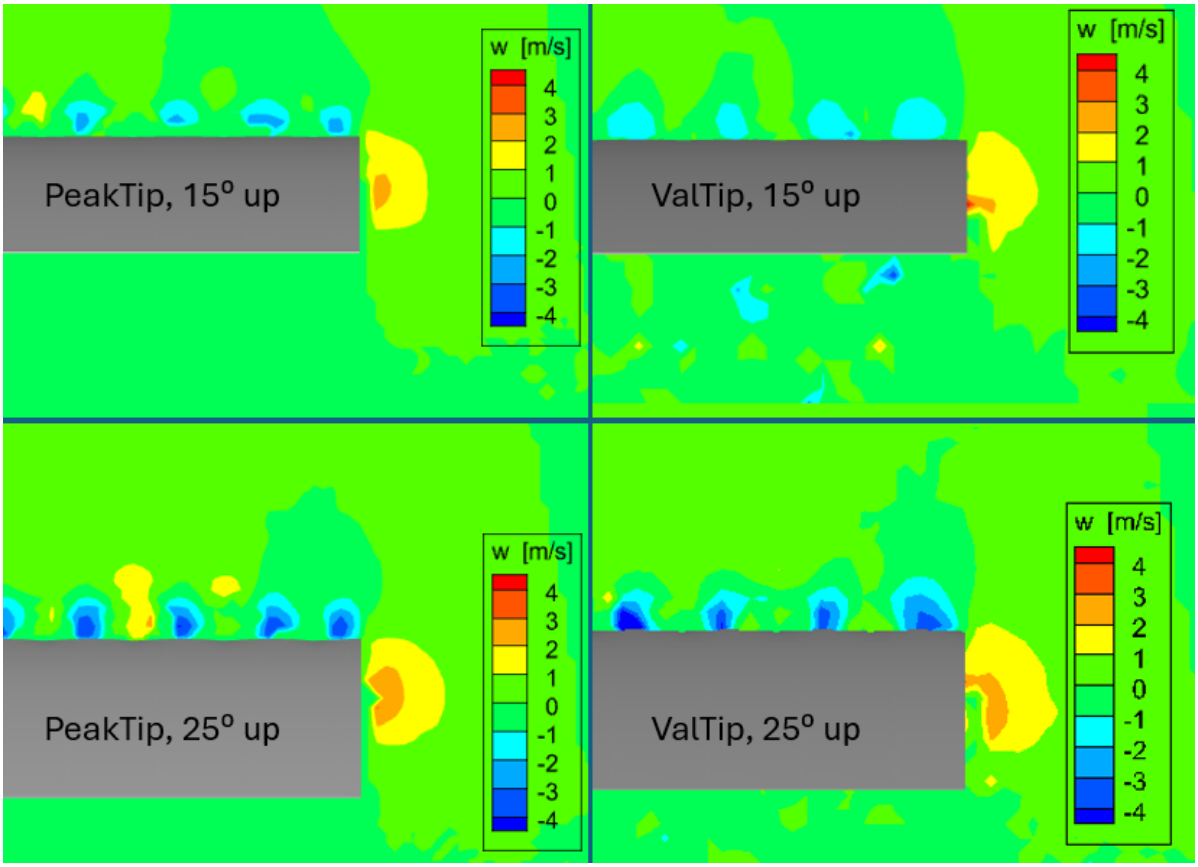

Figure 5.16: Vertical velocity plots taken on an X-slice at the quarter-chord plane of the wing on $k = 0.1$ phase-averaged experimental data

The tip detail snapshots in Figure 5.17 show iso-surfaces of vorticity equal in magnitude, but opposite in sign. It is visible that for all angles of attack the first blue vortex is drawn closer to the wing root in the PeakTip case than in the ValTip case. Ultimately, this means that later downstream this blue vortex exerts less destructive influence on the tip vortex.

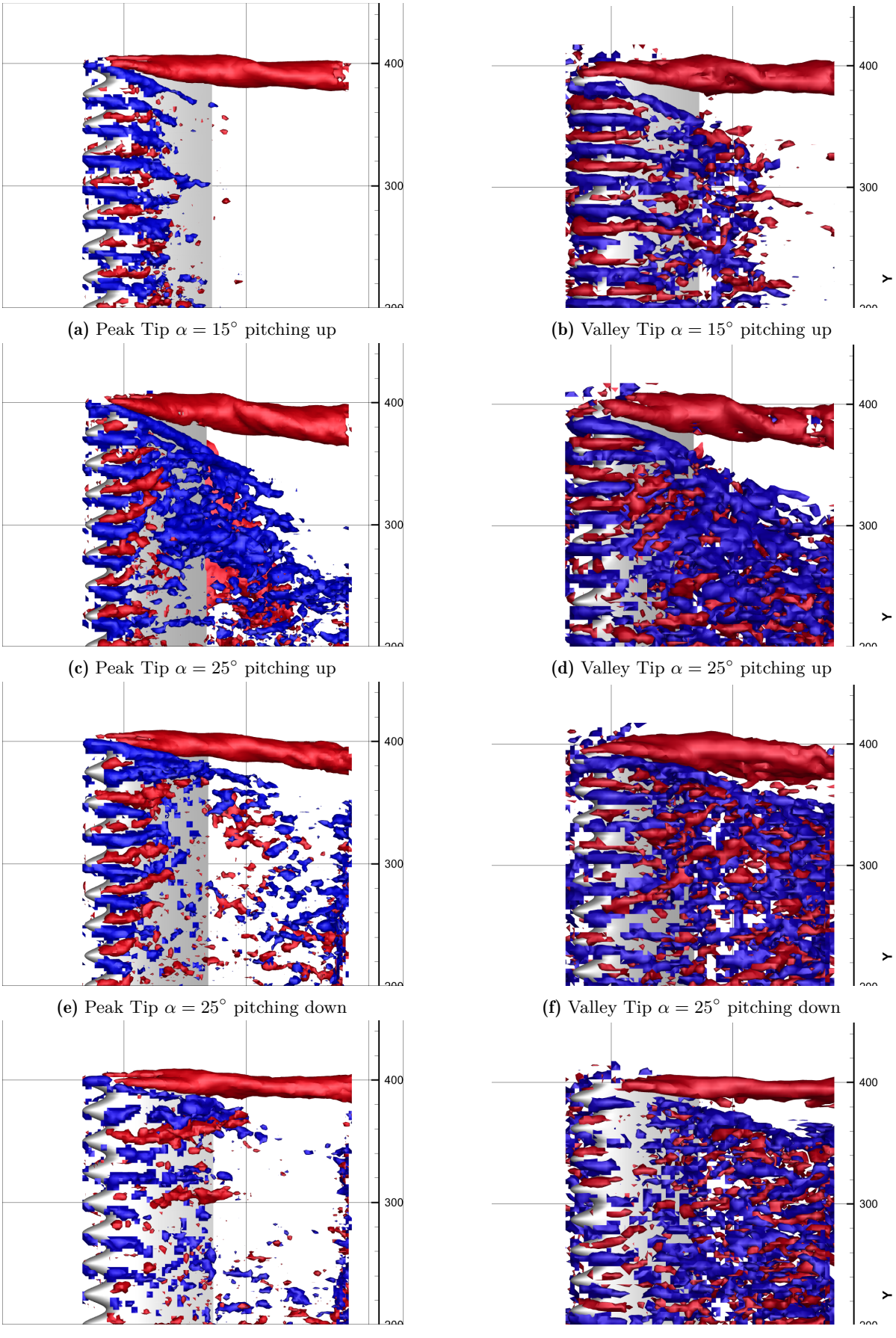

(a) Peak Tip $\alpha = 15°$ pitching up

(b) Valley Tip $\alpha = 15°$ pitching up

(c) Peak Tip $\alpha = 25°$ pitching up

(d) Valley Tip $\alpha = 25°$ pitching up

(e) Peak Tip $\alpha = 25°$ pitching down

(f) Valley Tip $\alpha = 25°$ pitching down

(g) Peak Tip $\alpha = 15°$ pitching down

(h) Valley Tip $\alpha = 15°$ pitching down

Figure 5.17: Z-axis view of $\omega_x \cdot c/U_\infty = -3$ iso-surface (blue) and $\omega_x \cdot c/U_\infty = +3$ iso-surface (red) for phase-averaged $k = 0.1$ experimental data

5.4.3. Effect of LE tubercles on induced drag

Lift-induced drag is an inviscid phenomenon resulting from the pressure difference between the upper and lower surfaces of a finite-span wing that creates a spanwise pressure gradient, causing air to flow around the wingtip and form vortices at the tips [9]. The wake-integral technique calculates drag by integrating flow variables over an arbitrary crossflow plane in the wake of the air vehicle, known as a Trefftz plane [42]. This method avoids the inaccuracies associated with the misdirection of projected pressures or the additive cancellation of nearly equal quantities. It also provides insight into the physical sources of drag by allowing the decomposition of drag into its relevant components—viscous drag, shock wave drag, and induced drag—as separate integrals. The Trefftz plane analysis, as used by Snyder and Povitsky [43] expressed the induced drag force as equivalent to the kinetic energy transferred to the crossflow velocities (v and w, for the y-axis and z-axis respectively) and is given by the following equation:

$$D_i = \frac{\rho}{2} \int (v^2 + w^2) dydz \tag{5.1}$$

Therefore the induced drag coefficient is determined by:

$$C_{D_i} = \frac{D_i}{0.5\rho U_\infty^2 S} \tag{5.2}$$

Similarly to the way the circulation was integrated over a cycle of the phase-averaged oscillation results, the crossflow integral was computed as well, over a plane transversal to the flow, located as far downstream of the wing as allowed by the measurement domain (i.e. at 1 chord downstream of the wing's trailing edge). The results are shown for a comparison between the SLE wing and the PeakTip wing in the figure below Figure 5.18. the range of values and behaviour of the SLE wing align to existing results from Birch and Lee's [29] whose study has found a maximum of $C_{D_i} = 0.013$ for an oscillation from $\alpha = 12°$ to $\alpha = 22°$, as shown in the background section in Figure 2.13b. Furthermore, the current results as well as Birch and Lee's results for the induced drag coefficient are closely related to the circulation values, with the maximum induced drag occurring at the maximum tip vortex circulation angle of attack.

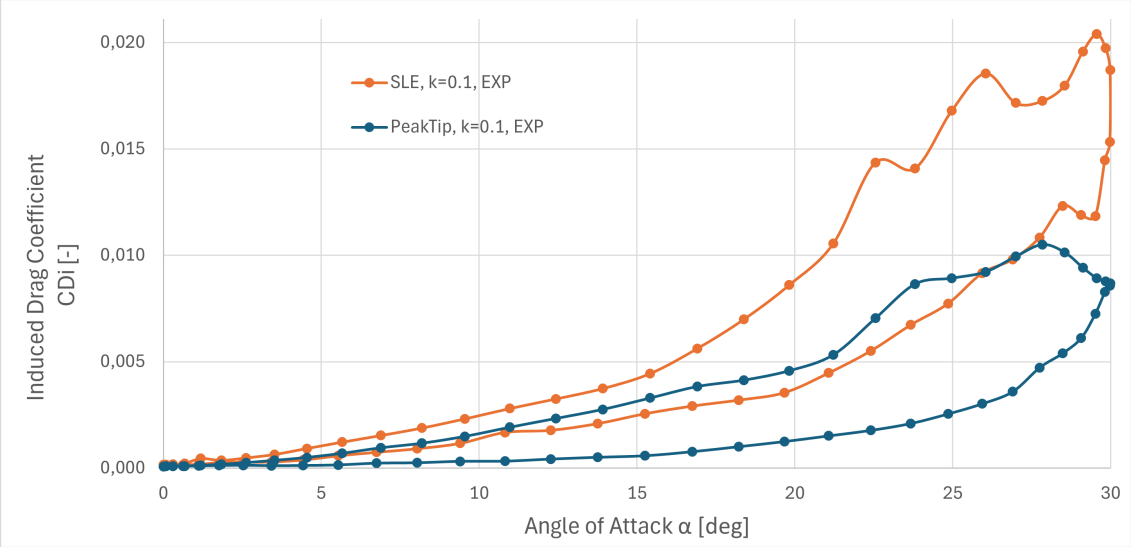

Figure 5.18: Phase-lag compensated, induced drag coefficient comparison of SLE and tubercle PeakTip wings obtained from phase-averaged experimental data

However, the values for the induced drag coefficient alone do not tell the whole story. In order to gauge the efficiency of the different wing shapes, the induced drag value needs to be contextualized using lift. For this, the span efficiency factor can be used:

$$e = \frac{C_L^2}{C_{D_i} \pi AR} \tag{5.3}$$

While the aspect ratio AR is known and the C_{D_i} has been obtained from the Trefftz analysis, the C_L is not directly available for the experimental data due to the lack of force balance measurements. Therefore, this can only be approximated by using the Kutta-Joukowski theorem. This will not provide an exact absolute value of the lift, but it will allow for the relative comparison between the two wing shapes.

$$C_L = \frac{L}{0.5\rho U_\infty^2 S} = \frac{\Gamma \rho U_\infty b}{0.5\rho U_\infty^2 S} = \frac{\Gamma}{0.5 U_\infty c} \tag{5.4}$$

This estimation of the lift coefficient obtained from the lifting-line theory can be visualised in Figure 5.19. This, of course, is just a scaled version of the graph showing the phase-lag compensated tip vortex circulation from Figure 5.13, but shows the magnitude of the lift coefficient is in line with expectations from other dynamic studies.

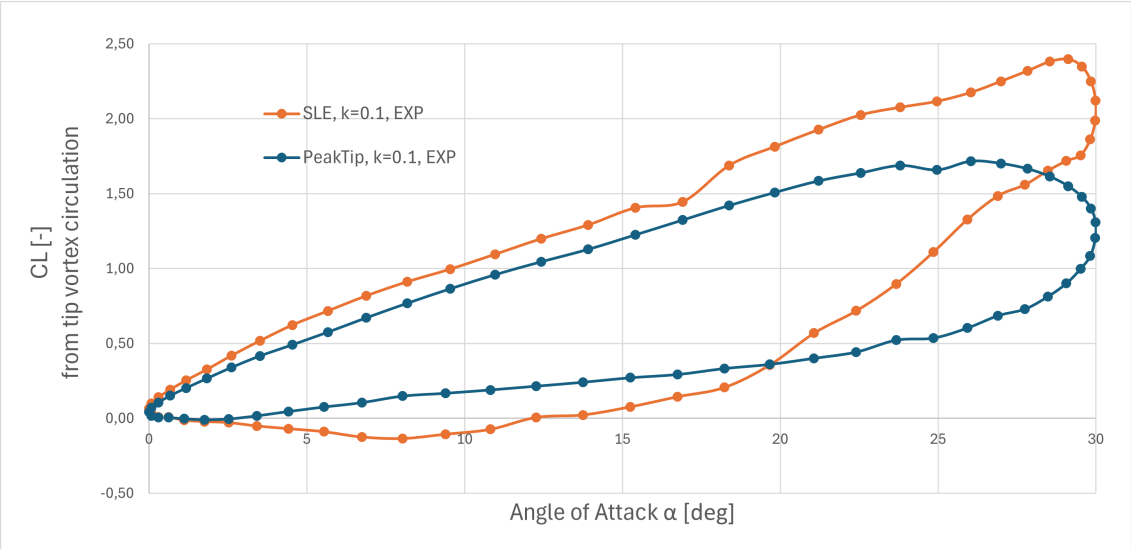

Figure 5.19: Phase-lag compensated, lift coefficient (estimated from tip vortex circulation) comparison of SLE and tubercle PeakTip wings obtained from phase-averaged experimental data

The span efficiency factor in this case is, therefore simply showing the proportionality relation below:

$$e \propto \frac{C_L^2}{C_{D_i}} \quad or \quad e \propto \frac{\Gamma^2}{C_{D_i}} \tag{5.5}$$

Applying the above equations produces the span efficiency factor from the phase-lag compensated circulation values. The variation of this span efficiency factor over the oscillation is shown in Figure 5.20.

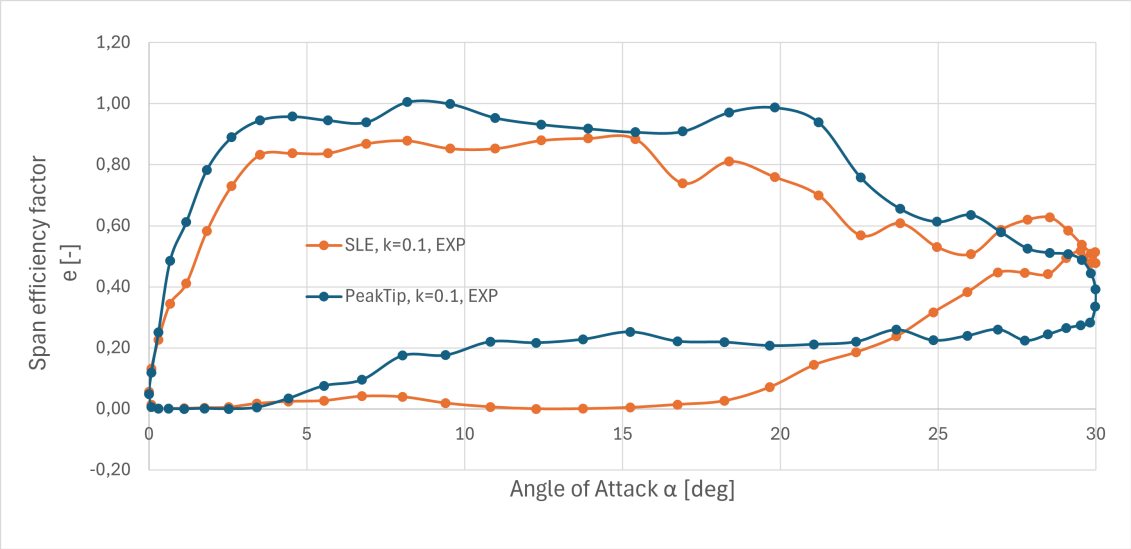

Figure 5.20: Phase-lag compensated, span efficiency factor comparison of SLE and tubercle PeakTip wings obtained from phase-averaged experimental data

It is clear that the PeakTip tubercle wing exhibits a higher span efficiency than the SLE wing at almost every point of the cycle. For the linearly-increasing lift region from $\alpha = 5°$ to $\alpha = 20°$ on the upstroke phase of the oscillation the results show almost constant values of the span efficiency factor for each of the wings, as shown in Figure 5.21, along with a linear trendline to remove the noise from the experimental values.

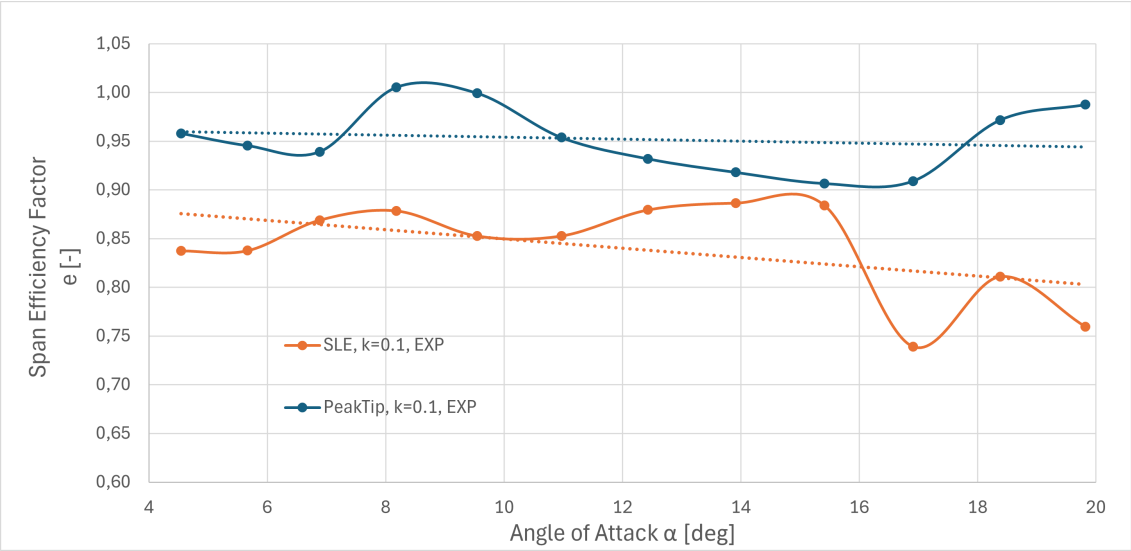

Figure 5.21: Span efficiency factor detailed comparison of SLE and tubercle PeakTip wings obtained from phase-averaged experimental data

A span efficiency factor of $e = 1$ is associated to the elliptical lift distribution, while a typical rectangular wing has an efficiency factor of around $e = 0.7$. Based on this information, it is clear that the current method overestimates this efficiency, but, as mentioned before, it needs to be stressed that while not entirely accurate in an absolute sense, this span efficiency factor is useful for a relative comparison between the wing leading-edge shapes. This way, based on Equation 5.5, it is clear that the PeakTip tubercle leading-edge wing produces less induced drag for the same amount of lift compared to the SLE wing.

The hypothesis that the current study proposes regarding why the PeakTip tubercle wing shows an overall higher span efficiency factor than the SLE wing is that the streamwise vortices shed by the leading-edge tubercles inhibit spanwise flow by compartmentalising it, acting in a similar manner to wing fences. This hypothesis is best justified by examining the contour plots of spanwise velocity in Figure 5.22 taken at an angle of attack $\alpha = 20°$, which is the point with the biggest span efficiency difference. Starting with a slice near the leading-edge, the alternating pattern of inwash and outwash produced by the tubercles is visible. moving downstream, around the $x/c = 0.3$ location, the slice shows a wider spread inwash region on the top side of the SLE wing, while the tubercle wing still retains the alternating pattern and a discretised inwash region, more concentrated at the tip. Also, the outwash from the underside is stronger in all chord-wise locations from the SLE wing. Going further downstream to the half-chord point, it is again apparent how the tubercle streamwise vortices have kept the inwash region of the PeakTip wing from spreading as much inboard as in the SLE case.

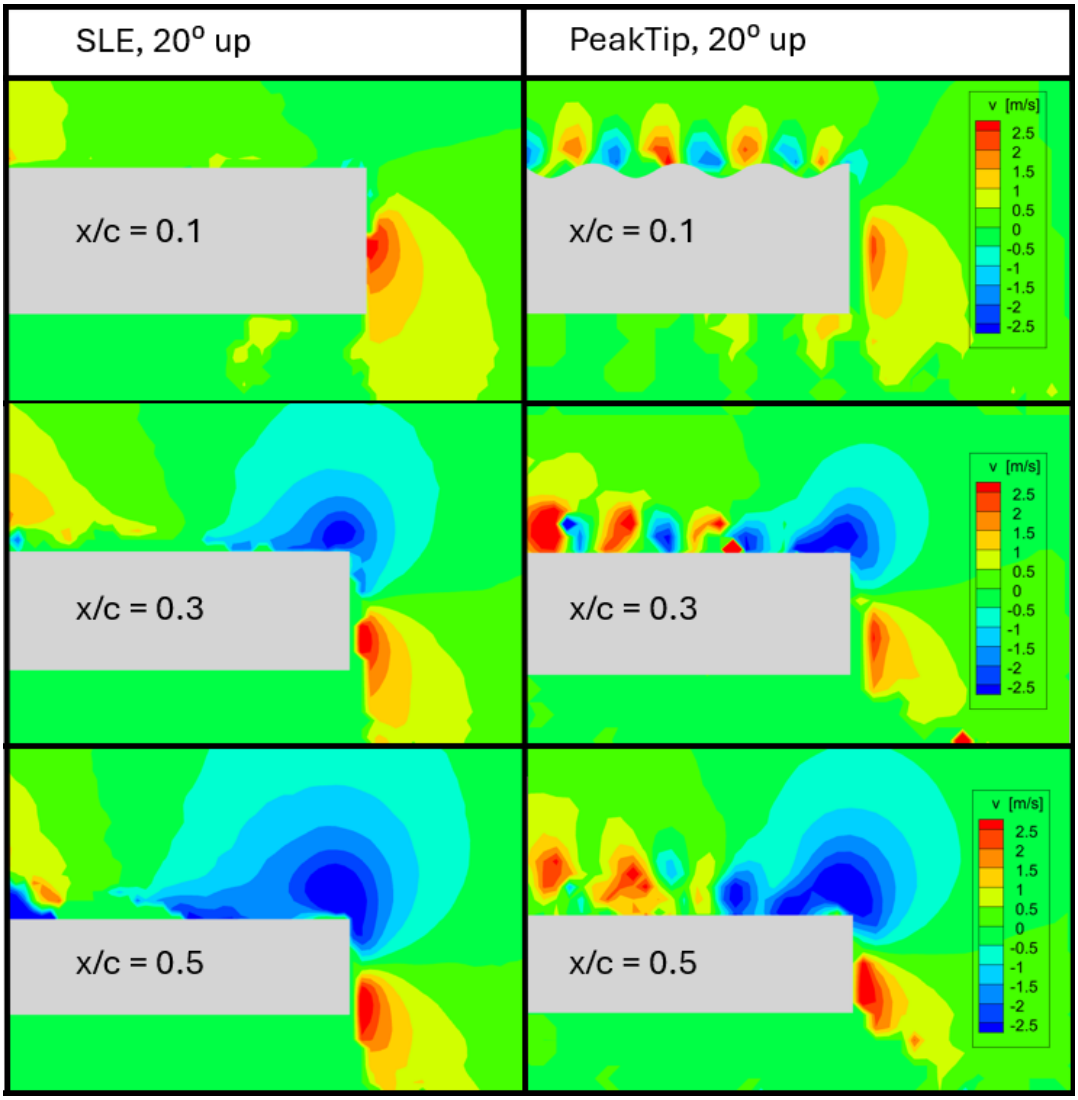

Figure 5.22: Spanwise velocity v contour plot comparison of SLE and tubercle PeakTip wings obtained from phase-averaged experimental data; negative (blue) values represent in-wash

Furthermore, the destructive influence of, in particular, the first tubercle streamwise anti-clockwise vortex on the clockwise tip vortex, explained also in Subsection 5.4.2 reduces the tip vortex circulation and its downwash, therefore reducing the induced drag.

6

Conclusions and Recommendations

6.1. Conclusions

6.1.1. Answers to the research questions

1. **Do the LE tubercles extend the usable angle of attack envelope of finite wings subjected to sinusoidal pitch rate oscillations?**

   CFD and experimental data offer conflicting answers to this questions, but as was established earlier, experimental data is considered to be the ground truth of this study because of the validity and very physical character of the results. Experimental data suggests that over the harshest possible sinusoidal oscillation of the study, namely from $\alpha = 0°$ to $\alpha = 30°$ and back down to $\alpha = 0°$ (centred around $\alpha = 15°$) at a reduced frequency of $k = 0.1$, the tubercle wings **do not** exhibit a higher α_{max} than the straight leading edge wing. However, the tubercle wing results for the tip vortex circulation, that are the best indication of the force on the wing, together with the separated flow iso-surfaces, suggest that the tubercle wings have a faster and more linear re-attachment on the downstroke of the oscillation, reducing the hysteretic gap in lift between the upstroke and the downstroke.

   CFD force results show that the α_{max} of the tubercle wings is higher by a approximately 1° than in the case of the straight leading edge, but because the force values for the SLE wing are likely significantly under-predicted as explained in Section 4.3, it is hard to draw a trustworthy conclusion based on the CFD force data. However, the flow-field structure from CFD aligns very well with that found from experimental data for the same angles of attack and reinforces the trust in the working mechanisms of the tubercles, showing similar better re-attachment on the downstroke phase of the oscillation in the case of the tubercle wings. The leading-edge tubercles reduce the hysteretical gap in lift force between the upstroke and downstroke phases of the oscillation and this effect is amplified with increasing reduced frequency.

2. **How do the streamwise vortices of the LE tubercles interact with the tip vortex under unsteady conditions?**

   (a) How do tubercles influence the spanwise distribution of velocities in compartments?

   The vortex structures presented in the full flow-field characterisations in Section 5.1 and Section 5.2 as well as the velocity contour plots shown in Section 4.1 and Section 4.1 prove that the counter-rotating streamwise vortices shed by the tubercles create an alternating spanwise pattern of upwash and downwash that leads to an earlier flow separation in the tubercle trough locations. When the angle of attack grows the separation region forms stall cells bordered by the streamwise vortices, which aligns with the compartmentalisation phenomenon presented in literature, detailed in Subsection 2.3.4. This phenomenon is again

visible on the downstroke of the oscillation when the separation regions that had merged are again split by the streamwise vortices into clear stall cells visible in both CFD and experimental data.

(b) Are tip and bound vorticity affected by tubercles?

The clear answer is yes. Subsection 5.4.1 shows the evolution of the integrated tip vorticity over an oscillation cycle and it is clear that the tubercle wings have lower tip vorticity. This is due to, first of all, producing less lift than the SLE wing in the upstroke phase which aligns with literature findings. Secondly, the first blue vortex from the tip has a destructive influence on the tip vortex because of their counter-rotating nature.

Furthermore, the spanwise vorticity is also affected. In the SLE case a strong and coherent DSV forms at the leading edge and convects downstream over the wing providing the lift overshoot seen in Subsection 5.4.1 and well-known in literature, as described in Subsection 1.1.2. In the tubercle wing case, as shown in the full flow-field characterisations in Section 5.1 and Section 5.2, this spanwise vorticity is broken up by the tubercles. A coherent DSV is not allowed to form.

(c) How does the tip end condition influence the tip vortex behaviour?

As briefly mentioned above, the tip vortex of the tubercle wings is affected by the distructive influence of the first vortex from the tip of counter vorticity (blue to the tip vortex's red vorticity). The location where this first blue vortex is shed in relation to the tip vortex shedding location produces a slight difference in tip vorticity. This is visible in the graphs for phase-averaged data from Subsection 5.4.1 where on average the Peak Tip end condition wing exhibits overall higher tip vortex circulation than the Valley Tip end condition wing. That being said, the influence of the tip end condition on the overall performance of the wings is very small.

3. **Is the induced drag of a finite wing with LE tubercles reduced compared to a SLE wing?**

The answer to this question is also a clear yes. The induced drag of a wing is proportional to the tip vorticity, therefore it makes sense that the results of a Trefftz plane analysis presented in Subsection 5.4.3 align with this showing that the tubercle wings do indeed exhibit lower coefficients of induced drag throughout the range of angles of attack.

6.1.2. Conclusions regarding methodology

6.1.2.1. Experimental methodology

The experimental side of the study was conducted in the W-Tunnel at the High Speed Laboratory of the TU Delft. This has been undertaken with 3 finite span (i.e. wing tip exposed) model wings at a Reynolds number of $Re = 3.3 \times 10^4$. Images of the flow seeded with helium filled soap bubbles around the wings oscillating sinusoidally in pitch were acquired using an array of 4 high speed cameras. The images were processed using the Davis software to produce particle tracks through the Shake-the-Box algorithm. This has provided a well space and time resolved flow field that allowed for the identification of the complex structures involved with leading edge tubercle wings namely separation regions, the counter-rotating streamwise vortices and the tip vortex.

For understanding the average performance over the oscillation cycle of the various wings, phase-averaging was used. This successfully emphasized coherent vortex structures and provided an insight into the average extent of flow separation, allowing for a performance comparison between the wings.

6.1.2.2. Computational methodology

The experimental study was complemented by a computational study involving CFD simulations that aimed to model the wind tunnel test conditions, including the test section walls in order for correlation

with the experimental data to be as close as possible.

An unstructured tetrahedral mesh with refinement layers next to the wing was generated using Ansys Fluent mesher and was deformed to specified node locations according to a sinusoidal function in order to replicate the exact pitch oscillation of the wing in the tunnel. The simulations were ran in Ansys CFX using a U-RANS solver with a k-ω SST turbulence model. A mesh refinement study as well as a turbulence intensity and surface roughness study were required to reach results that align well in terms of flow-field structure with the phase-averaged experimental results.

However, it was shown that there are a few caveats involved with the magnitude of certain flow parameters, with the CFD most likely under-predicting the lift force of the straight leading edge wing where the typical dynamic lift-overshoot is not present and also under-predicting the peak values of vorticity, as is the case for the tip vortex. Therefore, the force and circulation graphs produced by this CFD method need to be interpreted with a cautious view.

6.2. Recommendations

As discussed throughout the reports, this study has a number of limitations that the author feels should be addressed in any future studies on the topic of wings with tubercle-leading edges, particularly any focusing on the unsteady aerodynamic behaviour of these wings:

- **Higher Reynolds number testing**

  Both the experimental and computational testing have been undertaken in this study at a very low Reynolds number due to infrastructure limitations, as explained in Subsection 3.1.1 in the context of choosing the parameters to test, namely at approx. $Re = 3.3 \times 10^4$. This is lower than the Reynolds numbers at which most of the other existing research was performed, making it harder to compare results. Furthermore, the current study is performed below the range of Reynolds numbers for typical or potential applications of leading-edge tubercles such as wind turbine blades or helicopter rotor blades. This is particularly relevant as the tubercles are investigated for their effect on delaying separation and stall and flow separation is highly dependent on the Reynolds number, which dictates the transition from laminar to turbulent flow, the position of the separation point and the overall behavior of the boundary layer. Therefore, testing for example in a water tunnel could be a solution to achieve higher Reynolds numbers, while maintaining the reduced frequency and still being able to track the particles during this unsteady phenomenon.

- **Force or pressure tap wind-tunnel measurements**

  While having a clear picture of the complex 3D flow-field around the tubercle wings using 3D PTV is very valuable, complementing this with force balance measurements or even surface pressure tap data to extract the forces from would have been very valuable in the context of this study for two reasons: first, it would have made drawing a conclusion on the stall behaviour and angle of attack for maximum lift much easier and second, it would have been very useful for tuning the CFD simulation parameters to achieve a better correlation with experimental results.

- **LES simulations**

  For the scope and duration of the present study, U-RANS transient simulations showed that it is possible to at least model the phenomena involved with leading-edge tubercles over a pitching oscillation to a point were they can be compared well to experimental data and used to understand thsi wing shape better. But at the reduced frequencies of this study, the aerodynamic phenomena occuring are highly unsteady with vortex shedding, separation bubble shedding etc. A future study utilising LES simulations, for example, could capture these unsteady events better.

- **Different tubercle shapes and distributions**

  The present study has investigated one single tubercle shape, inspired from previous results available in the literature. Trials with different tubercle shapes might prove to be more effective and

potentially a parametric optimisation study could also be conducted to find a better suited tubercle shape. Furthermore, variations of the distribution of the tubercles across the span, for example only placing a number of them near the tip, could potentially provide some of the tip vortex strength reduction and stall delay benefits near the tip, while most of the span remains clean and can bridge the lift force deficit to the pure straight leading edge wings.

References

[1] J.G. Leishman. *Principles of Helicopter Aerodynamics*. 2nd ed. Cambridge University Press, 2006.

[2] R. Colpitts and R.E. Perez. "Application of Leading-Edge Tubercles on Rotor Blades". In: *AIAA Journal* 61.1 (2023), pp. 255–270. DOI: 10.2514/1.j062175. URL: https://doi.org/10.2514/1.j062175.

[3] J.M. Seddon and S. Newman. *Basic Helicopter Aerodynamics*. 3rd ed. John Wiley & Sons, 2011.

[4] F.O. Carta. "Experimental Investigation of the Unsteady Aerodynamic Characteristics of NACA0012 Airfoil". In: *United Aircraft Laboratory Report* (1960), pp. M–1283–1.

[5] M. Kramer. "Die Zunahme des Maximalauftriebs von Tragflügeln bei plötzlicher Anstellwinkeländerung (Böeneffekt)". In: *ZFM* 23 (1932), p. 185.

[6] Ü. Gülçat. *Fundamentals of Modern Unsteady Aerodynamics*. Springer International Publishing, 2021. DOI: 10.1007/978-3-030-60777-7. URL: https://doi.org/10.1007/978-3-030-60777-7.

[7] W. Sanz and M. F. Platzer. "On the Navier–Stokes Calculation of Separation Bubbles With a New Transition Model". In: *Journal of Turbomachinery* 120.1 (1998), pp. 36–42. DOI: 10.1115/1.2841385. URL: https://doi.org/10.1115/1.2841385.

[8] Y. Zheng and B. R. Ramaprian. "An Experimental Study of Wing Tip Vortex in the Near Wake of a Rectangular Wing". In: (1993).

[9] J. D. Anderson. *Fundamentals of aerodynamics*. Mcgraw-hill Publishing Co., 2007.

[10] Y.O. Han and J. G. Leishman. "Investigation of Helicopter Rotor-Blade-Tip-Vortex Alleviation Using a Slotted Tip". In: *AIAA Journal* 42.3 (2004), pp. 524–535. DOI: 10.2514/1.3254.

[11] H. Du et al. "Research on Rotorcraft Blade Tip Vortex Identification and Motion Characteristics in Hovering State". In: *Symmetry* 12.2 (2020), p. 196. DOI: 10.3390/sym12020196.

[12] F.E. Fish. "Biomimetics and the Application of the Leading-Edge Tubercles of the Humpback Whale Flipper". In: *Flow Control Through Bio-inspired Leading-Edge Tubercles* (2020), pp. 1–39. DOI: https://doi.org/10.1007/978-3-030-23792-9_1.

[13] F.E. Fish and J.M. Battle. "Hydrodynamic Design of the Humpback Whale Flipper". In: *Journal of Morphology* 225.1 (1995), pp. 51–60. DOI: 10.1002/jmor.1052250105.

[14] H. Johari et al. "Effects of Leading-Edge Protuberances on Airfoil Performance". In: *AIAA Journal* 45.11 (2007), pp. 2634–2642. DOI: 10.2514/1.28497. URL: https://doi.org/10.2514/1.28497.

[15] D. S. Miklosovic et al. "Leading-Edge Tubercles Delay Stall on Humpback Whale (Megaptera Novaeangliae) Flippers". In: *Physics of Fluids* 16.5 (2004), pp. 39–42. DOI: 10.1063/1.1688341.

[16] I. Fernandes et al. "Theoretical and Experimental Investigation of Leading Edge Tubercles on the Wing Performance". In: *2013 Aviation Technology, Integration, and Operations Conference* (2013). DOI: 10.2514/6.2013-4300.

[17] J. Borg. "The Effect of Leading Edge Serrations on Dynamic Stall". Master Thesis. University of Southampton, Faculty of Engineering and the Environment, School of Engineering Sciences, 2012.

[18] D. Custodio, C. W. Henoch, and H. Johari. "Aerodynamic Characteristics of Finite Span Wings with Leading-Edge Protuberances". In: *AIAA Journal* 53.7 (2015), pp. 1878–1893. DOI: 10.2514/1.j053568. URL: https://doi.org/10.2514/1.j053568.

[19] N. Rostamzadeh, K. Hansen, and R. Kelso. "Tubercled Wing Flow Physics and Performance". In: *Flow Control Through Bio-inspired Leading-Edge Tubercles* (2020), pp. 41–68. DOI: 10.1007/978-3-030-23792-9_2.

[20] K.L. Hansen, R.M. Kelso, and B.B. Dally. "Performance Variations of Leading-Edge Tubercles For Distinct Airfoil Profiles". In: *AIAA Journal* 49.1 (2011), pp. 185–194. DOI: 10.2514/1.j050631.

[21] J Katz. *Race Car Aerodynamics*. Robert Bentley, Incorporated, 1996.

[22] M.D. Bolzon, R.M. Kelso, and M. Arjomandi. "Tubercles and Their Applications". In: *Journal of Aerospace Engineering* 29.1 (2016). DOI: 10.1061/(asce)as.1943-5525.0000491.

[23] C. Cai et al. "Periodic and Aperiodic Flow Patterns Around an Airfoil with Leading-Edge Protuberances". In: *Physics of Fluids* 29.11 (2017), p. 115110. DOI: 10.1063/1.4991596.

[24] P.W. Weber et al. "Computational Evaluation of the Performance of Lifting Surfaces with Leading-Edge Protuberances". In: *Journal of Aircraft* 48.2 (2011), pp. 591–600. DOI: 10.2514/1.c031163.

[25] H. Carreira Pedro and M. Kobayashi. "Numerical Study of Stall Delay on Humpback Whale Flippers". In: *46th AIAA Aerospace Sciences Meeting and Exhibit* (2008). DOI: 10.2514/6.2008-584.

[26] G. Moscato, J. Mohamed, and G. P. Romano. "Improving Performances of Biomimetic Wings with Leading-Edge Tubercles". In: *Experiments in Fluids* 63.9 (2022). DOI: 10.1007/s00348-022-03493-8. URL: https://doi.org/10.1007/s00348-022-03493-8.

[27] S.J. Reid, R.E. Perez, and A. Asghar. "Characterization of Tubercle Effects on Finite Span Wings". In: *AIAA Aviation 2019 Forum*. American Institute of Aeronautics and Astronautics, 2019. DOI: 10.2514/6.2019-3294. URL: https://doi.org/10.2514/6.2019-3294.

[28] J.W. Chang and S.O. Park. "Measurements in the Tip Vortex Roll-up region of an Oscillating Wing". In: *AIAA Journal* 38.6 (2000), pp. 1092–1095. DOI: 10.2514/2.1072.

[29] D. Birch and T. Lee. "Tip Vortex Behind a Wing Undergoing Deep-Stall Oscillation". In: *AIAA Journal* 43.10 (2005), pp. 2081–2092. DOI: 10.2514/1.13139.

[30] E.C. Maskell. "Progress Towards a Method for the Measurement of the Components of the Drag of a Wing of Finite Span". In: *RAE Technical Report No. 72232* (1972).

[31] J. Hrynuk and D. Bohl. "Effects of Leading-Edge Tubercles on Dynamically Pitching Airfoils". In: *Flow Control Through Bio-inspired Leading-Edge Tubercles*. Springer International Publishing, 2020, pp. 131–146. DOI: 10.1007/978-3-030-23792-9_6. URL: https://doi.org/10.1007/978-3-030-23792-9_6.

[32] M.R. Amiralaei, H. Alighanbari, and S.M. Hashemi. "An Investigation Into the Effects of Unsteady Parameters on the Aerodynamics of a Low Reynolds Number Pitching Airfoil". In: *Journal of Fluids and Structures* 26.6 (2010), pp. 979–993. DOI: 10.1016/j.jfluidstructs.2010.06.004.

[33] P. Deval. "Cylinder Drag Reduction Using Discrete Surface Roughness: An Experimental Investigation Into the Effect of Cylindrical Roughness Elements". Master Thesis. Delft University of Technology, Faculty of Aerospace Engineering, 2023.

[34] G. E. Elsinga et al. "Tomographic Particle Image Velocimetry". In: *Experiments in Fluids* 41.6 (2006), pp. 933–947. DOI: 10.1007/s00348-006-0212-z.

[35] D. Schanz, S. Gesemann, and A. Schröder. "Shake-the-box: Lagrangian Particle Tracking at High Particle Image Densities". In: *Experiments in Fluids* 57.5 (2016). DOI: 10.1007/s00348-016-2157-1.

[36] M. Raffel et al. *Particle Image Velocimetry - A Practical Guide*. Springer, Switzerland, 2018. DOI: https://doi.org/10.1007/978-3-319-68852-7.

[37] Francesco M A Mitrotta, Jurij Sodja, and Andrea Sciacchitano. "On the Combined Flow and Structural Measurements Via Robotic Volumetric PTV". In: *Measurement Science and Technology* 33.4 (2022), p. 045201. DOI: 10.1088/1361-6501/ac41dd.

[38] P. Cueto Corral. "Propeller Slipstream Characterisation by Large-Scale PIV". Master Thesis. Delft University of Technology, Faculty of Aerospace Engineering, 2023.

[39] T. Yasuda et al. "Effect of the Reynolds Number on the Performance of a NACA0012 Wing with Leading Edge Protuberance at Low Reynolds Numbers". In: *Flow, Turbulence and Combustion* 102.2 (2018), pp. 435–455. DOI: 10.1007/s10494-018-9978-3.

[40] L.E. Ericsson and J.P. Reding. "Further Consideration of "Spilled" Leading-Edge Vortex Effects on Dynamic Stall". In: *Journal of Aircraft* 14.6 (1977), pp. 601–603. DOI: 10.2514/3.58827.

[41] J. Winslow et al. “Basic Understanding of Airfoil Characteristics at Low Reynolds Numbers (104–105)”. In: *Journal of Aircraft* 55.3 (2018), pp. 1050–1061. DOI: 10.2514/1.c034415.

[42] R.M. Cummings, M.B. Giles, and G.N. Shrinivas. “Analysis of the Elements of Drag in Three-Dimensional Viscous and Inviscid Flows”. In: (1996). URL: https://api.semanticscholar.org/CorpusID:122180621.

[43] T. Snyder and A. Povitsky. “Far-Field Induced Drag Prediction Using Vorticity Confinement Technique”. In: *Journal of Aircraft* 51.6 (2014), pp. 1953–1958. DOI: 10.2514/1.C032719.

A

Flow field snapshoths throughout the oscillation

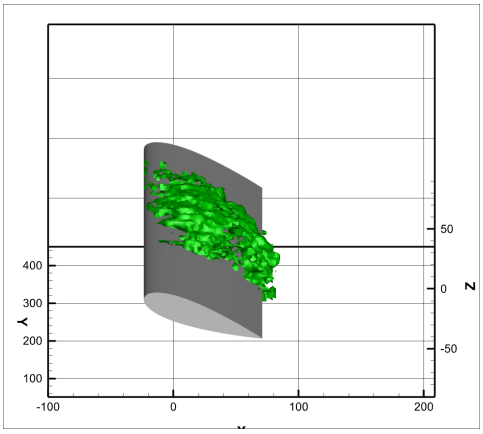

(a) $\alpha = 20^\circ$ pitching up

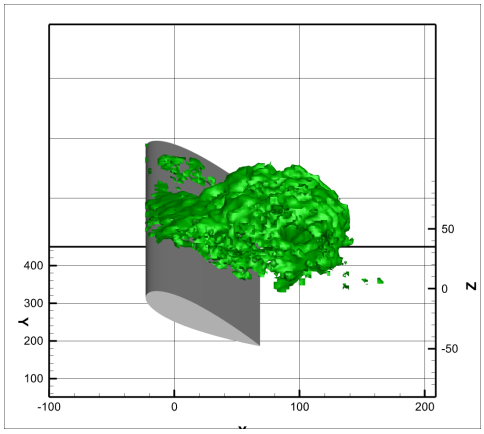

(b) $\alpha = 25^\circ$ pitching up

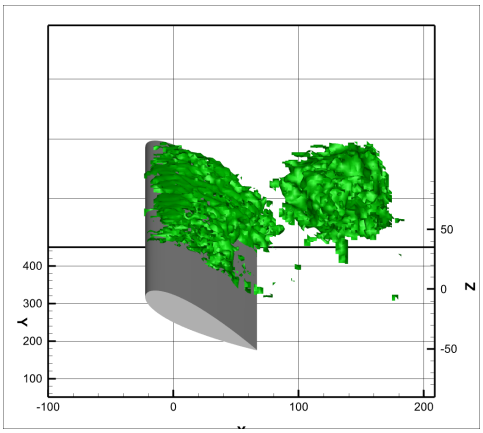

(c) $\alpha = 27^\circ$ pitching up

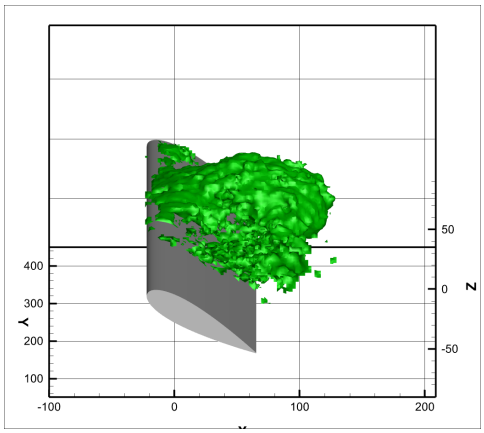

(d) $\alpha = 30^\circ$ maximum amplitude

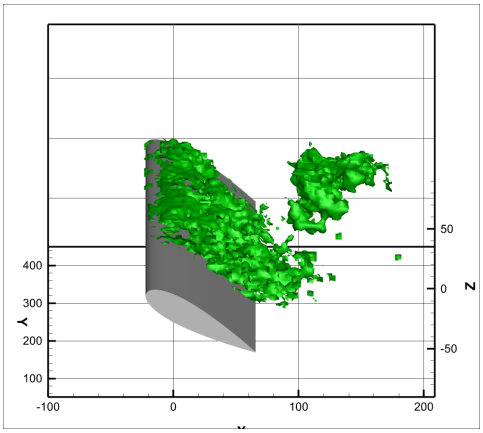

(e) $\alpha = 29.5^\circ$ pitching down

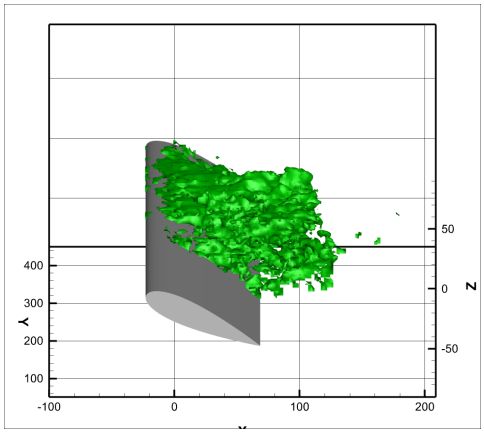

(f) $\alpha = 25^\circ$ pitching down

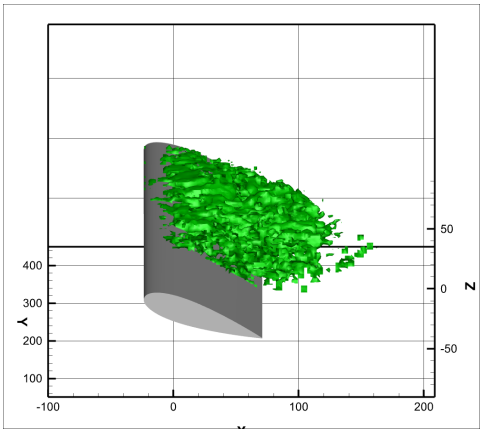

(g) $\alpha = 20^\circ$ pitching down

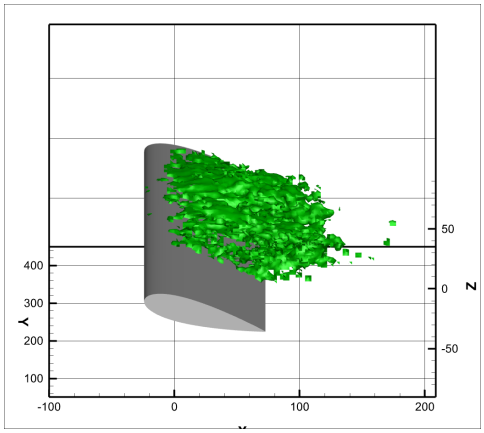

(h) $\alpha = 15^\circ$ pitching down

Figure A.1: Side view from the wing root of $U = 0[m/s]$ iso-surface for phase-averaged SLE, $k = 0.1$ experimental data

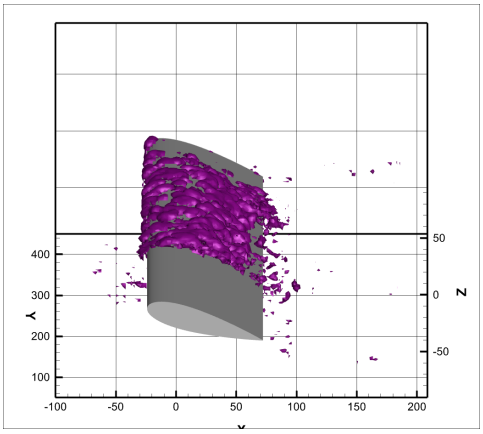

(a) $\alpha = 15°$ pitching up

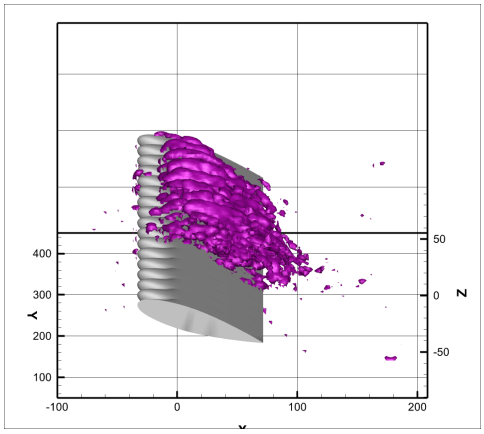

(b) $\alpha = 15°$ pitching up

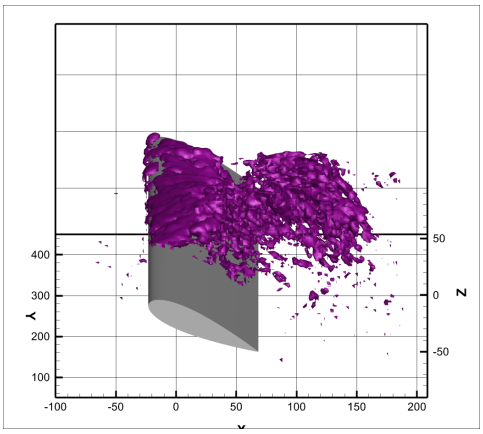

(c) $\alpha = 25°$ pitching up

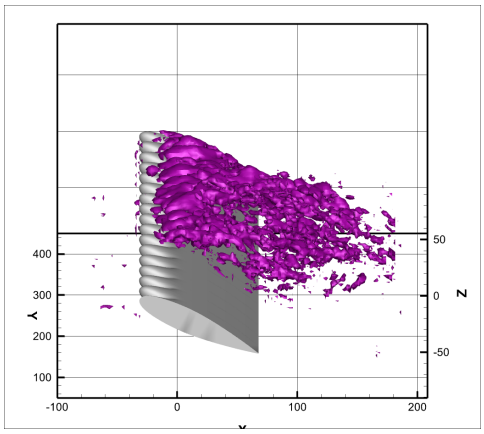

(d) $\alpha = 25°$ pitching up

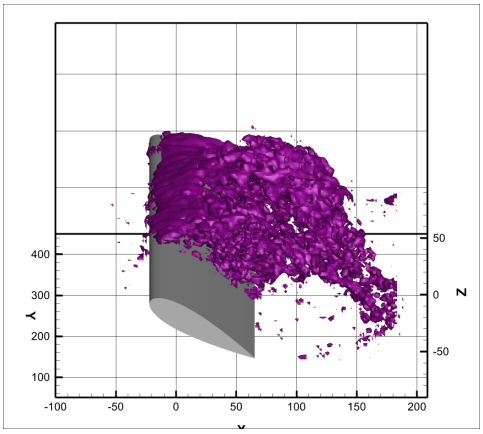

(e) $\alpha = 30°$ maximum amplitude

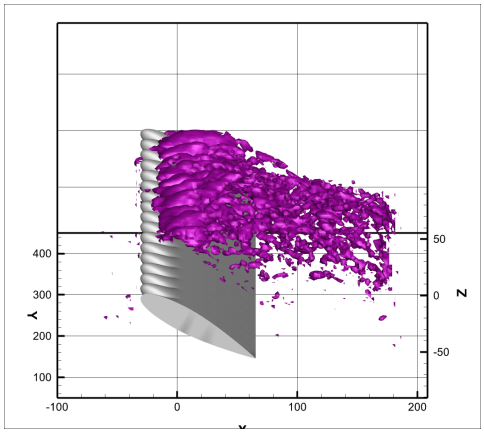

(f) $\alpha = 25°$ pitching down

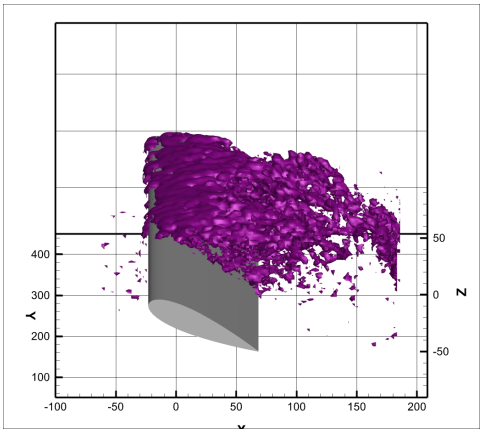

(g) $\alpha = 25°$ pitching down

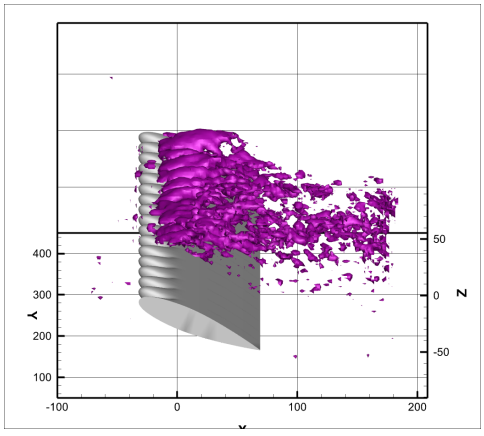

(h) $\alpha = 15°$ pitching down

Figure A.2: Side view from the wing root of $\omega_y \cdot c/U_\infty = 6$ iso-surface for phase-averaged SLE and PeakTip, $k = 0.1$ experimental data